

CHARGE STATE STUDIES OF HEAVY IONS PASSING THROUGH GAS

by

Wenjie Liu

THESIS SUBMITTED IN PARTIAL FULFILLMENT
OF THE REQUIREMENTS FOR THE DEGREE OF
MASTER OF SCIENCE
IN THE DEPARTMENT
OF
PHYSICS

© Wenjie Liu 2001
SIMON FRASER UNIVERSITY
November, 2001

All rights reserved. This work may not be
reproduced in whole or in part, by photocopy
or other means, without permission of the author.

APPROVAL

Name: Wenjie Liu

Degree: Master of Science

Title of thesis: Charge State Studies of Heavy Ions Passing Through Gas

Examining Committee: Howard Trottier
Professor, Simon Fraser University (Chair)

John M. D'Auria
Professor, Simon Fraser University

E. Daryl Crozier
Professor, Simon Fraser University

Ian D. Gay
Professor, Simon Fraser University

Art Olin
Senior Research Scientist, TRIUMF

Date Approved: November 8, 2001

Abstract

Charge State Studies of Heavy Ions Passing Through Gas

The charge state of an ion passing through matter fluctuates as a result of electron capture and loss in the collisions with the target atoms. Despite the existence of a large number of theoretical and experimental studies on this complicated atomic collision system, an accurate prediction of the charge state distribution is still not available. To meet DRAGON's future experimental needs, the non-equilibrium and equilibrium charge state distributions resulting from the collisions of ^{16}O , ^{23}Na , ^{24}Mg ions passing through a windowless hydrogen and helium gas target with the beam energy in the range of 0.138–0.875 MeV/u, 0.200–0.478 MeV/u, 0.200–0.800 MeV/u, respectively, have been measured using the differentially pumped gas target facility at Naples University, Italy, and DRAGON/ISAC, TRIUMF, Canada. It is determined that the equilibrium distribution is established at low target thickness. The equilibrium distribution depends on the projectile species, its energy and the nature of the target, while independent of the incident charge state. The uncertainties of the normalized charge state fractions are estimated to be less than 5% except for very low fractions. The equilibrium distribution is shown to be close to the Gaussian distribution. Semi-empirical formulas have been derived for the average equilibrium charge state and distribution width. Assuming that the probability of multiple electron capture and loss in a single collision are negligible, single electron capture and loss cross sections have been estimated using the least-squares method in cases where sufficient experimental charge state fraction data are available. The dependence of cross sections on projectile energy and charge state has been studied.

To My Parents

Acknowledgments

First and foremost, I would like to thank my supervisor, Professor John M. D’Auria, for his great interest in this work and the many fruitful discussion we have had. I could always count on him for advice and guidance.

My thanks also go to all the people contributed to this work. At Naples University, Professor Filippo Terrasi, guided my research and gave me a lot of useful suggestion. Gianluca Imbriani, Enzo Roca, Lucio Gialanella, Antonio D’Onofrio and Mario Romano all deserve credit for their contribution. Detlef Rogalla came all the way from Bochum University to work with us on the many overnight shifts. And without the help of tandem accelerator expert Gino Campajola, the experiments would not be possible to carry out successfully. I hope they all enjoyed this project as much as I did.

At TRIUMF, I would like to express my thanks to beam physicists Bob Laxdal and Matteo Pasini for all the effort they put into providing us beam of great quality.

Of course, I won’t forget all the DRAGONeers - Dave Hutcheon, Art Olin, Joel Rogers, Lothar Buchmann, Ahmed Hussein, Dave Ottewell, Don Hunter, Sabine Theis (Sabine Engel, now), Alan Chen, Shawn Bishop, Dario Gigliotti, etc. Without their hardwork in making DRAGON ‘alive’, my thesis work won’t exist. I also enjoyed the fruitful discussion in every DRAGON meeting.

Finally, I would like to thank my parents and brother, who always supported me from every aspect. Without them, I would have never made it.

Contents

Approval	ii
Abstract	iii
Dedication	iv
Acknowledgments	v
Contents	vi
List of Tables	viii
List of Figures	x
1 Introduction	1
1.1 Scientific Motivation	1
1.2 Overview of Charge-Changing Study	4
1.3 Outline of the Following Chapters	5
2 Theory of Charge-Changing Process	6
2.1 Description of Charge-Changing Process	6
2.2 Equilibrium Charge State Distribution	8
2.2.1 Concepts of Equilibrium Charge State Distribution	8
2.2.2 Average Equilibrium Charge State	10
2.2.3 Charge State Distribution Width	16
2.3 Cross Section	18
3 Experiment	24
3.1 Naples Experiment	24

3.2	DRAGON/ISAC Experiment	26
3.2.1	ISAC Heavy Ion Accelerator	28
3.2.2	DRAGON Facility	28
3.3	The Windowless Gas Target	29
3.3.1	Naples Target System	29
3.3.2	DRAGON Target System	32
3.4	Data Analysis and Uncertainties	39
3.5	Results	40
4	Discussion	44
4.1	Critical Target Thickness	44
4.2	Equilibrium Distribution	46
4.2.1	Reproducibility	46
4.2.2	Energy loss	48
4.2.3	Gaussian Distribution	48
4.2.4	Semi-empirical Formulas for \bar{q} And d	55
4.3	Single Electron Capture and Loss Cross Section	59
4.3.1	Least Squares Method	59
4.3.2	Scaling Rules for Cross Section	62
5	Conclusion	72
A	Compilation of Measured Growth Curves	74
A.1	Naples Experiment Results	75
A.2	DRAGON Experiment Results	86
B	Illustration of Experimental Data and Charge State distribution Calculation	90
	Bibliography	96

List of Tables

2.1	Experimental result from Betz et al. for parameter C and γ	12
3.1	Experimental and Data Analysis Uncertainties	41
3.2	Experimental Equilibrium Charge State Distribution, where * and † refer to data from Naples and DRAGON measurements, respectively.	43
4.1	Critical target thickness x_c and the corresponding pressure at Naples and DRAGON gas target, with * and † refer to data from Naples and DRAGON measurements, respectively.	45
4.2	Energy loss measurements versus SRIM calculation, with * and † refer to data from Naples and DRAGON measurements, respectively. Naples data have also been converted to corresponding energy loss through DRAGON target at 1 Torr (listed in the ' $E_{loss}1Torr(DRAGON)$ ' column with DRAGON measurement data). All energies are in unit of keV/u.	49
4.3	Experimental \bar{q} , d, and s versus \bar{q} and d from Gaussian fit, with * and † refer to data from Naples and DRAGON measurements, respectively. . . .	54
4.4	Single Electron Capture and Loss Cross sections for Heavy Ions, with * and † refer to data from Naples and DRAGON measurements, respectively. Uncertainties of the cross sections have been normalized to make χ^2 per freedom be 1.0. Additional normalization of all the cross sections with respect to the uncertainty in the target effective length are not included here.	63
4.5	Single Electron Capture and Loss Cross sections for Heavy Ions, with * and † refer to data from Naples and DRAGON measurements, respectively (continued). Uncertainties of the cross sections have been normalized to make χ^2 per freedom be 1.0. Additional normalization of all the cross sections with respect to the uncertainty in the target effective length are not included here.	64

4.6	Comparison of charge-changing cross sections for O^{5+} in H_2 and He with literature[43].	65
B.1	$^{16}O^{2+}0.138MeV/u + H_2$	92
B.2	$^{16}O^{2+}0.138MeV/u + H_2$ (continued)	93
B.3	$^{16}O^{4+}0.800MeV/u + H_2$	94
B.4	$^{16}O^{4+}0.800MeV/u + H_2$ (continued)	95

List of Figures

1.1	Schematic of DRAGON facility at ISAC, TRIUMF	3
2.1	Average relative equilibrium charge of ions passing through carbon (solid symbol) and other light foils (open symbol) plotted as a function of the reduced velocity $v/(v'Z^{0.45})$, with $v' = 3.6 \times 10^6$ m/s, and Z is the projectile atomic number. The solid line represents the semi-empirical estimation by Nikolaev and Dmitriev (equation (2.17))[5].	13
2.2	Average relative equilibrium charge of ions passing through gaseous target of nitrogen, oxygen and air, plotted as a function of the reduced velocity $v/(v_0Z^{0.55})$, with $v_0 = 2.188 \times 10^6$ m/s, and Z the projectile atomic number. The solid and open symbols refer to dense and more dilute gas target, respectively[5].	13
2.3	Average relative equilibrium charge of ions passing through solid target plotted as a function of the reduced scaling variable x [27].	14
2.4	Average relative equilibrium charge of ions passing through gaseous target plotted as a function of the reduced scaling variable x [27].	14
2.5	Universal plot of reduced width for various ions as a function of mean number of electrons attached to the ions $\bar{n} = Z_p - \bar{q}$. The details of (a) at $\bar{n} < 20$ are given in (b)[25].	17
2.6	Universal plot of reduced width for various ions as a function of mean number of electrons attached to the ions for solid target[27].	19
3.1	Schematic diagram of Naples facility, Italy[37, 38]. (S = X-Y steerers, SL = slits, FC = Faraday cup, MQPD = magnetic quadrupole doublet, MQPT = magnetic quadrupole triplet.)	25
3.2	Plan view of ISAC experimental hall, TRIUMF, Canada	27

3.3	Schematic diagram of the set-up for the charge-state distribution study using DRAGON facility	29
3.4	Schematic diagram of the differentially-pumped gas target system at Naples, Italy[40].	30
3.5	Schematic diagram of the target chamber of Naples target system. The distance between the centers of apertures A and A' is 248 ± 2 mm[40]. . . .	30
3.6	Pressure profile of H_2 gas (with cell pressure at 5.0 mbar) along the beam axis, as taken from [40].	31
3.7	DRAGON's differentially-pumped windowless gas target system.	32
3.8	DRAGON's gas target with the recirculation and cold trap of the gas handling system.	33
3.9	Detailed dimension of pumping tubes in DRAGON's differentially-pumped windowless system.	33
3.10	Schematic of DRAGON trapezoid target cell placed in a rectangular box. Two elastic monitors are installed at $\theta_{lab} = 30^\circ$ and 57° , respectively. . . .	35
3.11	Side view of two-row BGO array along the gas target.	37
3.12	Setting of the single BGO detector facing the target with slit opening 0.95cm. 37	
3.13	Normalized yield versus the detector position along the beam axis with position 20cm corresponding to the center of the target.	38
4.1	Comparison of equilibrium charge state distribution between Naples and DRAGON's measurements for ^{16}O beam passing through hydrogen gas target, with symbols representing the experimental data and line for Gaussian distribution.	47
4.2	Equilibrium charge state distribution of ^{16}O beam passing through hydrogen gas target, with symbols representing the experimental data and line for Gaussian distribution.	50
4.3	Equilibrium charge state distribution of ^{23}Na beam passing through hydrogen gas target, with symbols representing the experimental data and line for Gaussian distribution.	51
4.4	Equilibrium charge state distribution of ^{24}Mg beam passing through hydrogen gas target, with symbols representing the experimental data and line for Gaussian distribution.	52

4.5	Equilibrium charge state distribution of ^{16}O beam passing through helium gas target, with symbols representing the experimental data and line for Gaussian distribution.	53
4.6	$\ln(1 - \bar{q}/z)$ plotted as a function of reduced velocity, with (A) for various projectiles passing through hydrogen target and (B) for oxygen beam passing through hydrogen and helium target, respectively.	56
4.7	$\ln(1 - \bar{q}/z)$ plotted as a function of the expression determined by Nikolaev and Dmitriev[5].	58
4.8	$\ln(1 - \bar{q}/z)$ plotted as a function of $f(x)$, given by Schiwietz[27].	58
4.9	Reduced width $d/(Z_p^w)$ plotted as a function of mean number of electrons $n_e(=Z_p - \bar{q})$	60
4.10	Distribution width d plotted as a function of relative average equilibrium charge state.	60
4.11	Single electron capture cross section of ^{16}O beam passing through hydrogen gas target plotted as a function of charge state q and projectile energy E , respectively.	66
4.12	Single electron capture cross section of ^{23}Na beam passing through hydrogen gas target plotted as a function of charge state q and projectile energy E , respectively.	67
4.13	Single electron loss cross section of ^{16}O beam passing through hydrogen gas target plotted as a function of charge state q and projectile energy E , respectively.	69
4.14	Single electron loss cross section of ^{23}Na beam passing through hydrogen gas target plotted as a function of charge state q and projectile energy E , respectively.	70
B.1	E_0 reading normalized to incident beam intensity and time plotted as a function of pressure reading.	91

Chapter 1

Introduction

1.1 Scientific Motivation

For centuries, the goal of scientists is to understand the nature of the world. One of the most fundamental questions to be answered is the origin of elements.

It is now believed that nuclear reactions occurring in explosive phenomena such as novae, x-ray bursts, and supernovae play an important role in the synthesis of heavy nuclei. To fulfill a quantitative study of these phenomena, measurements of the rates of such reactions involving radioactive reactants are required. However, limited by the availability of radioactive beams, many key reaction rates have not yet been measured directly. DRAGON (Detector of Recoils And Gammas Of Nuclear reactions) combined with the new ISAC (Isotope Separator and ACcelerator) accelerated radioactive beam facility located at TRIUMF, Canada, was built for this study.

The primary goal of the program using the DRAGON facility is to explore from an experimental perspective, the most likely pathway of the initial nuclear reactions of explosive nucleosynthesis scenarios, particularly nova explosions and x-ray bursts. An important parameter is the nuclear reaction rate and the key reactions are radiative proton and alpha capture reactions, i.e., fusion of heavy nuclei with hydrogen or helium nuclei at stellar, explosive temperatures, namely of order 10^9 K or less than 1 MeV/u¹. These reactions can be dominated by resonance reactions but non-resonance, direct capture processes can also contribute. In the case of explosive nucleosynthesis, given higher temperatures than normal stellar environments and high hydrogen densities, the heavy nuclei can be radioactive, exotic nuclei. For this reason the ISAC accelerated radioactive beam facility is needed and the

¹u represents the atomic mass unit, which equals to one twelfth of the mass of ¹²C atom.

rates of these reactions can be measured in inverse kinematics, i.e., heavy projectile hitting the low Z (hydrogen or helium) target. The DRAGON recoil mass separator facility consisting of a windowless gas target system, followed by an electromagnetic mass separator, coupled to an end detection system to separate and detect the emitted reaction product is essential for this study. A schematic representation of the DRAGON facility is presented in Figure 1.1.

A windowless gas target is preferable to a solid target such as CH_2 for several reasons. First of all, hydrogen and helium are gaseous and solid targets are not very pure. Further, it is difficult to prepare an adsorbed hydrogen or helium target that is stable over a long period of time under heavy ion bombardment. Also, the coulomb scattering of other heavy ions in solid target, e.g. C atoms in CH_2 , will increase the background. So, with a gas target it is easier to maintain the target thickness, uniformity, purity and low background.

Secondly, for resonance reactions the yield varies inversely with the stopping power, not with total thickness of the target, as can be seen in the yield equation [1]

$$Y = I \frac{\lambda}{2} \omega \gamma \frac{1}{\epsilon} \left(\frac{A_t + A_p}{A_t} \right) \quad (1.1)$$

where I is the beam intensity, λ the de Broglie wavelength of the beam, $\omega \gamma$ the integrated resonance strength, A_t, A_p the atomic number of the target and projectile, and ϵ the stopping power. The stopping power per hydrogen atom is lower in gas target, and it is estimated that a target containing only hydrogen gas has a yield approximately 5-7 times larger per beam particle than a solid CH_2 target.

Finally, since it is difficult to minimize the charge changing process of ions passing through solid material, a thin window cannot be used to separate the gas from high vacuum in the beam line. Thus, a differentially pumped windowless gas target system was built for use in the DRAGON facility. The details of this system are given in Chapter 3.

The multi-unit electromagnetic separator of DRAGON follows the gas target. It consists of magnetic and electrostatic elements to separate the reaction products from the beam itself, which have similar momentum. This is achieved by selecting one charge state of the beam and the reaction product in the first stage, magnetic dipole. Then, the beam and reaction product of the same charge but slightly different energy ($< 3\%$) are separated using an electrostatic dipole system. Additional separation of the reaction product from the beam is achieved with a second stage of magnetic and electrostatic elements.

Therefore, a key part of the measurement of the absolute cross section of the interaction between the heavy ion radioactive projectile and the gaseous target is a measurement

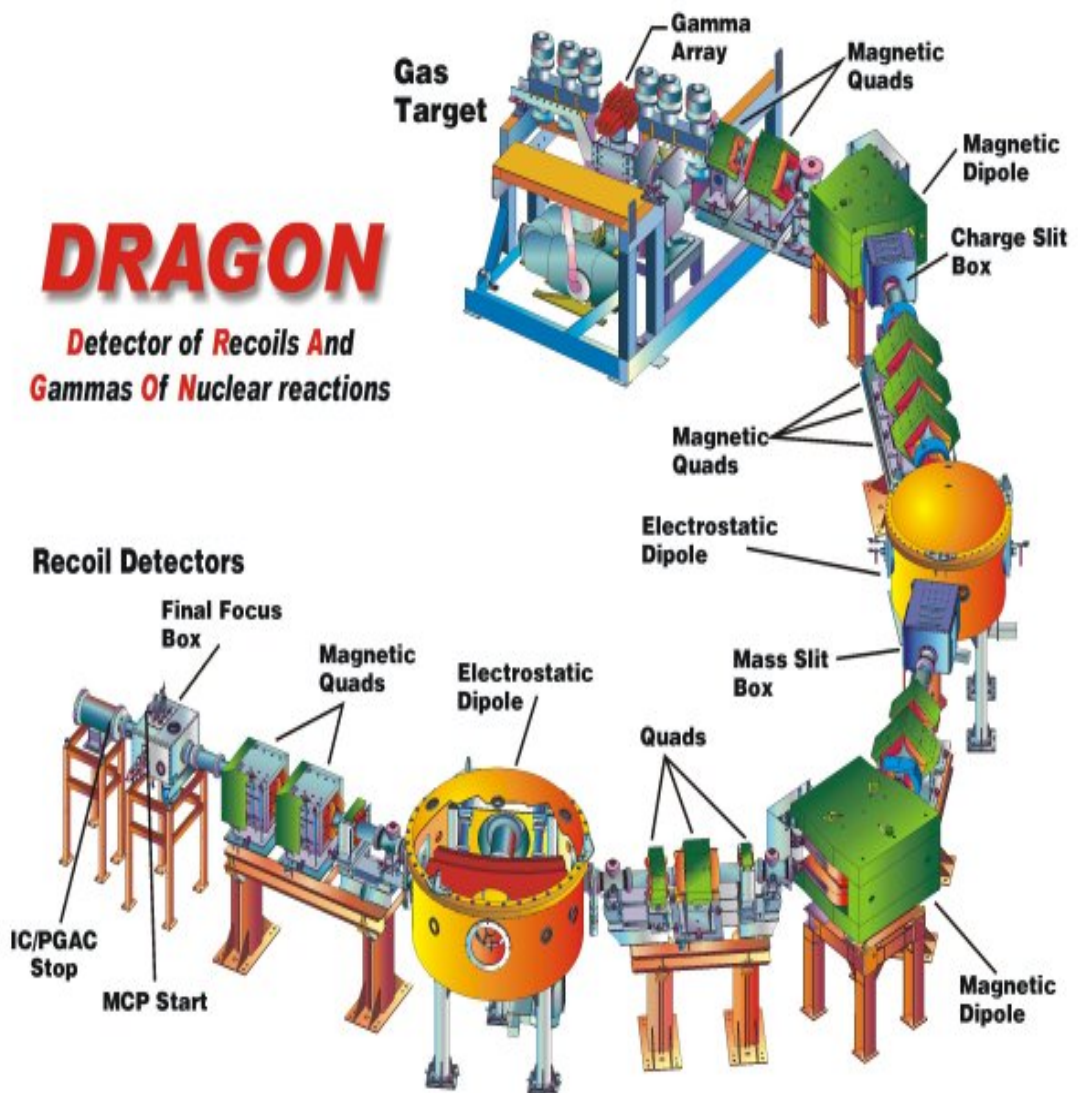


Figure 1.1: Schematic of DRAGON facility at ISAC, TRIUMF

of the charge state distribution resulting from the passage of the low energy heavy ion through the gas. The first DRAGON studies will attempt to measure the reaction rate of the $^{21}\text{Na}(p, \gamma)^{22}\text{Mg}$ using inverse kinematics in the energy range from 0.15 to 1.0 MeV/u. Another very important study is the $^{15}\text{O}(\alpha, \gamma)^{19}\text{Ne}$. It is important then to measure the charge state distribution of sodium, magnesium, oxygen and neon ions moving through hydrogen and helium gas. Related to this is the study of whether this distribution reaches equilibrium in its passage through the gas target at a thickness planned for the DRAGON studies.

A thorough search of the literature revealed that although many studies have been done on charge-changing studies, very little data is available for the passage of low energy (0.15 to 1.0 MeV/u) heavy ions through hydrogen or helium gas. The primary motivation of this thesis is then to measure for the first time the charge state distribution of selected low energy heavy ions passing through a gas target. Those earlier studies will be reviewed to provide a framework in an attempt to formulate some semi-empirical approach, which can then be used in the actual DRAGON studies. Extrapolation or interpolation of the measurements performed herein can provide a foundation for later studies.

1.2 Overview of Charge-Changing Study

Charge-changing of a projectile ion is the result of electron capture and loss from the projectile during the collision with the target atom. In an electron capture process, the projectile picks up one or more electrons from the target atom, while in an electron loss process, the projectile loses one or more electrons, which usually goes into unbound or continuum states.

History of the study of these processes can be dated back to 1922. While tracing out the puzzle of failure to detect α particles of velocity less than about 8×10^6 m/s, Henderson [2] first noticed the change in the charge state of α particle passing through matter.

Since then studies of charge-changing processes attracted a lot of attention, not only because they provide important information about atomic collision and other processes in complex atomic systems, but also because of the numerous requirements for practical uses, such as the radiation detectors, accelerators, storage rings, etc. Especially since the middle of last century, with the availability of energetic beams of ions in different charge states from particle accelerators, the number of studies has grown considerably, both theoretically and experimentally.

The early studies were straightforward, focusing on using low energy light ions, and

later on, in connection with the study of velocity-range relations of fission fragment, heavy ions have been studied extensively. Major results on charge state distribution, experimental techniques, and charge-changing cross sections have been published in a number of review papers and books, e.g., Allison [3], Nikolaev [4], Betz [5], Gillbody [6], Bransden et al. [7], and McDaniel et al. [8]. Compilations of data on charge state distribution and charge-changing cross sections are given by Datz et al. [9], Wittkower et al. [10], Tawara et al. [11], and Wu et al. [12, 13].

Theoretically, with knowledge of a complete set of charge-changing cross sections, the charge state distributions could be predicted. However, the complexity of these atomic collision systems makes such theoretical predictions very unreliable. Even the simplest case, namely, the proton-hydrogen atom collision, has presented a problem of great complexity. Several semi-empirical or empirical formula have been derived from experimental data, however, their application is usually limited to a certain domain, for example, a certain energy range, or, certain projectile and target species.

This lack of an adequate comprehensive theory requires a phenomenological approach before a sufficient complete picture is attained. In this study, we focus on low energy projectiles with atomic number in the range of $7 \leq Z_p \leq 12$.

1.3 Outline of the Following Chapters

Chapter 2 will provide a theoretical review of charge-changing processes and equations defining the cross sections. Then the concept of equilibrium charge state distribution is introduced. Scaling rules of single electron capture and loss cross sections are also discussed.

Chapter 3 gives the details of facilities and experiments performed at Naples University, Italy and DRAGON/ISAC, TRIUMF, Canada. An overview of the data analysis and a summary of major results are given.

Chapter 4 contains the discussion over the results of our experiments, along with the derived semi-empirical formulas.

A conclusion of this study with remarks and suggestion for future studies are presented in Chapter 5.

Chapter 2

Theory of Charge-Changing Process

2.1 Description of Charge-Changing Process

The encounter of an ion of a certain charge state with an atom is a complicated many-body collision system. Phenomenologically, the ion will capture or lose one or more electrons, which causes the change of its charge state after the collision. The probability of these charge-changing processes is described by cross section $\sigma_{q,q'}$ [8] as

$$N_{q'} = N_q x \sigma_{q,q'} \quad (2.1)$$

where N_q is the number of ions in charge state q before the collision, $N_{q'}$ the number of ions that change to charge state q' after the collision, and $\sigma_{q,q'}$ is the cross section for the change from charge state q to q' , in unit of cm^2 . x , the thickness of the target, is the number of target atoms per cm^2 or molecules per cm^2 along the path of ion in the target. For a gas target, thickness derived from the ideal gas law can be expressed as

$$x = \frac{N_A L P}{R T} \quad (2.2)$$

where N_A is Avogadro's number, L the length of the gas cell, P the gas pressure in the cell, R the gas constant and T the temperature of the gas cell. For $T=25^\circ\text{C}$,

$$x = 3.24 \times 10^{16} L(\text{cm}) P(\text{Torr}) \quad [\text{molecules}/\text{cm}^2] \quad (2.3)$$

We also calculated the target thickness from the Van der Waals equation of state given as

$$(P + a(\frac{n}{V})^2)(V - nb) = nRT \quad (2.4)$$

where a is a measure of the attractive force between molecules, and b is due to the finite volume of the molecules. n , P , and V are mole number, pressure and volume of the gas cell, respectively. Using the tabulated Van der Waals constant [14], we recalculated the thickness for hydrogen and helium target at 5.0 Torr and noticed that the difference is less than 0.1% as compared with the result from using ideal gas law.

The charge composition of a beam may be described in terms of the charge state fractions, F_q , where q is the charge state of the ion. The variation of the charge state distribution during the passage through the target can be expressed by a system of linear coupled differential equations

$$\frac{dF_q}{dx} = \sum_{q', q' \neq q} (F_{q'} \sigma_{q', q} - F_q \sigma_{q, q'}) \quad (2.5)$$

where F_q is under the restriction

$$\sum_q F_q = 1 \quad (2.6)$$

The sum includes all the possible charge states. In actual charge state distribution, the fractions of negative and zero charge state (F_0) are really small and negligible if the projectile velocity is not smaller than Bohr electron orbital velocity v_0 ¹. It has been measured that F_0 is less than 2% for heavy ions at around 0.4 MeV [15], and it decreases rapidly when the energy is increased.

Several assumptions have been made in equation (2.5). First of all, only those processes that result in charge changing have been taken into consideration. Processes in which a electron capture followed immediately by a electron loss or the inverse are not included. Also, it has been assumed that the ions and target atoms are in their ground states when the collision happens. In the other word, it is assumed that the target is dilute enough (long mean free path) that the ions in excited states after one collision have enough time to return to their ground state before the next collision. Energy loss in the target is neglected in this simple model.

Under these assumptions, charge-changing cross sections are functions of the projectile species and velocity (or energy), and the target species.

¹ Bohr electron orbital velocity v_0 is the orbital velocity of electron in hydrogen atom, which equals 2.188×10^6 m/s, or equivalently, 0.025 MeV/u.

$$\sigma_{q,q'} = \sigma_{q,q'}(v, Z_p, Z_t) \quad (2.7)$$

where v is the projectile velocity, and Z_p, Z_t refer to the atomic number of projectile and target, respectively. The non-equilibrium and equilibrium distribution can be predicted by a numerical integration of the coupled differential equations (2.5), given a complete set of cross sections.

Target thickness is another important parameter in determining the charge state distribution. Two ways of increasing the target thickness - by increasing the length of target when keeping target pressure constant, or by increasing target pressure when keeping target length constant, are regarded as equivalent under the above assumptions.

Because of the complexity of this process, almost all theoretical calculations have been limited to capture and loss of a single electron. The probability of multiple electron transfer in one single collision has generally been assumed to be very small and negligible, and this has been proved to be a fair assumption in most cases by experimental evidence. For example, the ratio of $\sigma_{q,q-2}/\sigma_{q,q-1}$ amounts to less than $\sim 8\%$ for low energy ^{14}N and ^{16}O ions (~ 0.05 MeV/u) passing through hydrogen gas target [11]. And it is a general observation that the ratio decreases as increasing the projectile energy. Also multiple electron capture process with $n > 2$ is only expected to occur provided that the target atoms contain at least more than n electrons, which is impossible for hydrogen and helium target. The multiple electron loss in one collision is a more probable process compared to the multiple electron capture process. The ratio of measured double and single electron loss cross $\sigma_{q,q+2}/\sigma_{q,q+1}$ is around 12% for 0.357 MeV/u ^{56}Fe beam in hydrogen gas target [11]. It is expected that this ratio decreases as the projectile atomic number decreases. So starting with the simplest, we will use the single electron capture and loss assumption in our study of ^{16}O , ^{23}Na , and ^{24}Mg beams passing through hydrogen and helium gas. As will be discussed later, this turned out to be a good assumption.

2.2 Equilibrium Charge State Distribution

2.2.1 Concepts of Equilibrium Charge State Distribution

Under ideal conditions as discussed in Section 2.1, each charge state fraction of the projectile can reach a certain value which does not change when the target thickness is further increased. This is referred to as the equilibrium charge state distribution.

At equilibrium, $\frac{dF_q}{dx} = 0$, equation (2.5) yields for each charge state q ,

$$\sum_{q', q' \neq q} (F_{q'} \sigma_{q', q} - F_q \sigma_{q, q'}) = 0 \quad (2.8)$$

This implies that the number of particles populating the charge state q is equal to the number of particles depopulating the charge state q .

Equilibrium charge state distribution can be determined by equation (2.6) and (2.8) given the complete set of cross sections. This distribution is a function of the energy of the incoming beam, while independent of the incident charge state of the beam.

When only single electron capture and loss processes are considered, equation (2.6) and (2.8) can be reduced to

$$F_q \sigma_{q, q+1} = F_{q+1} \sigma_{q+1, q} \quad (2.9)$$

No simple relation holds when multiple electron capture and loss cross sections are present.

Two important quantities of the equilibrium charge state distribution are the average equilibrium charge state and the width of the distribution, which are defined respectively as

$$\bar{q} = \sum_q q F_q \quad (2.10)$$

$$d = \sqrt{\sum_q (q - \bar{q})^2 F_q} \quad (2.11)$$

For light target, the equilibrium distribution is close to a Gaussian distribution. The average equilibrium charge state corresponds to the maximum of the distribution. The width of the distribution, d , is related to the full e^{-1} -width, Γ , by

$$\Gamma = 2\sqrt{2}d \quad (2.12)$$

So the Gaussian distribution can be expressed as

$$F_q = \frac{1}{\sqrt{2\pi}d} \exp\left[-\frac{(q - \bar{q})^2}{2d^2}\right] \quad (2.13)$$

Charge state distributions are not always symmetrical. As a measure of the degree of asymmetry, skewness is introduced and defined as

$$s = \sum_q (q - \bar{q})^3 F_q / d^3 \quad (2.14)$$

2.2.2 Average Equilibrium Charge State

Theoretical Calculation of Average Equilibrium Charge State

The first theoretical estimations of average charge state were given by Bohr [16, 17] and Lamb [18] independently.

As regards the average charge state, Bohr assumed that a fast heavy ion penetrating through dilute gas retains all of its electrons that have orbital velocities greater than the velocity of the ion. The electrons with smaller velocity are torn off during the collision, whereas the removal of electrons of higher velocity is very improbable since for such electrons the collision is adiabatic. For \bar{q} close to, but not larger than $Z_p/2$, Bohr derived the well-known formula

$$\frac{\bar{q}}{Z_p} = \frac{v}{v_0 Z_p^{2/3}} \quad \left(1 < \frac{v}{v_0} < Z_p^{2/3}\right) \quad (2.15)$$

where v is the projectile velocity, v_0 the Bohr orbital velocity and Z_p the projectile atomic number.

When applying Bohr's criterion to the extreme cases where \bar{q} approaches Z_p , one would expect that the ions become almost fully stripped at velocities $v \simeq v_0 Z_p^{2/3}$. This has been verified experimentally by Heckmann [19] for ions with $Z_p \leq 18$.

Independent of Bohr's work, Lamb determined the average charge state by energy consideration. He assumed that the electrons will be stripped off until the ionization energy potential of the next ionization stage is greater than the kinetic energy of target electrons, which, in the projectile reference frame, bombard the projectile with a velocity v . The outermost electron that remains in the projectile ion is referred to as the characteristic electron.

Theoretically, Lamb's assumption would be identical to Bohr's if the characteristic electron velocity determined by the ionization potential is equal to the corresponding electron orbital velocity. This would be true if all electrons move in a Coulomb field and the Virial theorem can be applied to each electron in the ion. However, the Virial theorem is valid only for the total ion and not for each individual electron [20]. When comparing to experimental data, the Lamb curve turns out to be a better assumption, which indicates the importance of ionization energy to the stripping processes.

Although in their considerations, the binding energy of electrons of the target atoms and any other specific effects of the target atoms have been neglected, Lamb and Bohr's assumption (referred to as LB criterion) serves as a very important first-order approximation for further theoretical and semi-empirical treatments.

Further improvement of the statistical models has been done by Knipp, Teller [21] and Bell [22] in determining the relation between the characteristic electron velocity and the projectile velocity. More detailed calculation turned out to be more complex, but not much better agreement with experimental result has been achieved. The problem of relating the characteristic electron velocity to the projectile velocity remains uncertain.

Semi-empirical formula for Average Equilibrium Charge State

Quantitatively, the limited theoretical calculations are in fair agreement with experimental results. However, none of those theories allow the prediction of \bar{q} with sufficient accuracy and over large ranges of projectile species, velocity and target species.

For practical reason, considerable attention has been devoted to the development of the semi-empirical formula for average equilibrium charge state and the equilibrium charge state distribution width based on simple theoretical grounds.

In case of average equilibrium charge state, LB criterion has been generally used as a basis for further derivation of semi-empirical formulas. From this point, the average equilibrium charge state of the projectile is believed to be a function of the incoming velocity v and Z_p^α , where $\alpha = \frac{2}{3}$ under Bohr's assumption.

In 1963, Heckmann et al. [19] measured the equilibrium charge state distribution of fast ions (C, N, O, Ne) with energy in the range of 1.59 to 10.50 MeV/u passing through zapon (cellulose nitrate) foil. It is found that if \bar{q}/Z_p is plotted as a function of v_e/Z_p^α , where v_e is the characteristic velocity of outmost electron within the projectile ion, α can be chosen so that a universal curve is obtained for all ions. They determined α to be 0.55 when assuming v_e to be the velocity of the energetically most easily removable electron. It is also indicated that if the ratio of v_e to velocity of the ions v is the same for all ions, \bar{q}/Z_p will also be a universal function of v/Z_p^α , and α is estimated to be in the range of 0.55 to 0.58. A plot of the experimental value $\ln(1 - \frac{\bar{q}}{Z_p})$ versus $v/Z_p^{0.55}$ showed a linear relation.

Betz et al. [23] followed Heckmann's suggestion. They derived a semi-empirical formula for average charge state based on experimental data of fast heavy ions ($Z_p \geq 10$, $5 < E < 80$ MeV) passing through gas and foil stripper. The average equilibrium charge state \bar{q} is expressed as

$$\frac{\bar{q}}{Z_p} = 1 - C \exp\left(-\frac{v}{v_0 Z_p^\gamma}\right) \quad (v \geq v_0) \quad (2.16)$$

where C and γ are determined empirically for different projectile and target combinations as listed in Table 2.1. They argued that for gaseous targets, the choice of constant values $C = 1$

Table 2.1: Experimental result from Betz et al. for parameter C and γ

	<i>Air-Stripper</i>		<i>Formvar-Foil-Stripper</i>	
Ion	C	γ	C	γ
S	1.135 ± 0.049	0.663 ± 0.016	1.083 ± 0.020	0.604 ± 0.007
As	1.117 ± 0.007	0.628 ± 0.003	1.098 ± 0.006	0.538 ± 0.002
I	1.065 ± 0.004	0.641 ± 0.003	1.030 ± 0.002	0.518 ± 0.002
U	—	—	1.030 ± 0.002	0.510 ± 0.002

and $\gamma = \frac{2}{3}$ gives reasonable estimation for \bar{q} . This also agreed with the previous theoretical equation (2.15) when $v/(v_0 Z_p^\gamma) \ll 1$.

Meanwhile, extensive experimental data of heavy ions (Br, I, Ta, and U) passing through carbon foil at energy above 100 MeV has been used by Nikolaev and Dmitriev [24]. They developed a universal formula for average equilibrium charge state of ions stripped in solid target as

$$\frac{\bar{q}}{Z_p} = [1 + (\frac{v}{v' Z_p^\alpha})^{-\frac{1}{k}}]^{(-k)} \quad (2.17)$$

where $\alpha = 0.45$, $k = 0.6$, $v' = 3.6 \times 10^6$ m/s. They argued that, compared to the previous expression of the type $\frac{\bar{q}}{Z_p} = A - B \exp(-\frac{v}{v' Z_p^\alpha})$, this expression gives better agreement with experiment data. In addition, it is also able to give the expected proportionality between \bar{q} and v when v is small, while the previous one can not if $A \neq B$. The usefulness of equation (2.17) is evident, as shown in Figure 2.1, when plotting all the experimental data \bar{q}/Z_p versus $v/(v' Z_p^{0.45})$ for solid target. Most of the data falls within a narrow band around the line predicted by equation (2.17).

The success with solid target encouraged the similar description for average equilibrium charge state in gaseous targets. The relative average charge state \bar{q}/Z_p has been plotted as a function of the reduced velocity $v/(v_0 Z_p^{0.55})$ [5] as shown in Figure 2.2. Because of the scattering of the data, a universal exponent is hard to choose.

With the availability of more experimental data, some modification has been made on these semi-empirical formulas. Shima et al. [25] discussed the oscillation of \bar{q} with Z_p and v , and did a fit for \bar{q} through carbon foil using the expression

$$\bar{q} = Z_p [1 - \exp(-\sum_i a_i x^i)] \quad (2.18)$$

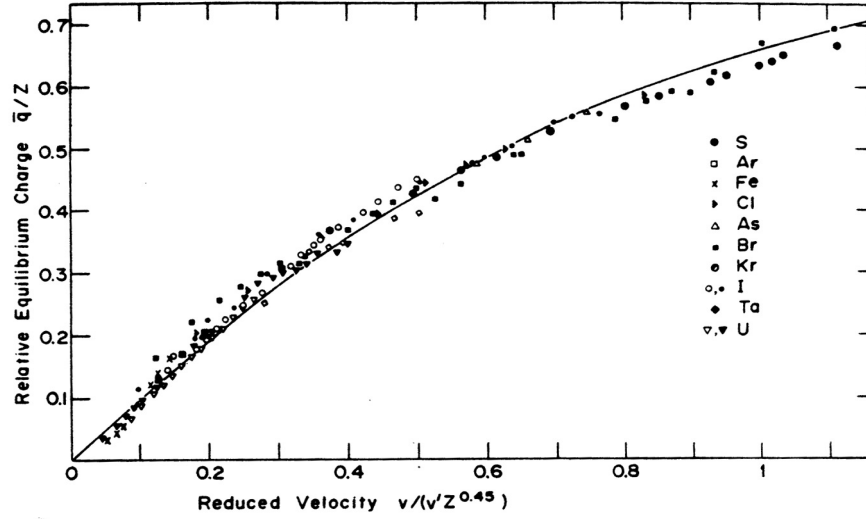


Figure 2.1: Average relative equilibrium charge of ions passing through carbon (solid symbol) and other light foils (open symbol) plotted as a function of the reduced velocity $v/(v'Z^{0.45})$, with $v' = 3.6 \times 10^6$ m/s, and Z is the projectile atomic number. The solid line represents the semi-empirical estimation by Nikolaev and Dmitriev (equation (2.17))[5].

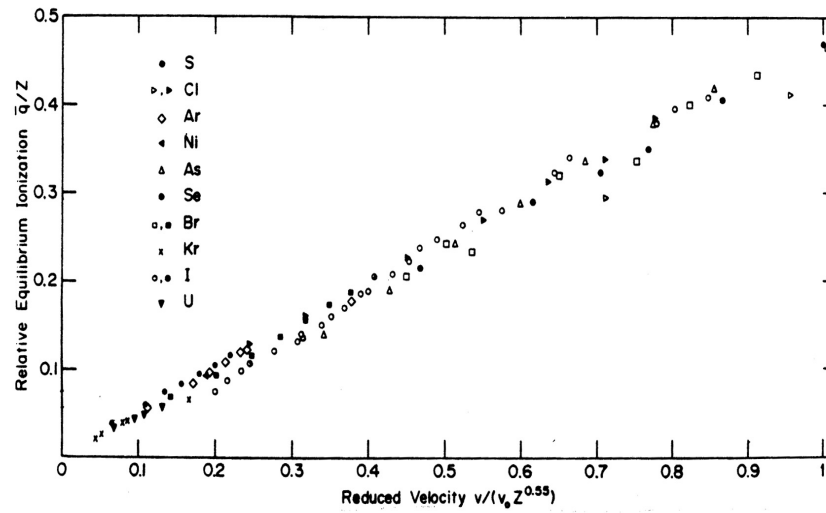


Figure 2.2: Average relative equilibrium charge of ions passing through gaseous target of nitrogen, oxygen and air, plotted as a function of the reduced velocity $v/(v_0Z^{0.55})$, with $v_0 = 2.188 \times 10^6$ m/s, and Z the projectile atomic number. The solid and open symbols refer to dense and more dilute gas target, respectively[5].

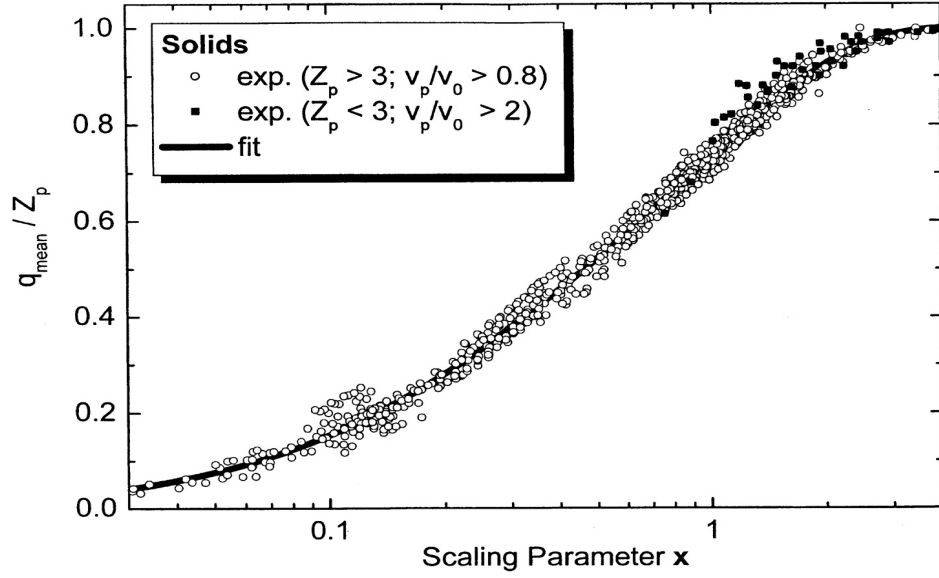


Figure 2.3: Average relative equilibrium charge of ions passing through solid target plotted as a function of the reduced scaling variable x [27].

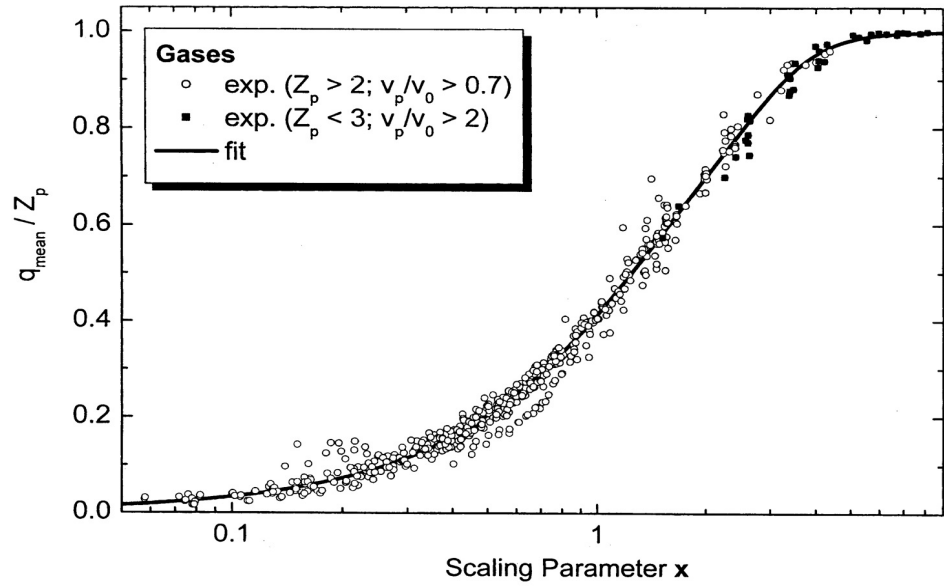


Figure 2.4: Average relative equilibrium charge of ions passing through gaseous target plotted as a function of the reduced scaling variable x [27].

where $x = (v/v'Z_p^{0.45})$, $v' = 3.6 \times 10^6$ m/s.

In case of sodium ion at the exit of a carbon foil for energy ranging from 0.43 to 1.66 MeV, X. Tordoir et al. [26] limited the sum to the first two terms of equation (2.18) and found a good fit is obtained with $a_1 = 0.96 \pm 0.03$ and $a_2 = 1.05 \pm 0.13$.

Most recently, G. Schiwietz and P.L. Grande [27] determined two improved charge state fits, which take the target species as one of the parameters in the consideration. A multi-parameter least squares fit has been performed to find a reduced parameter x that minimizes the scatter of \bar{q}/Z_p around a smooth curve. One formula for projectiles ranging from protons to uranium for gas target (fitted to experimental data for target atomic number $Z_t = 1$ to 54) is found as

$$\frac{\bar{q}}{Z_p} = \frac{376x + x^6}{1428 - 1206x^{0.5} + 690x + x^6} \quad (2.19)$$

with

$$x = (v_p/v_0 Z_p^{-0.52} Z_t^{0.03 - 0.017 Z_p^{-0.52} v_p/v_0})^{1 + 0.4/Z_p}. \quad (2.20)$$

And a similar one for solid target (fitted to experimental data for Be to Bi target) is also determined as

$$\frac{\bar{q}}{Z_p} = \frac{12x + x^4}{0.07/x + 6 + 0.3x^{0.5} + 10.37x + x^4} \quad (2.21)$$

with

$$x = (v_p/v_0 Z_p^{-0.52} Z_t^{-0.019 Z_p^{-0.52} v_p/v_0} / 1.68)^{1 + 1.8/Z_p}. \quad (2.22)$$

Note that only fast projectile with $v > 2.8v_0$ have been included in the fit since at very low velocity the details of the target and projectile shell structure come into play. The corresponding resonant electron capture processes depend significantly on the target projectile combination and a simple scaling behavior is not available. The fits are shown in Figure 2.3 and 2.4.

With these semi-empirical formulas, it may be possible to interpolate, and to some extent, extrapolate the existing data on \bar{q} . However the uncertainty is normally higher than 10%.

2.2.3 Charge State Distribution Width

For a comprehensive description of the equilibrium charge state distribution, it is necessary to understand not only the average charge state, but also the distribution around the average. The LB criterion is a good approximation of the average, however it gives no information for the neighboring charge states. The major attempts to predict the charge state distribution are based on phenomenological description of the regularities observed in numerous experimental data.

In case of light targets, especially hydrogen, distributions are comparably narrower and more symmetrical. They are closely approximated by the Gaussian distribution as expressed by equation (2.13).

Thus, a reasonable estimation will be available once the average equilibrium charge state, \bar{q} , and the distribution width, d , are known. Asymmetry is not a serious factor in our study and is neglected in the discussion here.

It is a common observation that the distribution widths are, in wide range of ion velocities, practically independent of v , except at very low ($\leq 0.1/Z_p^{0.5}$ MeV/u) and very high ($\geq 0.06Z_p$ MeV/u) energy, where d becomes very small. There exist several semi-empirical formulas of d , but each of them is valid only within a certain domain. Dmitriev and Nikolaev [5] derived the estimation

$$d = d_1 Z_p^w \quad (2.23)$$

where parameters d_1 and w have been determined semi-empirically to be 0.32 and 0.45 in nitrogen and argon gas, and be 0.38 and 0.40 in solids. Later, Nikolaev and Domitirev [24] presented a new formula for solid strippers as

$$d = d_2 \left\{ \bar{q} \left[1 - \left(\frac{\bar{q}}{Z_p} \right)^{\frac{1}{k}} \right] \right\}^{\frac{1}{2}} \quad (2.24)$$

where d_2 and k were determined to be 0.5 and 0.6, respectively. This has been proved to be a useful approximation by Ryding et al. [28] and Wittkower et al. [29] for heavy ions ($Z_p < 92$), stripped in oxygen gas and in carbon foil at energy below 20 MeV. However, for fast ions, equation (2.24) generally gives unsatisfactory results.

Other expressions have been given independently by Betz [30], Sayer [31], and Baudinet-Robinet [32]. However, the data of experimental distribution width often scatter considerably, and the influence of the target species, the shell effects and the asymmetries of the distribution present additional complications.

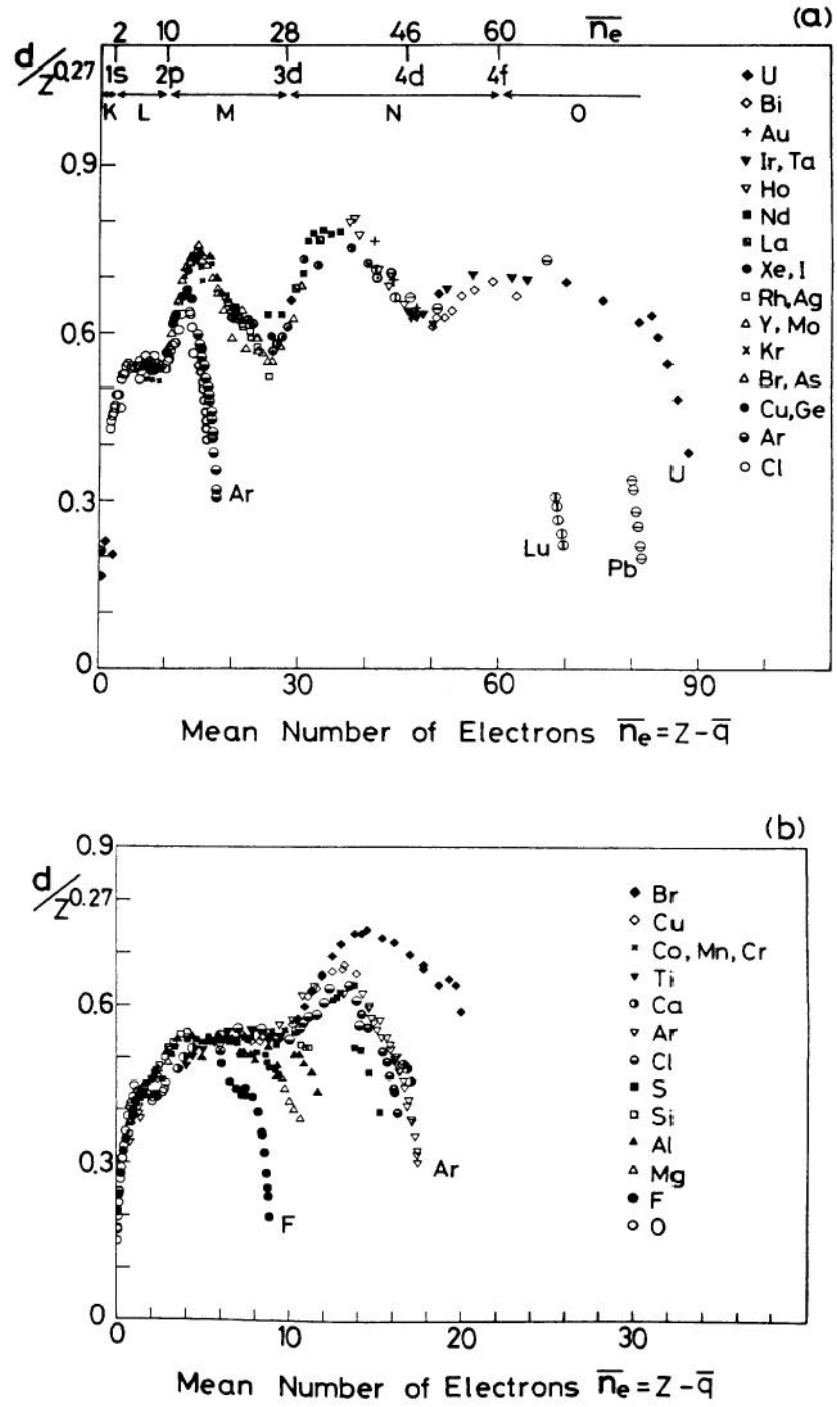


Figure 2.5: Universal plot of reduced width for various ions as a function of mean number of electrons attached to the ions $\bar{n}_e = Z_p - \bar{q}$. The details of (a) at $\bar{n}_e < 20$ are given in (b)[25].

The correlation of the oscillation of distribution width to the shell structure has been studied extensively by Shima et al. [25]. It has been noticed that the width of the charge state distribution in which outermost electrons are distributed mainly in the L shell ($\bar{q} \geq 19$), are smaller than those mainly in the M shell ($\bar{q} \leq 18$). They argued that the variation of the width d versus Z_p or v is dominated by the variation of the shell retaining the outermost electron of the ions. So the scaling of d is attained when classifying d in terms of an average number of electrons $\bar{n}_e (= Z_p - \bar{q})$ instead of \bar{q} as shown in Figure 2.5. The reduced width $d/Z_p^{0.27}$ is taken since the presence of the relation

$$d = 0.53Z_p^{0.27} \quad (n_e < 10) \quad (2.25)$$

It is also indicated in Figure 2.5 that d values rise sharply from the limit of $\bar{n}_e = Z_p$ at zero velocity until they join the scaled oscillatory curve of d , and finally d approaches 0 at the high velocity limit ($\bar{n}_e = 0$).

Schiwietz et al. [27] extend the scaling to different solid-state target species. Based on previous works, they determined a reduced width w as

$$w = dZ_p^{-0.27}Z_t^{0.035-0.0009Z_p}f(\bar{q})f(Z_p - \bar{q}) \quad (2.26)$$

with

$$f(x) = \sqrt{(x + 0.37Z_p^{0.6})/x} \quad (2.27)$$

w is around 0.7 as shown in Figure 2.6. The Z_p dependence dominates the general trend of the data and the function f serves to correct for the statistical reduction of the width at either very low or very high energy. Although the general trend is obvious, the scattering of the data makes the accurate determination of a certain width impossible. To the best of our knowledge, universal scaling rule of the distribution width for a gas target has not been done.

2.3 Cross Section

Charge-changing cross sections provide the fundamental basis for all accurate and complete descriptions of the ionic charge states produced in an ion-atom encounter.

Numerous investigators have devoted considerable effort to theoretical estimations and experimental measurements of these cross sections. However, the processes involving the

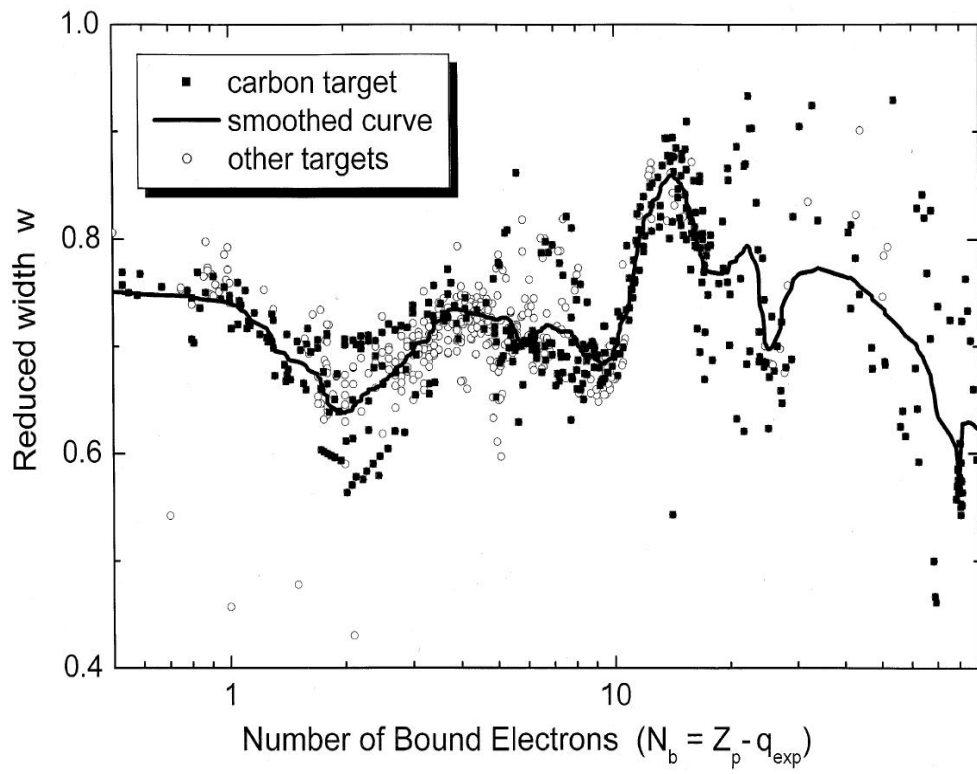


Figure 2.6: Universal plot of reduced width for various ions as a function of mean number of electrons attached to the ions for solid target[27].

capture and loss of electrons by heavy ions are generally so complicated as to preclude precise and comprehensive theoretical descriptions. The difficulties of such calculation can be readily seen when one considers the very large matrix made of different charge changing cross sections, not to mention the number of electronic excitation configurations which are energetically possible in these interactions.

Free Collision Approximation

The major part of the theoretical work has been based on simplified models, which are valid only in restricted regions of the basic parameters Z_p, v, q , and Z_t . The details of those classical and quantum theoretical treatments can be found elsewhere. Here only a brief description of Born and Lindhard's early work will be given. Their work serves as a first-order assumption in the later study of the scaling rules of the cross sections.

Bohr [33] argued that, especially when the orbital dimensions of the target electrons are larger or comparable to those of the electrons to be lost from the ion, the ionizing effects of the electrons and nucleus of the ions are approximately independent of each other. This is the so-called free collision approximation where the binding force is neglected, and basically is valid when the ion velocity is large compared to the Bohr electron orbital velocity v_0 .

Bohr and Lindhard [34] presented an interpretation of electron capture and loss of highly charged ions by applying simple mechanical consideration partially based on this approximation.

Electron loss has been considered as an ionization process. By summing up the cross section of transferring energy greater than $m_e u^2/2$ to an electron in a collision over all electrons with orbital velocities $u \leq 2v$ (v the projectile velocity), they determined an expression for single electron loss as

$$\sigma_{q,q+1} = \pi a_0^2 Z_t^{\frac{2}{3}} Z_p^{\frac{4}{3}} q^{-3} \left(\frac{v}{v_0}\right)^2 \quad (2.28)$$

where a_0 is the Bohr radius ($a_0 = 0.529 \times 10^{-10}$ m).

As regards electron capture, Bohr emphasized in his earlier work that it is more difficult since at least three particles take part in the exchange of energy and momentum. Following Born approximation, electrons are preferentially captured when their initial orbital velocities are close to the projectile velocity. For electron capture by heavy projectiles in light target gas, they explained the possibility of capture of weakly bound target electrons on the

basis that electron release is a gradual process. Thus there is a small chance that a loosely bound electron will remain with the atom until the highly charged ions approached closely enough that the capture can take place. They gave a cursory estimation

$$\sigma_{q,q-1} = \pi a_0 q^3 \left(\frac{v_0}{v} \right)^7 \frac{\mu^{*2}}{\mu^3} \quad (2.29)$$

where μ^* and μ characterize screening effects in the target atom and an effective quantum number, respectively.

Deriving Cross Sections from Measured Charge State Distribution

For experimentalists, it is usually more straightforward to measure the charge state distribution. The cross sections can be derived from the measured distribution basically by two methods – the slope method and the least squares method.

The slope method has been widely used to determine the cross sections from the linear part of the non-equilibrium distribution, where mainly single collision occurs. To apply this method, three conditions must be met: incident beam consists of one pure charge state q ; the target thickness is precisely measured at really small values, namely of order 10^{14} atoms/cm² (or say, target pressure of the order of mTorr); the total amount of the residual gas must be small and negligible even for the smallest target thickness. Under these restrictions, we can calculate the cross section $\sigma_{q,q'}$ by measuring the presence of charge state other than q , namely as

$$F_{q'} = \sigma_{q,q'} x \quad (q \neq q') \quad (2.30)$$

where q is the incident charge state, and x the target thickness as defined in equation (2.3).

The drawbacks of this method mainly lie in two aspects. First of all, appreciable deviations from linearity occurs at a thickness where the fraction of the incident beam F_q is still more than 90%. Consequently, a linear fit may easily introduce errors of 10~20% in the determination of a single capture or loss cross section. Another serious problem arises from the residual gas, especially when its cross sections differ a lot from that of the target gas.

A more comprehensive determination of the cross sections can be managed by the least squares method provided a sufficient number of charge state distributions are measured. Residual gas problem is not that serious as long as it is negligible at greater target thickness. And no requirement is placed on the incident charge state of the projectile.

With the incident charge state distribution and a set of cross sections as initial parameters, equation (2.5) can be integrated numerically. The charge fractions calculated at a certain target thickness is compared to those measured using the least squares sum

$$\chi^2 = \sum_{q=1}^{q_{max}} W_q (F_q - Y_q)^2 \quad (2.31)$$

where F_q, Y_q are the experimental and calculated charge fractions, and W_q the weighing factor chosen with respect to the experimental uncertainty. The sum runs over the charge fractions measured for all charge state at different target thickness for a certain projectile and target combination. The cross sections can be determined by minimizing χ^2 , regarding all cross sections as free parameters in calculating charge fractions Y_p . With enough experimental data, a complete set of cross sections can be obtained.

Scaling rules for Cross Section

Knowledge of the experimental charge-changing cross sections is useful for testing theoretical calculations as well as for a variety of applications. Given the vast number of combinations of projectile species, energy and charge state, and the large number of possible gas and vapor targets, scaling rules obtained from experimental data are useful, if they exist, for predicting the magnitude of unmeasured cross sections.

To obtain a universal scaling rule, several parametric studies must be made including the dependence of cross sections on projectile atomic number Z_p , projectile energy E , projectile incident charge state q , and target atomic number Z_t .

Berkner et al. [35] found that for single electron capture by fast highly charged iron ions in a hydrogen gas target, the cross section can be expressed as

$$\sigma_{q,q-1} = 1.2 \times 10^{-8} q^{3.15} E(keV/u)^{-4.48} \quad [cm^2/atom] \quad (2.32)$$

for projectile energies greater than 275 keV/u. And later, a universal empirical scaling rule for electron capture in gas target for intermediate energy ions ($0.3 < E < 8.5$ MeV/u) has been found by Schlachter et al. [36] as

$$\tilde{\sigma} = \frac{1.1 \times 10^{-8}}{\tilde{E}^{4.8}} [1 - \exp(-0.03\tilde{E}^{2.2})] \times [1 - \exp(-2.44 \times 10^{-5}\tilde{E}^{2.6})] \quad (2.33)$$

where $\tilde{\sigma}, \tilde{E}$ is the reduced cross section and energy defined as

$$\tilde{\sigma} = \sigma_{q,q-1} Z_t^{1.8} / q^{0.5} \qquad \tilde{E} = E / (Z_t^{1.25} q^{0.7}) \qquad (2.34)$$

with $\sigma_{q,q-1}$ in cm^2 and E in keV/u.

No universal scaling rule on single electron loss cross section has yet been published upon our knowledge.

Chapter 3

Experiment

3.1 Naples Experiment

At Naples University, we measured the charge state distribution of ^{16}O and ^{23}Na beams passing through hydrogen gas target and ^{16}O beam passing through helium gas target. The combinations of projectile energy and incident charge state are listed in Table 3.2. For each combination, the charge state distributions have been measured at several target pressure points, corresponding to the distribution from non-equilibrium to equilibrium.

A schematic diagram of the facility [37, 38] is shown in Figure 3.1. Negative ion beam produced by a cesium sputter ion source is selected by a 35° inflection magnet (mass resolution $m/\Delta m = 30$), and accelerated by the 3MV tandem accelerator. The positive ions of selected charge state emerging from the accelerator are focused by a magnetic quadrupole doublet on the object slits of a 90° analyzing magnet. The double focusing analyzing magnet focuses the beam on the image slits and a downstream magnetic quadrupole doublet focuses the beam on the center of the gas target system. The ion beam exiting the gas target is transported through a magnetic quadrupole triplet and a 30° switching magnet.

Faraday cups (FCs) are installed along the beam line to monitor the beam transportation. The measurement is performed by first reading the incident beam intensity from FC3, which is located upstream of the gas target. Total intensity of beam exiting the target is measured by FC4. The beam intensity of different charge states is measured using FC5 by scanning the switching magnet. Neutral particles have been neglected since they are not detectable by the switching magnet and also for the reason discussed in the section 2.1. Beam transmission was high with minimal loss from scattering and charge states were easily separated by scanning the magnet. However, major uncertainties were introduced as the

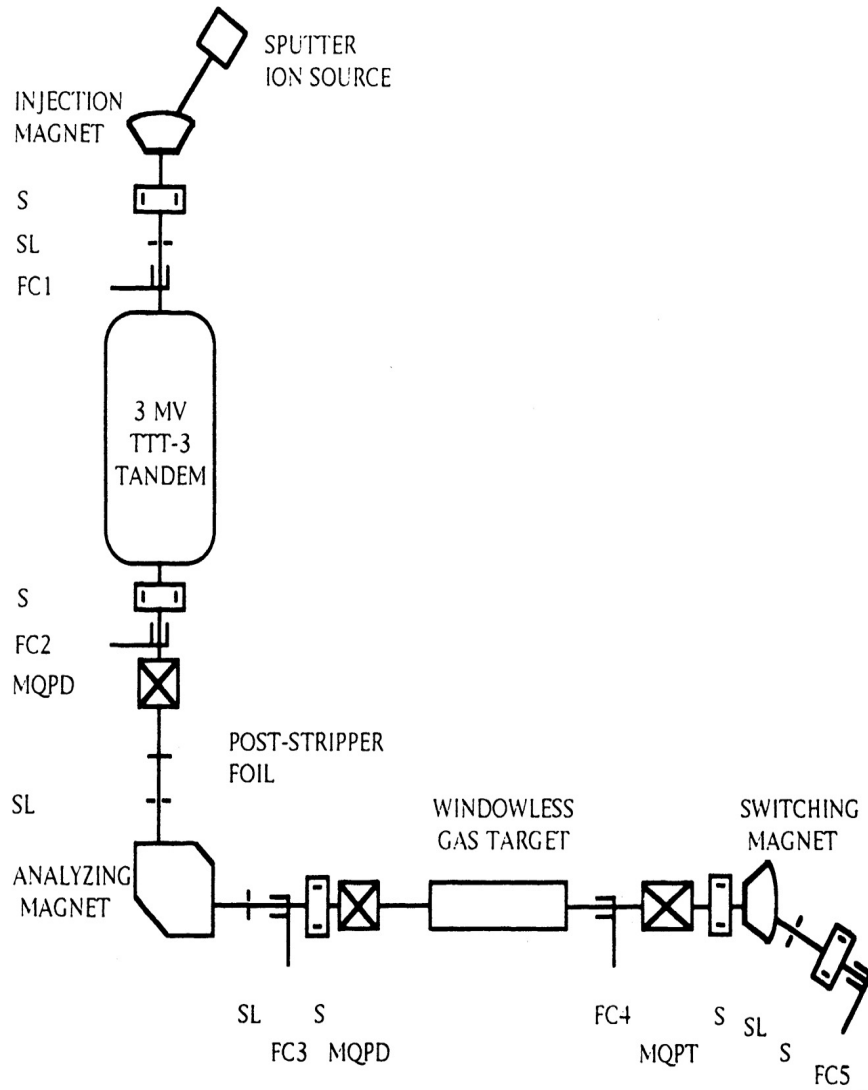


Figure 3.1: Schematic diagram of Naples facility, Italy[37, 38]. (S = X-Y steerers, SL = slits, FC = Faraday cup, MQPD = magnetic quadrupole doublet, MQPT = magnetic quadrupole triplet.)

magnet scanning and beam tuning were conducted manually by different persons on shift.

Energy loss of the beam is estimated as

$$\Delta E = E \times \left(1 - \frac{B_q^2(p)}{B_q^2(0)}\right) \quad (3.1)$$

where E is the energy of the incoming beam, $B_q(p)$ and $B_q(0)$ the switching magnet reading at zero pressure and non-zero pressure p for a certain charge state q , respectively.

Before loading gas into the target chamber, the beam transmission and residual gas were checked. The readings of FC3 and FC4 showed that the intensity of beam entering and exiting the target agreed well within uncertainties, which indicated a good transmission. However, when scanning the magnet, we noticed the beam exiting the target chamber already established a charge state distribution with the initial incident charge state fraction lowered to about 70%. It is estimated that the residual gas in the transportation line and target chamber added up to a gas thickness around 3×10^{15} molecules/cm². After installing another pump on the downstream side of the analyzing magnet, this situation was improved. The residual gas thickness was reduced to around 1×10^{15} molecules/cm². This residual gas problem introduced a large error in the measurement of the charge state distribution at low target thickness.

Beams of the same energy but different charge state are required to check the dependence of charge state distribution on incident charge state and also for calculating the complete set of charge-changing cross sections. A post-stripper (carbon foil, $10 \mu\text{g}/\text{cm}^2$) has been installed in front of the object slits (downstream the analyzing magnet). Accelerated beam of a certain charge state is further stripped before entering the analyzing magnet and transported to the gas target. With this we have managed to measure the charge state distribution of ^{16}O beam with incident charge state 2+, 3+, 4+, 5+, and of ^{23}Na beam with incident charge state 3+, 4+, 5+, 6+, 7+.

3.2 DRAGON/ISAC Experiment

DRAGON, located in the ISAC hall (Figure 3.2), is a new facility and is presently being commissioned. The charge state distribution study represents the first time beam passed through the gas target.

To complete our study and also to check the reproducibility of charge state distribution using different systems, we measured the charge state distribution of ^{15}N , ^{16}O and ^{24}Mg ions passing through the hydrogen gas target.



Figure 3.2: Plan view of ISAC experimental hall, TRIUMF, Canada

3.2.1 ISAC Heavy Ion Accelerator

Stable beam required for this study is produced by the Off-Line Ion Source(OLIS) and delivered by the all electrostatic Low Energy Beam Transport (LEBT) to the 35 MHz Radio Frequency Quadrupole (RFQ). The RFQ is commissioned to accelerate beams of $A/q \leq 30$ from 2 keV/u to 153 keV/u. Then the beam is stripped to $3 \leq A/q \leq 6$ by the post stripper in the medium energy transport (MEBT) system and accelerated to a final energy between 0.153 MeV/u to 1.53 MeV/u at the end of the 106 MHz variable energy drift tube linac (DTL).

The high energy beam transport (HEBT) delivers the beam from the DTL to the experiment stations like DRAGON. It is composed of four basic sections: a section to match the beam from DTL to HEBT, a diagnostic and bunching section, an achromatic bend section to deliver the beams to the experiments and a matching section to focus the beam to the experimental target.

To maintain a sharply pulsed energy and time structure, bunchers and choppers are installed along the beam line.

3.2.2 DRAGON Facility

A schematic diagram of the units of DRAGON used for the charge state distribution studies is shown in Figure 3.3.

Beams of desired energy, mass and charge state produced by the ISAC accelerator are delivered to DRAGON. Typical beam intensity is $10^{11} \sim 10^{12}$ electrons/sec. The transmission of the beam is checked by tuning the beam through the system without gas in the target. The transmission is $\geq 98\%$. Also, charge analyzing of the beam at the exit of the target showed more than 99% of the beam is of the original incident charge state, which indicates that the residual gas is negligible.

The total intensity of beam entering the target is measured by the Faraday cup (HEBT:FC4), which is installed upstream of DRAGON's target in HEBT's last section. Another Faraday cup (FC1) located downstream of the target measured the total intensity of beam exiting the target. The intensity of a certain charge state is determined by scanning the magnetic dipole (MD1) and collecting it at the Faraday cup (FCCH) after the magnet. The output of the Faraday cups is integrated by the digital current integrator set at 10^{-10} coul/pulse. Each measurement of pulse-counting from the Faraday cup is conducted for a time sufficient to achieve reasonable statistics ($< 3\%$ except for really low counting rate). For each beam

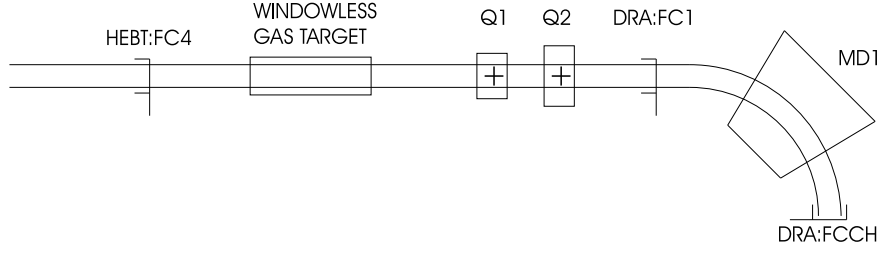


Figure 3.3: Schematic diagram of the set-up for the charge-state distribution study using DRAGON facility

energy, measurement at several pressure points has been done.

The scan of MD1 is done automatically corresponding to a reference file and taking the beam energy at the exit of target and charge state as input parameters. Before charge state distribution measurements, energy scan of each beam was done at zero target pressure and another high pressure (around 4.5Torr) using MD1. Energy loss of the beam within the target is estimated to be the difference between two peak energies of the scans. This has been checked with the SRIM (the Stopping and Range of Ions in Matter) [39] calculation and has been used to estimate the beam energy at different pressures during the charge state distribution measurements.

3.3 The Windowless Gas Target

3.3.1 Naples Target System

At Naples University, the windowless gas target is run in a flow-through mode. The differentially-pumped target system has three pumping stages on each side of its gas chamber, as shown in Figure 3.4. They consist of Roots blowers (e.g. WS2000, pumping speed = 2000 m³/h), turbo pumps (e.g. TV360, pumping speed = 360 l/s), and roughing pumps (e.g. D65B, pumping speed = 65 m³/h). For the cell pressure of 5.0 mbar with hydrogen gas, the three-stage pumping system can sequentially reduce the pressure outside the gas chamber to $p_1 = 0.20$ mbar, $p_2 = 6.5 \times 10^{-4}$ mbar, $p_3 = 1.6 \times 10^{-5}$ mbar, respectively. The beam enters the target chamber through three electrically insulated apertures with diameters of 5 mm, 8 mm, and 10 mm, respectively. The pressure inside the target chamber is measured by a baratron capacitance manometer to an accuracy of 4%.

The disk-shaped target chamber has an outer radius of 175 mm. The central ion-beam pipe of 12 mm diameter hosts the apertures A and A', whose centers are 124 ± 1 mm from

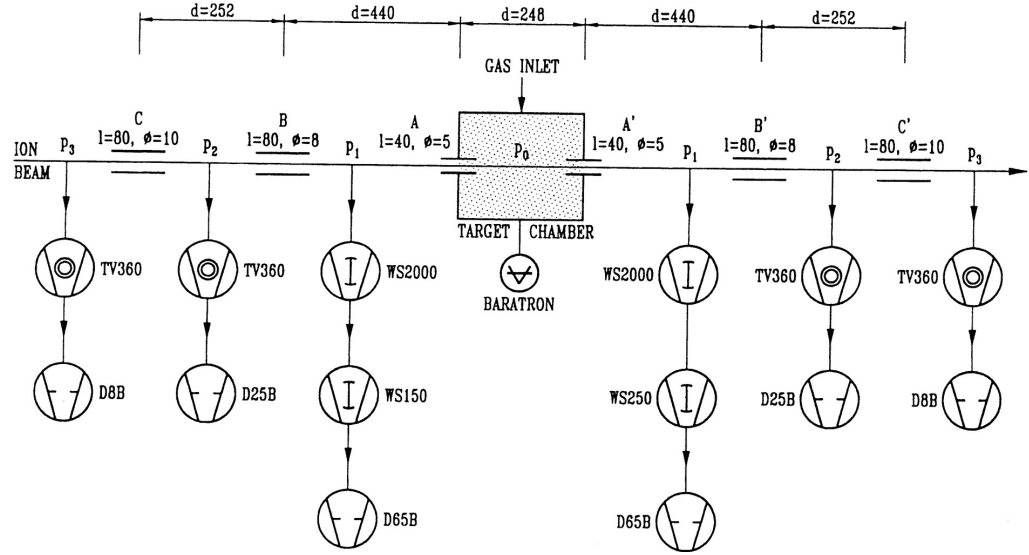


Figure 3.4: Schematic diagram of the differentially-pumped gas target system at Naples, Italy[40].

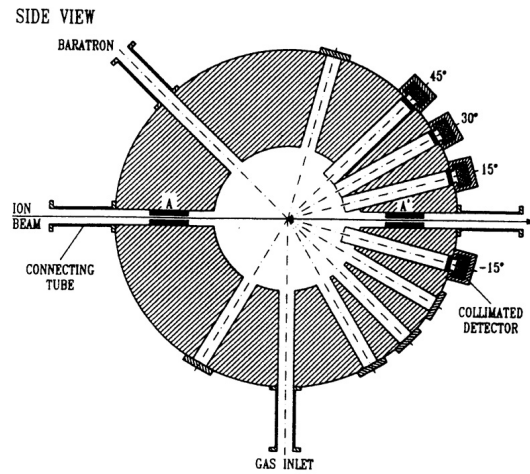


Figure 3.5: Schematic diagram of the target chamber of Naples target system. The distance between the centers of apertures A and A' is 248 ± 2 mm[40].

the center of the chamber. The detailed structure of the chamber is shown in Figure 3.5. Several ports radiate from the center of the chamber. They are used for gas inlet, adapter for the baratron manometer, and installation of collimated particle detectors at the scattering angles $\theta_{lab} = 45^\circ, -45^\circ$ and -75° .

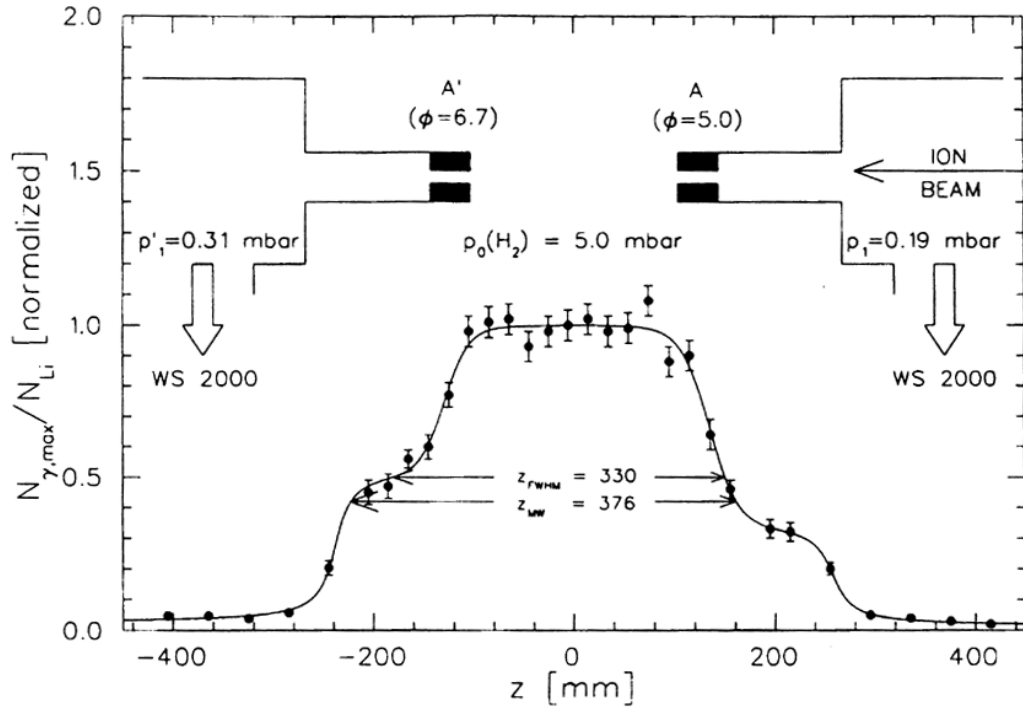


Figure 3.6: Pressure profile of H_2 gas (with cell pressure at 5.0 mbar) along the beam axis, as taken from [40].

The $p(^7Li, \gamma)^8B$ capture reaction has been used to measure the pressure profile of the H_2 in target chamber [40] as shown in Figure 3.6. It is determined that there is a constant pressure plateau at the center region of the target chamber, and a relatively sharp pressure drop near the apertures A and A'. The target chamber has a full-width-at-half-maximum of $Z_{FWHM} = 330 \pm 8$ mm and a mean width of $Z_{MW} = 376 \pm 8$ mm. Because the target gas streams out the aperture, the effective target length is about 30% longer than its physical configuration. We use 376 ± 8 mm as the effective length of the target chamber to calculate the target thickness.

3.3.2 DRAGON Target System

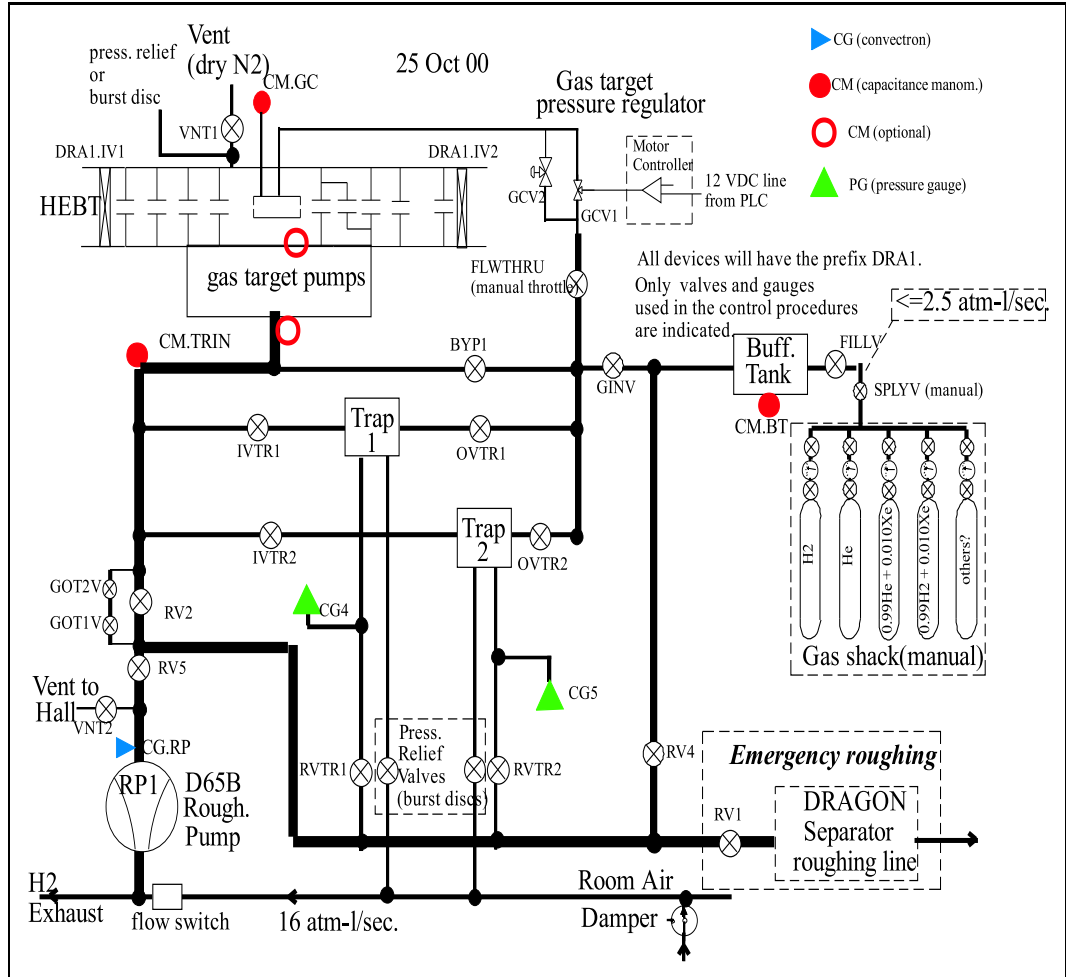


Figure 3.7: DRAGON's differentially-pumped windowless gas target system.

Differentially-Pumped Gas Target and the Recirculation System

Given the long-time run required by DRAGON experiments, the gas target is designed to run in the recirculation mode from the consideration of the cost and gas-handling aspects of flow-through mode. Figure 3.7 shows a schematic view of the system. To handle the contamination problem of recirculation, a cold trap cleaner containing zeolite at liquid N₂

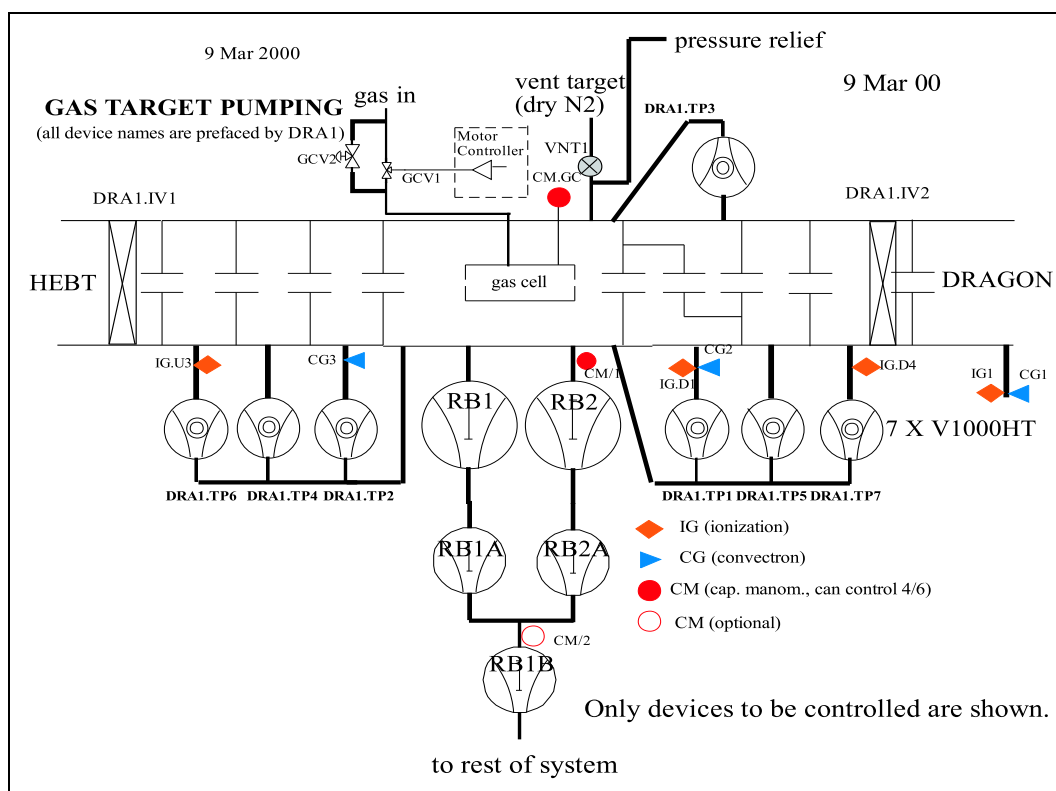


Figure 3.8: DRAGON's gas target with the recirculation and cold trap of the gas handling system.

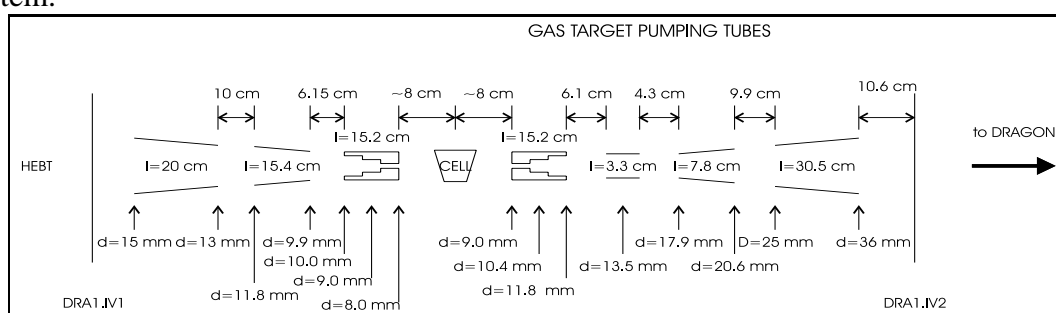


Figure 3.9: Detailed dimension of pumping tubes in DRAGON's differentially-pumped windowless system.

(LN) temperature is built initially. A second trap might be built if necessary.

DRAGON's extended gas target system, shown in Figure 3.8, consists of a central inner cell with its pumping stage, and in addition, three stages of differential pumping upstream and four downstream.

The central stage of the pumping system is functioned with five Roots blowers. Two large blowers (WSU2001), which displace a nominal $2000 \text{ m}^3/\text{h}$, are each backed by a $500 \text{ m}^3/\text{h}$ Roots blower (WSU501). The final boost to 50 Torr trap in the recirculation system is made by feeding the two smaller blowers to a third one of the same type. This system can pump the pressure in the target box (out of the cell) down to around 0.35 Torr with 4.5 Torr inside the gas cell.

The subsequent stages of differential pumping utilize turbomolecular pumps (V1000HT) for pumping down to about 10^{-6} Torr. This was only achieved for hydrogen when the trapezoidal shape was introduced as will be described. The dimension of the pumping tubes connecting the target and the consecutive pumping stages are shown in Figure 3.9. This design of pumping tubes limit the gas flow out from the target, and also limits the beam incident on the target to a half-cone angle divergence of 0.566° , and an half-cone opening to 0.795° .

A needle valve controls the loading of gas into the cell, and the pressure in the target cell is measured by the capacitance manometer with an uncertainty less than $\pm 2\%$. The offset of the gauge varies with temperature, so it is checked by normalizing the elastic monitor (particle detector) data to pressure.

At the time of our run, the trap cleaner has not been commissioned. One gas sample has been analyzed for impurities and found there is about 5% N_2 accumulated about four hours after the loading of gas. So during our measurement, gas in the recirculation system is refreshed every four hours to minimize the contamination problem. Such a procedure is not needed with the present trap operation.

Target Box

The shapes of the entrance and exit windows of the target inner cell was inclined (at an angle of 20°), as shown in Figure 3.10, to minimize the effects of jetting apparently at the nozzle of the inner chamber, but only when using hydrogen gas. The vacuum levels at the exit of the target system improved up a factor of ten when this shape change was introduced, and the design criteria of $< 1.2 \times 10^{-6}$ Torr was met.

The center target cell is of length 11.05 cm and can be operated at the maximum pressure

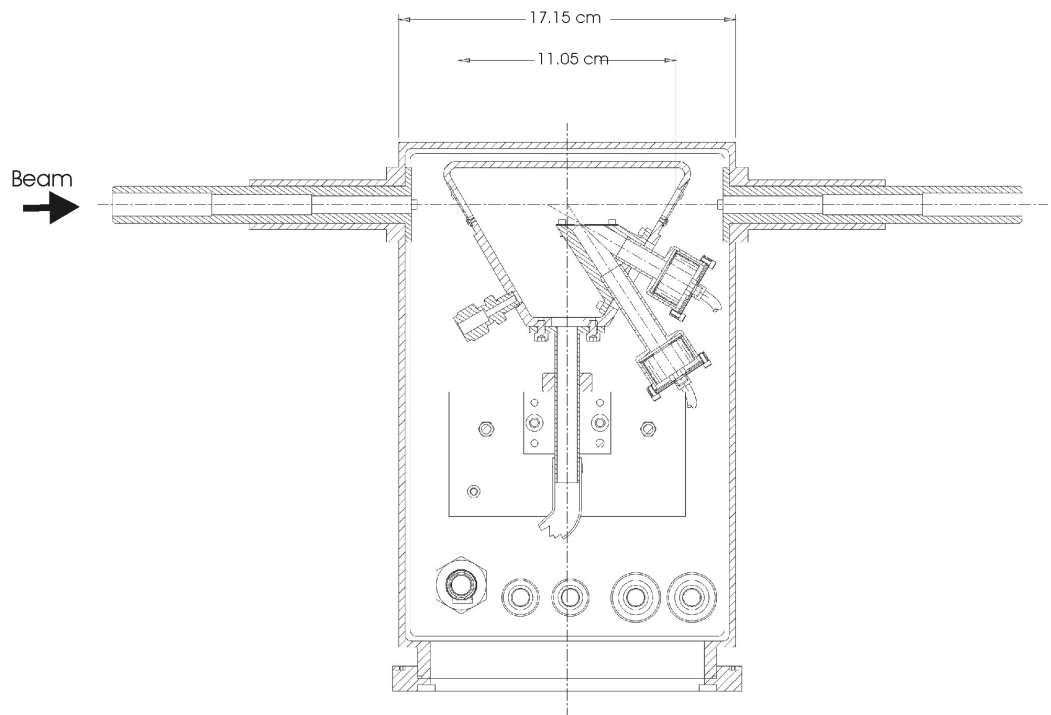


Figure 3.10: Schematic of DRAGON trapezoid target cell placed in a rectangular box. Two elastic monitors are installed at $\theta_{lab} = 30^\circ$ and 57° , respectively.

6 Torr. The gas flow out of the cell is limited by an entrance and exit circular aperture of diameter 6 mm and 8 mm, respectively. Tube on the bottom connects to the initial pumping stage, which is composed of five Root blowers as described.

The most reliable monitor of beam intensity is expected to be elastic scattering of beam particle from the target atoms. So two elastic monitors (solid state silicon detectors), looking at the center of the gas, are installed in the gas cell at $\theta_{lab} = 30^\circ$ and 57° , respectively. They have a common ellipse collimator and another individual circular one right in front of the detector. This defines the effective length seen by the detectors to be 1.298 ± 0.001 cm and 0.709 ± 0.001 cm, which corresponds to a range of scattering angle $23.22^\circ \sim 36.15^\circ$ and $51.85^\circ \sim 61.78^\circ$, respectively. In addition, an alpha source is mounted permanently in a position that is observed by the 57° detector.

Target Density Profile

The target density profile is an important operational parameter of the target cell. Using the energy independent cross section interval of the $H(^{15}N, \alpha\gamma)^{12}C$ reaction around 1.45 MeV/u [41], we measured the density profile of the windowless gas target.

BGO ($Bi_4Ge_3O_{12}$) gamma detectors have been set up on both sides of the target as shown in Figure 3.11 and 3.12. Each hexagonal BGO detector has a side length of 33.4 cm. On one side of the target, a two-row array built up by thirteen BGO detectors covered a length of 20.4 cm along the beam axis. It provided a position sensitivity, which can be used to place the resonance in the center of the target in later experiments. On the other side, a single BGO detector placed on a sleigh is gated by lead. The detector looks at an effective length of 1.65 ± 0.1 cm, determined by the 0.95 cm wide slit located 3 cm away from the center of the target. It can only be moved along the target from -10 cm to 10 cm, referring to the center of the target because of the structural hindrances.

The resulting yield versus detector position is plotted in Figure 3.13. It shows a constant pressure plateau at the center of the target chamber and a relatively sharp drop near the aperture. The full-width-at-half-maximum is determined to be of $Z_{FWHM} = 10.82 \pm 0.64$ cm.

The yield curve also indicated that the pressure outside the cell drops to 34% of the inner cell pressure, which corresponds 1.5 Torr outside the cell when the cell pressure reads 4.5 Torr. The fact that this does not agree with the pressured measured to 0.35 Torr by a capacitance vacuum gauge at the bottom of the target box can be explained as the obstacles (i.e., elastic scattering monitors, cables etc.) in the box limit the effective pumping to the

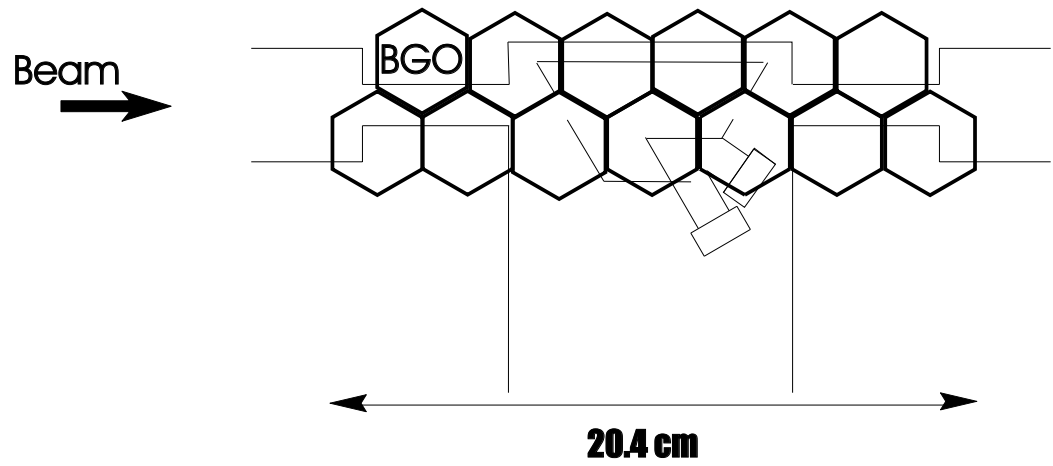


Figure 3.11: Side view of two-row BGO array along the gas target.

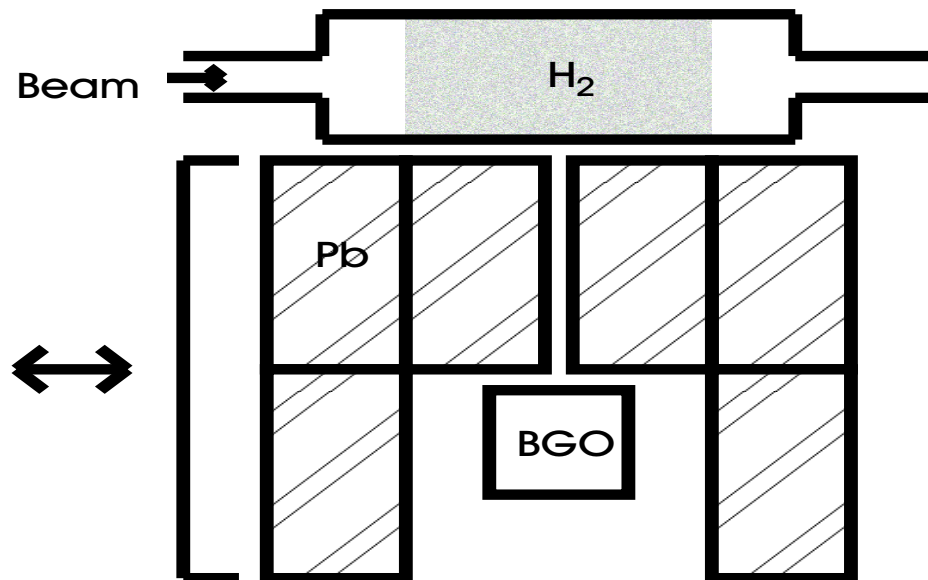


Figure 3.12: Setting of the single BGO detector facing the target with slit opening 0.95cm.

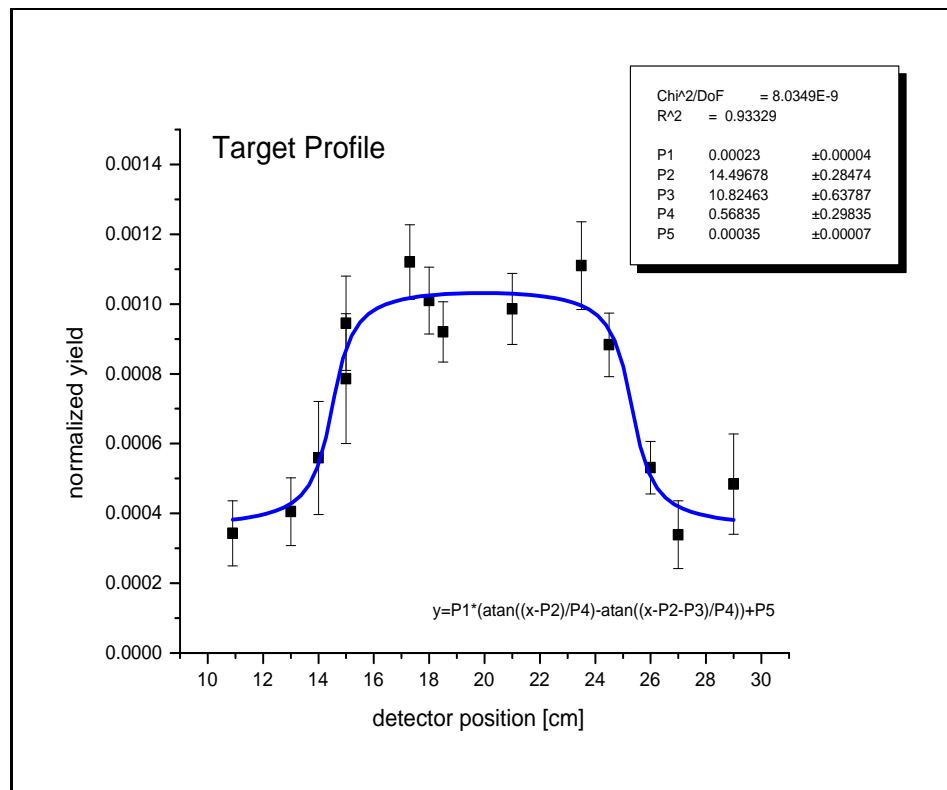


Figure 3.13: Normalized yield versus the detector position along the beam axis with position 20cm corresponding to the center of the target.

upper part of the box.

The biggest systematic error in the final determination of the charge changing cross section arises from the uncertain effective length of the gas target. Due to the finite pumping speed, target gas streams out through apertures and tubes. The net result of this is an increase of the effective length of the gas cell.

Because of the structural constrictions, a complete pressure profile measurement along the beam axis, namely, extending from the target cell to the entrance and exit sections of pumping tubes, could not be conducted for DRAGON target. To estimate the effective target length, the rate of gas flow through a tube V_m is calculated from the Poiseuille law as [42]

$$V_m \propto \frac{a^4}{l} (P_2^2 - P_1^2) \quad (3.2)$$

where a is the radius of tube, l the length, and P_1, P_2 the pressure at the two ends of the tube. The pressure P_{tube} in the 15.2 cm tubes connecting the target box (Figure 3.9) to the differential pumping stages is calculated as a function of the radius a and distance z , assuming a constant flow through the tube. The pressure at the inner and outer end of these two tubes are taken to be 34% of the cell pressure and 0 Torr, respectively. Also assume a constant pressure (34% of the inner cell pressure) from the cell aperture to the pumping tube, the effective length of the gas target can be expressed as

$$Z_{eff} = Z_{FWHM} + \left(\frac{\int P_{tube}(z) dz}{P_0} \right)_{downstream} + \left(\frac{\int P_{tube}(z) dz}{P_0} \right)_{upstream} + 2 \times \frac{34\% P_0 \times 2.5}{P_0} \quad (3.3)$$

where 2.5 cm is the distance from the cell aperture to the tube aperture. This gives an effective length of 18.5 cm for our gas target.

3.4 Data Analysis and Uncertainties

Theoretically, the measured beam intensities of different charge states should sum up to the total beam intensity measured by FC1. However, experimental data normally deviate from this because of the instability of the beam and measurements on individual charge state are done sequentially.

Therefore, to calculate the charge state fraction, we first converted the measured charge intensity to particle intensity and normalized it to the counting rate of elastic monitor C (or to the total beam intensity)

$$n_q = \frac{I_q}{qC} \quad (3.4)$$

Then the charge state fraction, F_q can be calculated as

$$F_q = \frac{n_q}{\sum n_q} \quad (3.5)$$

Two examples of these calculations are illustrated in Appendix B. One is for ^{16}O beam of 0.138 MeV/u and incident charge state 2+ passing through hydrogen gas target, which was measured at Naples, and the other for ^{16}O beam of 0.800 MeV/u and incident charge state 4+ passing through hydrogen gas target, which was measured at DRAGON.

The uncertainty Δn_q in n_q can be evaluated as

$$\Delta n_q = \sqrt{\left(\frac{\partial n_q}{\partial I_q}\right)^2 (\Delta I_q)^2 + \left(\frac{\partial n_q}{\partial C}\right)^2 (\Delta C)^2} \quad (3.6)$$

$$= n_q \sqrt{\left(\frac{\Delta I_q}{I_q}\right)^2 + \left(\frac{\Delta C}{C}\right)^2} \quad (3.7)$$

Then the uncertainty in the charge state fraction is estimated to be

$$\Delta F_q = \sqrt{\left(\frac{\partial F_q}{\partial n_q}\right)^2 (\Delta n_q)^2 + \sum_{q' \neq q} \left(\frac{\partial F_q}{\partial n_{q'}}\right)^2 (\Delta n_{q'})^2} \quad (3.8)$$

Assume the same $\Delta n_q/n_q$ for different charge states, the above equation can be simplified to

$$\frac{\Delta F_q}{F_q} = \frac{\Delta n_q}{n_q} \sqrt{(1 - 2F_q) + \sum_q F_q^2} \quad (3.9)$$

All the experimental and data analysis uncertainties are listed in Table 3.1.

3.5 Results

As mentioned above, we measured the non-equilibrium and equilibrium charge state distribution of low energy (0.138 - 0.875 MeV/u) ^{15}N , ^{16}O , ^{23}Na , and ^{24}Mg beams passing through windowless hydrogen and helium gas target. The combinations of projectile and target are tabulated in Table 3.2, together with the equilibrium charge state distributions. Uncertainties quoted in Table 3.2 are calculated as discussed in Section 3.4.

In cases where the distribution from non-equilibrium to equilibrium is measured, the experimental data are shown as solid symbols on the growth curve graphs listed in Appendix

Table 3.1: Experimental and Data Analysis Uncertainties

<i>Experimental Uncertainties - Naples</i>		
<i>Source</i>	<i>Equipment</i>	<i>Uncertainty</i>
Pressure	Baratron	<4%
Effective target Length	Gas cell	~3%
Beam Charge Intensity	Faraday Cup	2% ~ 10%
Charge State Analyzing	Magnet + People	2% ~ 5%
<i>Experimental Uncertainties - DRAGON</i>		
<i>Source</i>	<i>Equipment</i>	<i>Uncertainty</i>
Pressure	Manometer	<2%
Effective target Length	Gas cell	~ 10%
Beam Charge Intensity	Faraday Cup + Current Integrator	<3%
Charge State Analyzing	Magnet +Reference File	<1%
Gas Impurity	Target Sysytem	<5%
<i>Analysis Uncertainties</i>		
	Naples	DRAGON
$F(q) < 1\%$	10 ~ 20%	~10%
$1\% < F(q) < 10\%$	6 ~ 10%	~5%
$F(q) > 10\%$	~4%	~3%

A. Solids lines on the graphs come from calculations, which will be discussed in the next chapter.

Table 3.2: Experimental Equilibrium Charge State Distribution, where * and † refer to data from Naples and DRAGON measurements, respectively.

	$E(MeV/u)$	q_{in}	1+	2+	3+	4+	5+	6+	7+	8+	9+	10+
$^{15}N + H_2^{\dagger}$	0.435	4+				3.70 ± 0.22	34.32 ± 0.90	57.57 ± 0.95	4.41 ± 0.26			
$^{16}O + H_2^*$	0.138	2+,3+,4+	10.46 ± 0.56	43.30 ± 1.21	38.99 ± 1.18	7.01 ± 0.46	0.33 ± 0.05					
$^{16}O + H_2^*$	0.200	3+,4+,5+	17.59 ± 0.71	48.78 ± 1.21	48.78 ± 1.21	30.17 ± 1.05	3.41 ± 0.27	0.05 ± 0.01				
$^{16}O + H_2^*$	0.325	3+,5+	1.10 ± 0.09	13.41 ± 0.56	47.59 ± 1.22	34.19 ± 1.13	3.71 ± 0.29					
$^{16}O + H_2^{\dagger}$	0.325	4+			7.37 ± 0.41	50.07 ± 0.94	37.51 ± 0.91	5.05 ± 0.35				
$^{16}O + H_2^*$	0.500	4+			0.50 ± 0.06	10.00 ± 0.44	44.50 ± 1.27	43.50 ± 1.26	1.50 ± 0.09			
$^{16}O + H_2^{\dagger}$	0.500	4+			0.35 ± 0.04	9.89 ± 0.54	41.88 ± 0.95	46.77 ± 0.96	1.11 ± 0.07			
$^{16}O + H_2^*$	0.588	3+			0.11 ± 0.02	3.50 ± 0.29	32.23 ± 1.17	59.85 ± 1.24	4.31 ± 0.30			
$^{16}O + H_2^{\dagger}$	0.800	4+				0.36 ± 0.04	8.93 ± 0.51	65.81 ± 0.84	23.78 ± 0.72	1.12 ± 0.14		
$^{23}Na + H_2^*$	0.200	3+,5+,6+	7.39 ± 0.49	42.51 ± 1.21	40.78 ± 1.20	8.72 ± 0.57	0.60 ± 0.07					
$^{23}Na + H_2^*$	0.374	4+,6+			1.01 ± 0.11	13.25 ± 0.54	40.90 ± 1.15	34.69 ± 1.09	9.44 ± 0.50	0.71 ± 0.08		
$^{23}Na + H_2^*$	0.478	4+,7+			0.10 ± 0.02	2.18 ± 0.15	16.74 ± 0.66	40.18 ± 1.14	32.81 ± 1.06	7.50 ± 0.48	0.49 ± 0.08	
$^{24}Mg + H_2^{\dagger}$	0.200	6+			36.17 ± 0.88	48.72 ± 0.94	14.03 ± 0.44	1.07 ± 0.06	0.01 ± 0.001			
$^{24}Mg + H_2^{\dagger}$	0.500	6+				0.66 ± 0.08	8.29 ± 0.40	30.45 ± 0.76	40.81 ± 0.85	17.66 ± 0.51	2.13 ± 0.12	
$^{24}Mg + H_2^{\dagger}$	0.800	6+						1.40 ± 0.08	10.51 ± 0.33	41.64 ± 0.89	37.78 ± 0.86	8.67 ± 0.42
$^{16}O + H_2^*$	0.138	2+,3+,4+	20.78 ± 0.79	44.96 ± 1.18	27.69 ± 0.97	6.31 ± 0.35	0.26 ± 0.04					
$^{16}O + H_2^*$	0.200	3+,4+,5+	0.02 ± 0.003	33.04 ± 1.10	46.31 ± 1.22	18.64 ± 0.74	1.92 ± 0.15	0.07 ± 0.01				
$^{16}O + H_2^*$	0.325	3+,5+			7.90 ± 0.43	34.48 ± 1.10	42.28 ± 1.17	14.61 ± 0.59	0.73 ± 0.08			
$^{16}O + H_2^*$	0.371	3+			4.82 ± 0.27	25.56 ± 0.93	47.21 ± 1.47	20.31 ± 0.78	2.10 ± 0.12			
$^{16}O + H_2^*$	0.588	3+			3.90 ± 0.22	24.45 ± 0.90	47.52 ± 1.19	23.31 ± 0.87	0.82 ± 0.09			
$^{16}O + H_2^*$	0.750	6+				9.00 ± 0.59	37.38 ± 1.19	48.11 ± 1.25	5.51 ± 0.31			
$^{16}O + H_2^*$	0.875	5+					29.88 ± 1.11	59.44 ± 1.22	10.68 ± 0.59			

Chapter 4

Discussion

4.1 Critical Target Thickness

For several projectile and target combinations, we measured the non-equilibrium and equilibrium charge state distribution with different incident charge states. It is obvious from the growth curves of charge state distribution (Appendix A) that the non-equilibrium distribution is a function of incident charge state, while equilibrium distribution is independent of the incident charge state. This agrees with theoretical prediction.

In case of self-supporting solid foil target, the thickness is usually large enough for charge state distribution of beam passing through it to reach equilibrium. For gas target, however, this is not the case. At low target pressure, the beam passing through it cannot have enough collisions with the target atoms for the charge state distribution to establish equilibrium. Practically, it is important to understand how fast the equilibrium charge state distribution is reached. We define the critical thickness as the lowest target thickness necessary to establish the equilibrium distribution. A thorough review of the literature seems to indicate that there is not a theory available to predict the relation of critical thickness with projectile energy, species and the target species.

In Table 4.1, we presented critical thickness estimated from the growth curve of our measurement, if available. The transition from non-equilibrium to equilibrium is a gradual process, so it is hard to determine exactly the lowest pressure where all the charge state fractions start to be constant from the growth curve. The critical thickness and the corresponding pressure listed are where the fractions of all charge states are within $\pm 5\%$ of its equilibrium values as listed in Table 3.2. The critical thickness is calculated from the critical pressure using equation (2.3), and to make the data more comparable, pressure from Naples

Table 4.1: Critical target thickness x_c and the corresponding pressure at Naples and DRAGON gas target, with * and † refer to data from Naples and DRAGON measurements, respectively.

	$E(\text{MeV/u})$	q_{in}	$x_c(10^{16}\text{atoms/cm}^2)$	P_{NAPLES} (mbar)	P_{DRAGON} (Torr)
$^{15}\text{N} + H_2^\dagger$	0.435	4+	73.1		0.610
$^{16}\text{O} + H_2^*$	0.138	2+	3.54	0.038	0.059
		3+	8.23	0.044	0.068
		4+	10.2	0.055	0.085
$^{16}\text{O} + H_2^*$	0.200	3+	11.6	0.063	0.097
		4+	17.0	0.092	0.142
		5+	19.7	0.106	0.164
$^{16}\text{O} + H_2^*$	0.325	3+	50.7	0.274	0.423
		5+	44.6	0.241	0.372
$^{16}\text{O} + H_2^\dagger$	0.325	4+	16.1		0.134
$^{16}\text{O} + H_2^\dagger$	0.500	4+	116.2		0.969
$^{16}\text{O} + H_2^\dagger$	0.800	4+	508.5		4.242
$^{23}\text{Na} + H_2^*$	0.200	3+	14.6	0.079	0.122
		5+	18.3	0.099	0.153
		6+	20.4	0.110	0.170
$^{23}\text{Na} + H_2^*$	0.374	4+	85.4	0.461	0.712
		6+	63.8	0.341	0.527
$^{23}\text{Na} + H_2^*$	0.478	4+	140.1	0.757	1.169
		7+	120.6	0.651	1.006
$^{24}\text{Mg} + H_2^\dagger$	0.200	6+	19.8		0.165
$^{24}\text{Mg} + H_2^\dagger$	0.500	6+	107.5		0.897
$^{24}\text{Mg} + H_2^\dagger$	0.800	6+	277.2		2.312
$^{16}\text{O} + He^*$	0.138	2+	6.47	0.070	0.108
		4+	7.49	0.081	0.125
$^{16}\text{O} + He^*$	0.200	3+	3.60	0.039	0.060
		4+	6.29	0.068	0.105
		5+	7.97	0.086	0.133
$^{16}\text{O} + He^*$	0.325	3+	8.69	0.094	0.145
		5+	11.7	0.127	0.196

experimental data have been converted to pressure corresponding to the same thickness at DRAGON's target as

$$P_{DRAGON}(Torr) = \frac{L_{Naples}}{L_{DRAGON}} \times P_{Naples}(mbar) \times 0.76(Torr/mbar) \quad (4.1)$$

where L_{Naples} and L_{DRAGON} are the effective lengths of the targets, determined to be 37.6 cm and 18.5 cm, respectively. The error on critical thickness is about $\pm 10\%$.

From these limited data, it is noticed that the equilibrium distribution is generally reached at low target pressure. In addition, the critical thickness increases as the energy of the projectile increases, because, as will be discussed in section 4 of this chapter, the corresponding charge changing cross section decreases and more charge changing processes are required to reach equilibrium charge state distribution. Comparing the critical thickness x_c of different projectiles with same velocity passing through hydrogen target, we noticed that with the increase of the projectile atomic number, x_c increases slightly. It is also noticed from the growth curves for projectiles of same species and velocity but different incident charge state, equilibrium is reached relatively easier when the incident charge state is closer to the dominant state at equilibrium.

4.2 Equilibrium Distribution

4.2.1 Reproducibility

As stated before, the equilibrium charge state distribution is a function of the beam energy and the target species, and independent of the target thickness once equilibrium is reached, if the energy loss within the target is neglected.

Reproducibility of the equilibrium distribution is checked by comparing Naples and DRAGON's measurements for oxygen beam of 0.325 MeV/u and 0.500 MeV/u passing through hydrogen. We noticed the agreement between two measurements at 0.500 MeV/u, but also the divergence at 0.325 MeV/u (Figure 4.1). For the latter, the major difference is in F_3 , which is 13.41% from Naples measurement and 7.49% from DRAGON measurement. We considered the gas impurity as the major source of this divergence. As stated in Section 3.3.2, without the commission of the trap, the DRAGON target system, running in the recirculation mode, accumulated contamination from the backstreaming of the pumps. And unfortunately, the measurement of 0.325 MeV/u oxygen through hydrogen happened to be done after long time run and right before refreshing the target gas. A more quantitative

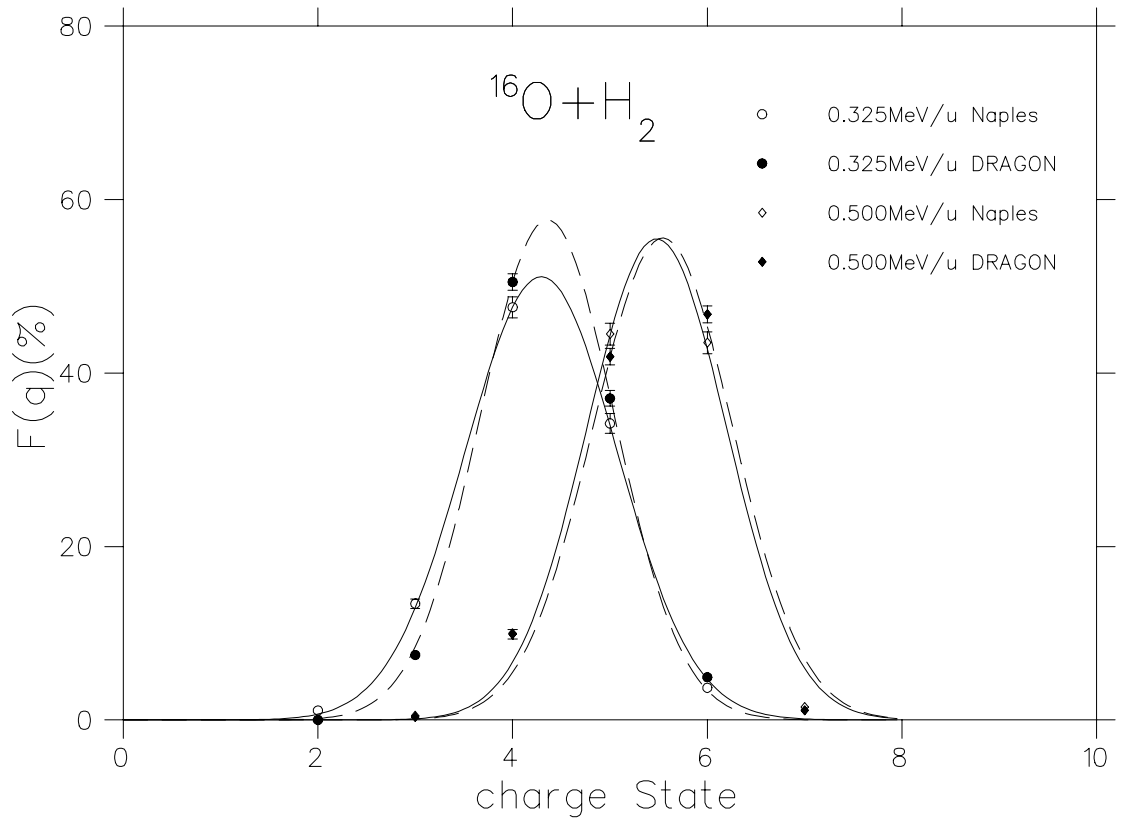


Figure 4.1: Comparison of equilibrium charge state distribution between Naples and DRAGON's measurements for ^{16}O beam passing through hydrogen gas target, with symbols representing the experimental data and line for Gaussian distribution.

explanation is not available because of the lack of relevant charge changing cross section data.

It has also been determined that the charge changing cross sections fitted from the Naples data fit into the general trend as will be shown in section 4.3. So from this point on, the DRAGON's data for 0.325 MeV/u oxygen passing through hydrogen is excluded from further discussion.

4.2.2 Energy loss

Projectile energy loss, at energies below nuclear excitation levels, is known to be by means of inelastic nuclear and electronic encounters, discrete electronic excitation with subsequent radiation, and electron capture and loss processes. Although the relative importance of a particular mechanism depends on the velocity of the particle in the medium under consideration, electron capture and loss are known to be important energy transfer mechanism at projectile velocities exceeding or of the order the electron orbital velocities associated with the projectile.

In our measurement, energy loss of beam is estimated as discussed in section 3.1 and 3.2, and tabulated in Table 4.2. Data from Naples measurements at 1 mbar have been converted to the corresponding energy loss of the same projectile and target combination passing through DRAGON target at 1 Torr as

$$E_{loss(DRAGON@1Torr)}(keV/u) = E_{loss(Naples@1mbar)}(keV/u) \times \frac{18.5(cm)}{37.6(cm)} \times \frac{1}{0.76(Torr/mbar)} \quad (4.2)$$

Also listed is the energy loss from SRIM [39] calculation for DRAGON target at 1 Torr.

Obviously, the energy loss of low energy beam within a dilute gas target is small. And we found that the change in F_q of the most probable equilibrium charge state caused by this energy difference is of the order of the uncertainty, which could be neglected. As an example, for 0.800 MeV/u ^{16}O passing through hydrogen gas target, energy loss is measured to be 0.030 MeV/u at 4.5 Torr. We found a difference of 3.0% in F_6 , the most probable charge state at equilibrium, between beam of 0.800 MeV/u and 0.770 MeV/u using the semi-empirical formula derived, which will be discussed in section 4.2.3.

4.2.3 Gaussian Distribution

Equilibrium charge state distributions obtained show a remarkable symmetry and can be well described by a Gaussian distribution as showed in Figure 4.2, 4.3, 4.4, 4.5. The average

Table 4.2: Energy loss measurements versus SRIM calculation, with * and † refer to data from Naples and DRAGON measurements, respectively. Naples data have also been converted to corresponding energy loss through DRAGON target at 1 Torr (listed in the ' $E_{loss}1Torr(DRAGON)$ ' column with DRAGON measurement data). All energies are in unit of keV/u.

	E	q_{in}	$E_{loss}@1mbar(Naples)$	$E_{loss}@1Torr(DRAGON)$	$SRIM@1Torr(DRAGON)$
$^{16}O + H_2^*$	0.138	2+	6.3	4.1	4.2
		3+	4.8	3.1	
		4+	6.3	4.1	
$^{16}O + H_2^*$	0.200	3+	4.8	3.1	4.6
		4+	4.6	3.0	
		5+	5.0	3.2	
$^{16}O + H_2^*$	0.325	3+	8.3	5.4	4.4
		5+	8.5	5.5	
$^{16}O + H_2^\dagger$	0.500	4+		3.5	4.0
$^{16}O + H_2^\dagger$	0.800	4+		6.6	3.5
$^{23}Na + H_2^*$	0.200	3+	5.5	3.5	2.9
		5+	3.9	2.5	
		6+	6.6	4.3	
$^{23}Na + H_2^*$	0.374	6+	4.8	3.1	4.3
$^{23}Na + H_2^*$	0.478	4+	8.7	5.6	4.2
		7+	6.1	3.9	
$^{24}Mg + H_2^\dagger$	0.200	6+		2.7	4.3
$^{16}O + He^*$	0.138	2+	2.8	1.8	2.8
		4+	2.9	1.9	
$^{16}O + He^*$	0.200	3+	2.3	1.5	3.2
		4+	3.4	2.2	
		5+	3.4	2.2	
$^{16}O + He^*$	0.325	3+	3.4	2.2	3.5
		5+	2.5	1.6	

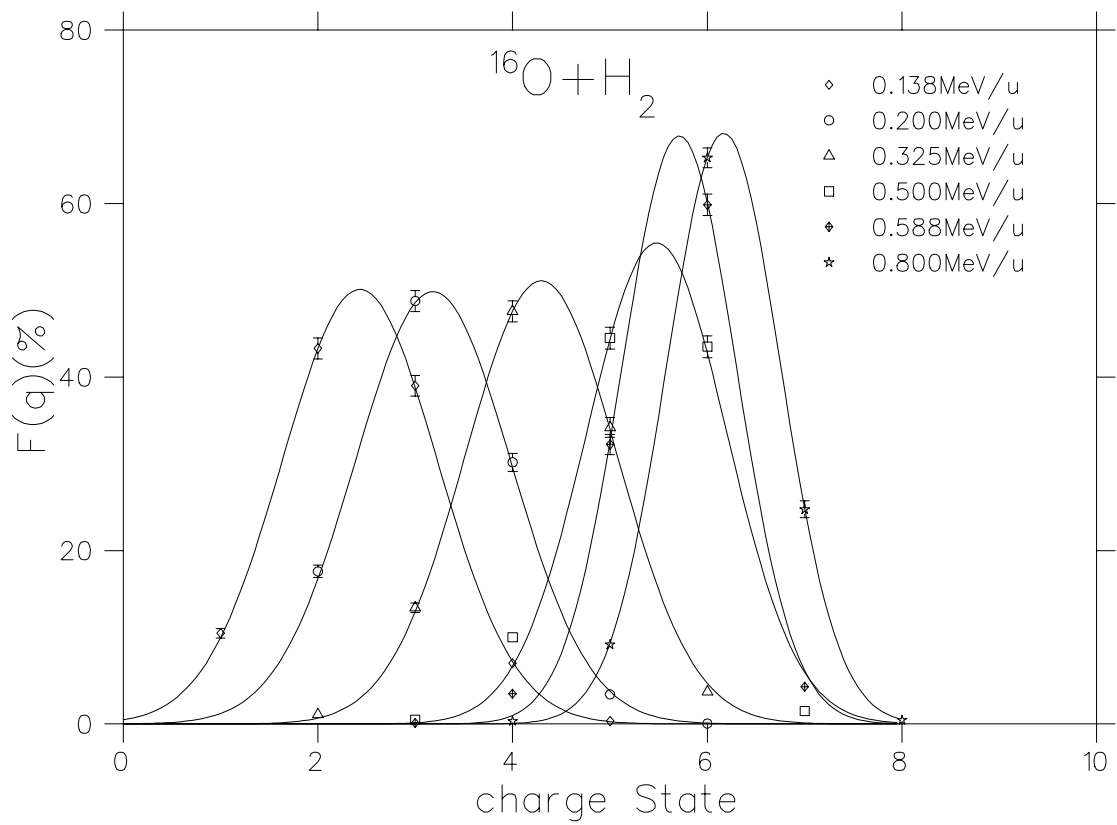


Figure 4.2: Equilibrium charge state distribution of ^{16}O beam passing through hydrogen gas target, with symbols representing the experimental data and line for Gaussian distribution.

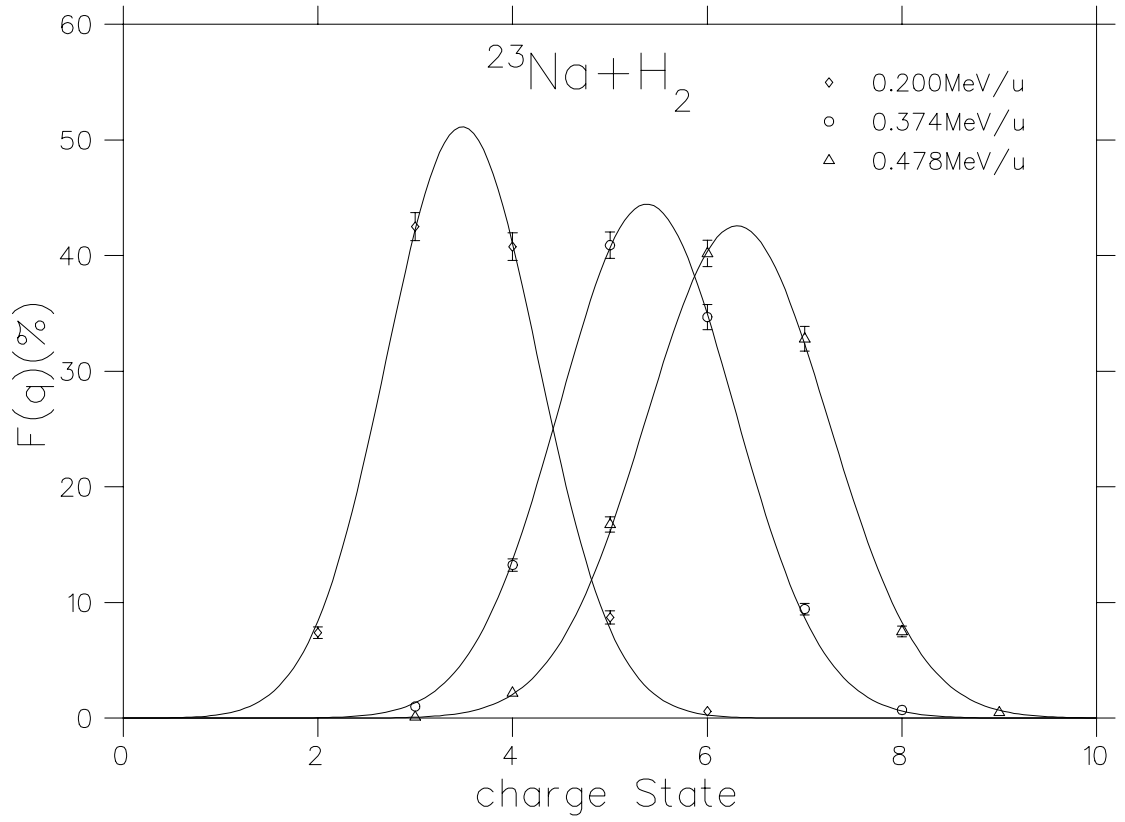


Figure 4.3: Equilibrium charge state distribution of ^{23}Na beam passing through hydrogen gas target, with symbols representing the experimental data and line for Gaussian distribution.

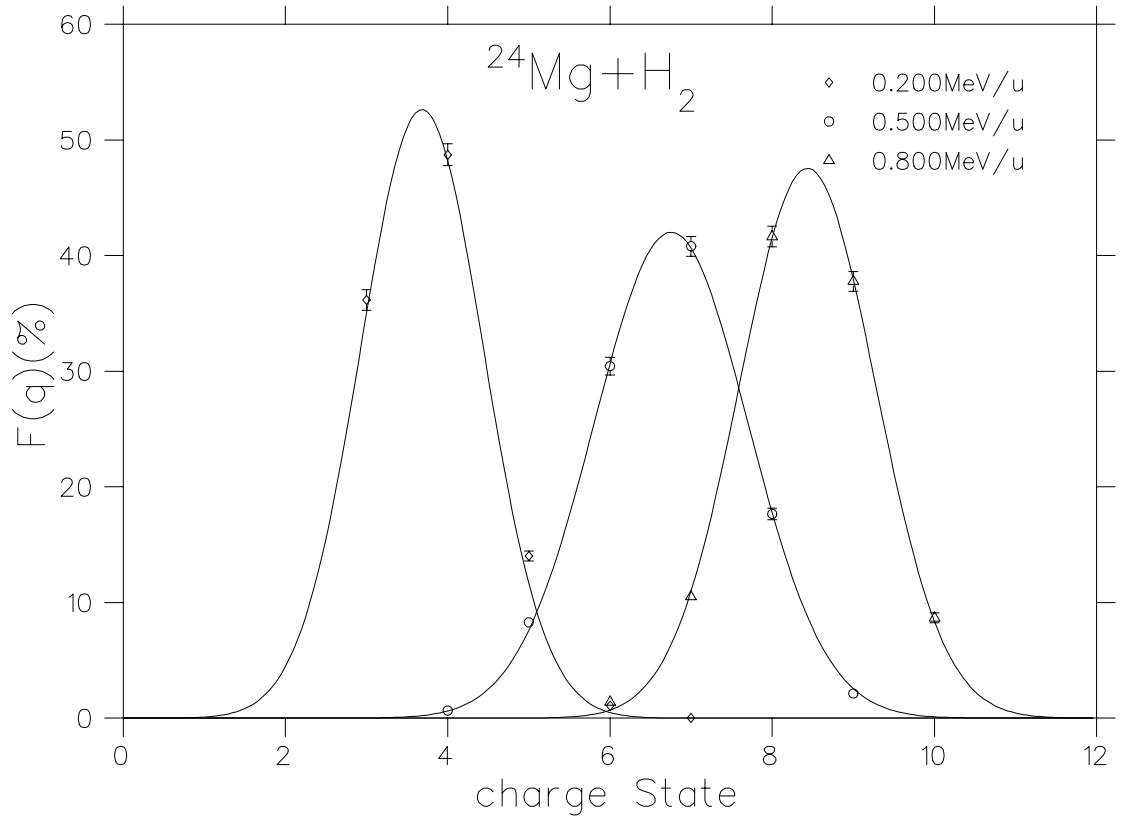


Figure 4.4: Equilibrium charge state distribution of ^{24}Mg beam passing through hydrogen gas target, with symbols representing the experimental data and line for Gaussian distribution.

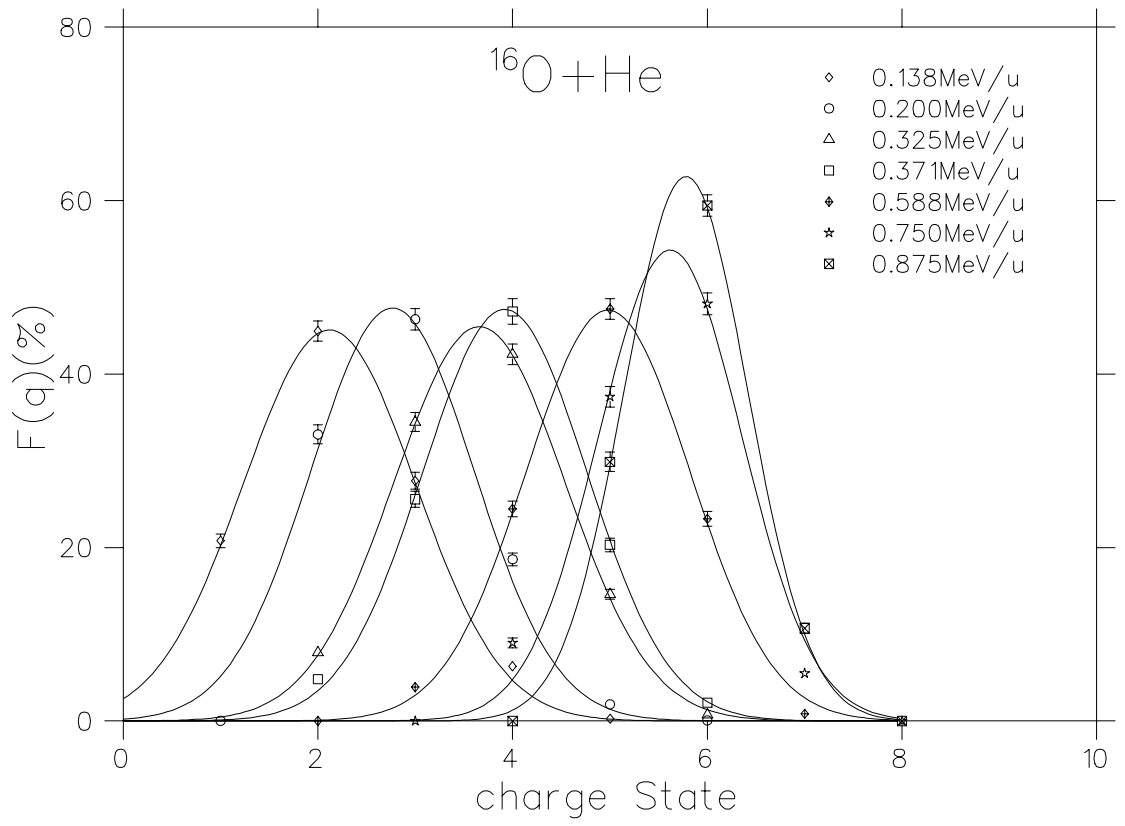


Figure 4.5: Equilibrium charge state distribution of ^{16}O beam passing through helium gas target, with symbols representing the experimental data and line for Gaussian distribution.

Table 4.3: Experimental \bar{q} , d, and s versus \bar{q} and d from Gaussian fit, with * and † refer to data from Naples and DRAGON measurements, respectively.

	$E(\text{MeV}/u)$	<i>Experimental Data</i>			<i>Gaussian Distribution</i>	
		\bar{q}	d	s	q_{max}	d
$^{15}\text{N} + H_2^\dagger$	0.435	5.63 ± 0.10	0.629 ± 0.007	-4.00E-5	5.69 ± 0.01	0.603 ± 0.011
$^{16}\text{O} + H_2^*$	0.138	2.44 ± 0.05	0.784 ± 0.010	9.52E-5	2.43 ± 0.01	0.796 ± 0.004
$^{16}\text{O} + H_2^*$	0.200	3.20 ± 0.06	0.762 ± 0.010	1.45E-5	3.18 ± 0.01	0.800 ± 0.009
$^{16}\text{O} + H_2^*$	0.325	4.26 ± 0.08	0.775 ± 0.009	-1.49E-5	4.29 ± 0.01	0.781 ± 0.006
$^{16}\text{O} + H_2^*$	0.500	5.36 ± 0.10	0.699 ± 0.008	-4.40E-5	5.48 ± 0.02	0.719 ± 0.029
$^{16}\text{O} + H_2^\dagger$	0.500	5.38 ± 0.08	0.691 ± 0.008	-5.37E-5	5.54 ± 0.04	0.718 ± 0.046
$^{16}\text{O} + H_2^*$	0.588	5.65 ± 0.10	0.625 ± 0.009	-5.38E-5	5.71 ± 0.02	0.588 ± 0.017
$^{16}\text{O} + H_2^\dagger$	0.800	6.16 ± 0.08	0.600 ± 0.008	1.32E-5	6.17 ± 0.01	0.586 ± 0.001
$^{23}\text{Na} + H_2^*$	0.200	3.53 ± 0.07	0.779 ± 0.011	1.87E-5	3.48 ± 0.01	0.780 ± 0.011
$^{23}\text{Na} + H_2^*$	0.374	5.40 ± 0.10	0.893 ± 0.011	6.55E-6	5.38 ± 0.01	0.897 ± 0.007
$^{23}\text{Na} + H_2^*$	0.478	6.28 ± 0.11	0.926 ± 0.012	-6.01E-6	6.30 ± 0.01	0.937 ± 0.008
$^{24}\text{Mg} + H_2^\dagger$	0.200	3.80 ± 0.05	0.711 ± 0.006	4.95E-5	3.68 ± 0.02	0.758 ± 0.021
$^{24}\text{Mg} + H_2^\dagger$	0.500	6.73 ± 0.09	0.940 ± 0.009	-7.30E-6	6.75 ± 0.01	0.949 ± 0.006
$^{24}\text{Mg} + H_2^\dagger$	0.800	8.42 ± 0.12	0.843 ± 0.008	-1.84E-5	8.44 ± 0.01	0.839 ± 0.005
$^{16}\text{O} + He^*$	0.138	2.20 ± 0.04	0.848 ± 0.010	3.24E-5	2.12 ± 0.02	0.885 ± 0.011
$^{16}\text{O} + He^*$	0.200	2.90 ± 0.05	0.768 ± 0.009	4.68E-5	2.77 ± 0.03	0.838 ± 0.024
$^{16}\text{O} + He^*$	0.325	3.66 ± 0.07	0.848 ± 0.010	9.37E-7	3.66 ± 0.01	0.877 ± 0.005
$^{16}\text{O} + He^*$	0.371	3.89 ± 0.08	0.851 ± 0.010	-5.95E-6	3.92 ± 0.01	0.841 ± 0.008
$^{16}\text{O} + He^*$	0.588	4.93 ± 0.09	0.813 ± 0.010	-2.10E-5	4.98 ± 0.01	0.842 ± 0.008
$^{16}\text{O} + He^*$	0.750	5.50 ± 0.10	0.735 ± 0.011	-2.68E-5	5.62 ± 0.03	0.735 ± 0.034
$^{16}\text{O} + He^*$	0.875	5.81 ± 0.10	0.607 ± 0.009	1.23E-5	5.78 ± 0.01	0.635 ± 0.005

equilibrium charge state \bar{q} and distribution width d calculated from experimental data are tabulated together with those fitted from Gaussian distribution in Table 4.3. They agree within 1% for most cases. Some large discrepancy came from experimental error, e.g., for ^{16}O beam of 0.138 MeV/u through helium target, we have not been able to measure the fraction of neutral particles. Also, during DRAGON's measurement of 0.200 MeV/u ^{24}Mg through hydrogen, charge state 2+ was missed because the required large magnetic field is out of the design limit of DRAGON's magnet dipole MD1. And some originated from the shell structure effect, e.g., the fractions of 4+ are higher than that expected by the symmetric Gaussian distribution for ^{16}O beam of 0.500 MeV/u and 0.588 MeV/u through hydrogen target. Also listed is skewness as defined by equation (2.14), which is very small and thus indicates a good symmetry of the distribution.

The excellent agreement between experimental value and Gaussian distribution encouraged us to look for semi-empirical formulas of average equilibrium charge state and the distribution width. With the knowledge of \bar{q} and d , we will be able to estimate the equilibrium charge state distribution without measurement.

4.2.4 Semi-empirical Formulas for \bar{q} And d

The measured average equilibrium charge state and the distribution width have been studied extensively. Several semi-empirical formulas have been used in looking for the best one for the projectile and target combinations of our interests¹.

Average Equilibrium Charge State \bar{q}

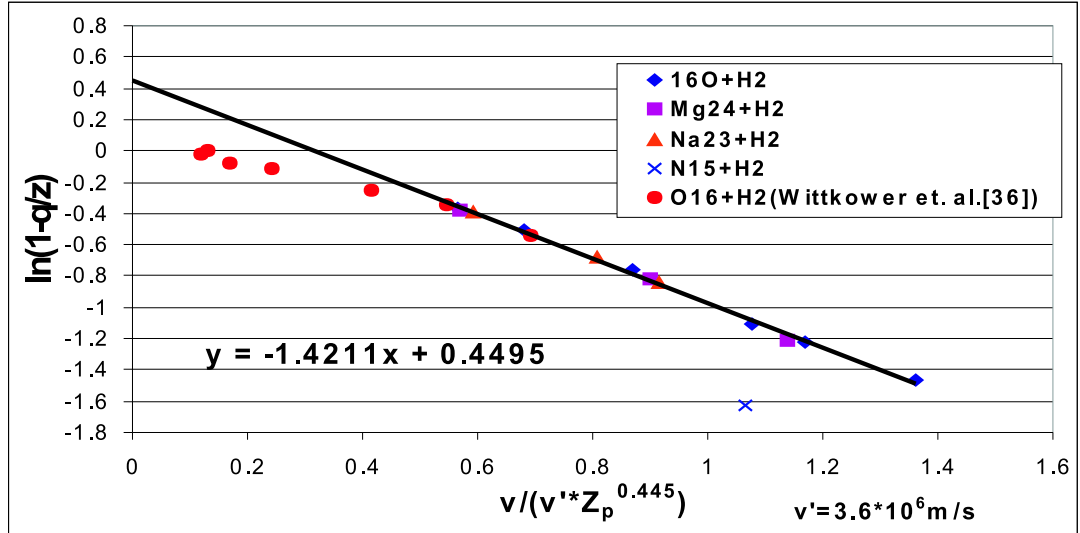
We first followed the suggestion of Betz et al. that, as shown by equation (2.16), the relation between the reduced average equilibrium charge state \bar{q}/Z_p and the reduced velocity $v/(v_0 Z_p^\gamma)$ can be expressed as

$$\ln\left(1 - \frac{\bar{q}}{Z_p}\right) = -\frac{v}{v_0 Z_p^\gamma} + C \quad (4.3)$$

where γ and C have been set as free parameters in the fitting. A good fit is not available until we release v_0 as free parameter too. To be comparable with other results, we took $v/(v' Z_p^\gamma)$ as the reduced velocity and introduced new parameters A and B as

¹ All notations here are used as defined in Chapter 2

(A)



(B)

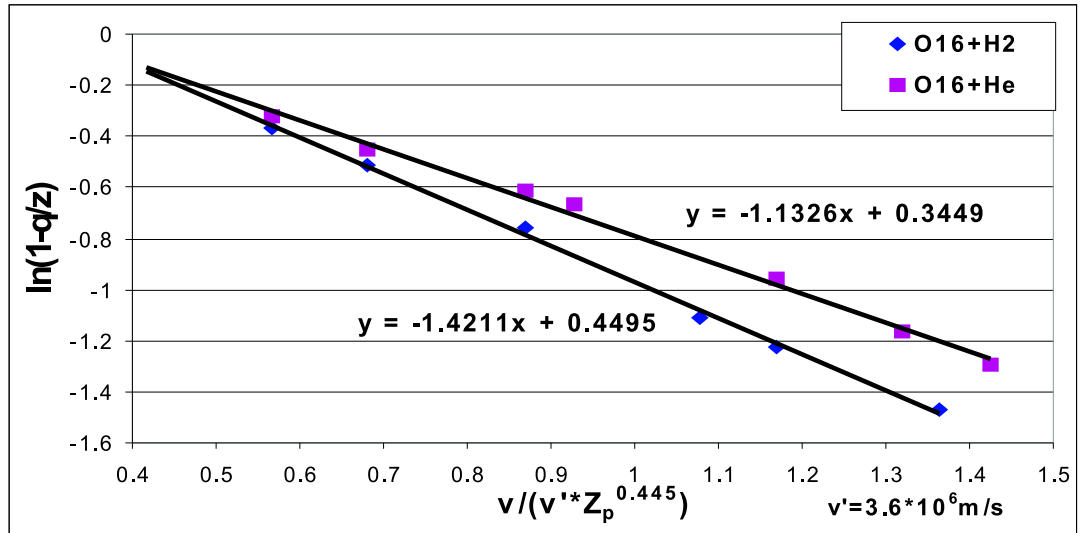


Figure 4.6: $\ln(1 - \bar{q}/z)$ plotted as a function of reduced velocity, with (A) for various projectiles passing through hydrogen target and (B) for oxygen beam passing through hydrogen and helium target, respectively.

$$\ln(1 - \frac{\bar{q}}{Z_p}) = -A \frac{v}{v' Z_p^\gamma} + B \quad (4.4)$$

The best fit for hydrogen gas target is reached at $\gamma = 0.44515$, $A = 1.4211$, $B = 0.4495$, and for Helium gas target $\gamma = 0.44515$, $A = 1.1326$, $B = 0.3449$, as shown in Figure 4.6(A) and (B). Our experimental data fall nicely on a line with a non-zero y intercept.

Also plotted in Figure 4.6(A) are the average equilibrium charge states of low energy ^{16}O passing through hydrogen gas target from literature [10]. Despite the great agreement in our energy range, it is clear that for reduced velocity less than 0.5, which corresponds to beam energy less than 0.1 MeV/u for ^{16}O , experimental data deviate away from the linear relation. This indicates that the expression determined cannot be extrapolated to very low energy region, where \bar{q} goes to zero at zero velocity.

We also tried the formula given by Nikolaev and Dmitriev for solid targets (equation (2.17)). Again, to make a fit to our data, new parameter A and B are introduced. And basically, the same low energy problem appears. The best fit to our data is

$$\frac{\bar{q}}{Z_p} = A[1 + (\frac{v}{v' Z_p^\alpha})^{-\frac{1}{k}}]^{(-k)} + B \quad (4.5)$$

with $\alpha = 0.45$, $k = 0.6$, $v' = 3.6 \times 10^6$ m/s, and $A = 1.0229$, $B = -0.0380$ for hydrogen gas target, $A = 0.9029$, $B = -0.0343$ for helium gas target (Figure 4.7).

Applying the complicated universal formula of Schiwietz to our data, the relative average charge state is plotted versus the function of the scaling parameter x defined by equation (2.19) and (2.20) as shown in Figure 4.8. Instead of getting $\bar{q}/Z_p = f(x)$, we got

$$\frac{\bar{q}}{Z_p} = 1.7725 f(x) - 0.8669 \quad (4.6)$$

where $f(x)$ represents the function on the right side of equation (2.19).

Among all these different fits, we determined equation(4.4) to be the best with the smallest χ^2 . To simplify the calculation, we represent the formula as

$$\bar{q} = Z_p \times [1 - \exp(-\frac{A}{Z_p^\gamma} \sqrt{\frac{E}{E'}} + B)] \quad (4.7)$$

where $\frac{1}{Z_p^\gamma} \sqrt{\frac{E}{E'}}$ is equivalent to the reduced velocity with E the projectile energy in unit of MeV/u and $E' = 0.067635$ MeV/u, which corresponds to $v' = 3.6 \times 10^6$ m/s.

What puzzles us is that data point of ^{15}N beam is out the general trend in all the fits. It is necessary to reproduce this point experimentally. However, this has to be postponed

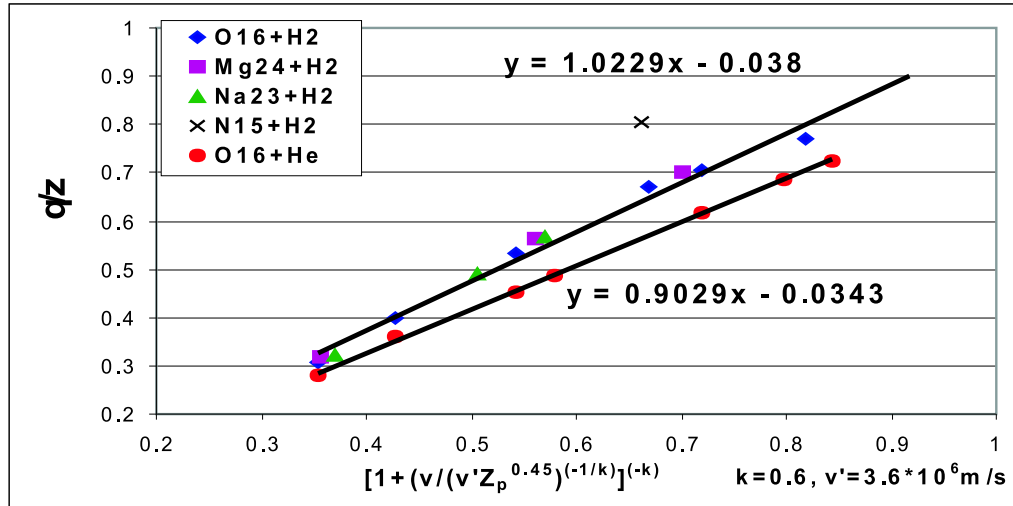


Figure 4.7: $\ln(1 - \bar{q}/z)$ plotted as a function of the expression determined by Nikolaev and Dmitriev[5].

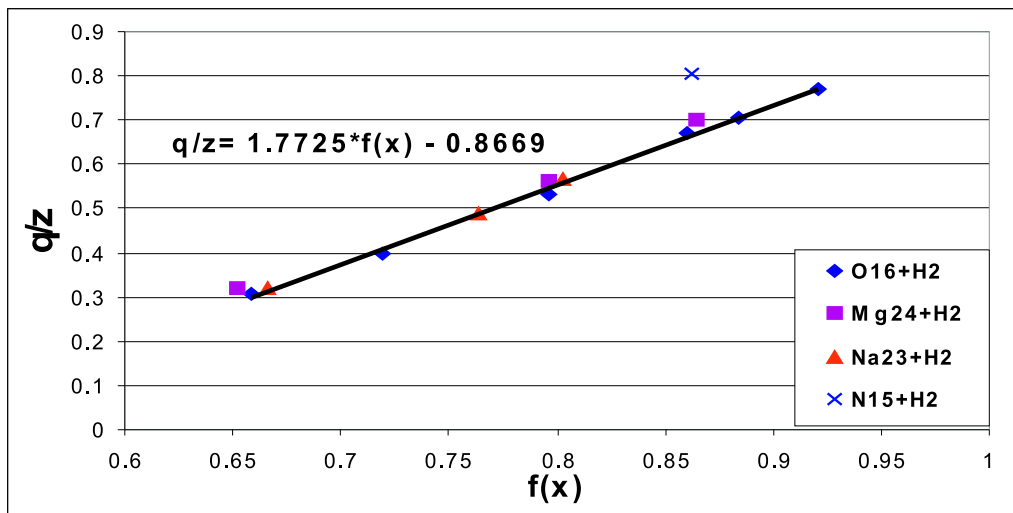


Figure 4.8: $\ln(1 - \bar{q}/z)$ plotted as a function of $f(x)$, given by Schiwietz[27].

since beam time was not made available for redoing this point as it was not considered high priority for DRAGON at this moment. It is interesting to mention that none of the existing semi-empirical formula in the literature can be fit to our experimental data without modification.

Distribution Width

The distribution width is a very sensitive parameter and no theoretical prediction is available yet.

Phenomenological observation of width from Table 4.3 shows the constancy over a wide range. Roughly, for the reduced charge state \bar{q}/Z_p in the range of $0.3 \sim 0.7$, the distribution width can be fitted with the expression

$$d = d_1 Z_p^w \quad (4.8)$$

with $d_1 = 0.23675$ and $w = 0.54772$, respectively.

While plotting the reduced width $d/Z_p^{0.54772}$ versus the average number of electron $\bar{n}(=Z_p - \bar{q})$ as suggested by Shima et al., the shell effect is obvious as shown in Figure 4.9.

Obviously, this is still not good enough to estimate distribution width, which is going to be used to calculate the equilibrium charge state distribution. Practically, interpolation in between our measured data (Figure 4.10) for each projectile and target combination will be more useful.

4.3 Single Electron Capture and Loss Cross Section

4.3.1 Least Squares Method

In our measurement, the observed slope at low target thickness showed significant deviation from linearity. Since we have measured charge state distribution at several thickness points from non-equilibrium to equilibrium, the least squares method has been adopted to fit the single electron capture and loss cross sections.

We initially used the MICROSOFT EXCEL program to fit the cross sections from a simple model. Assume that only one collision takes place when the projectile ion passes through a thin layer of the target. And since the probability of multiple electron capture and loss is negligible for low energy beam passing through dilute gas target, only single electron

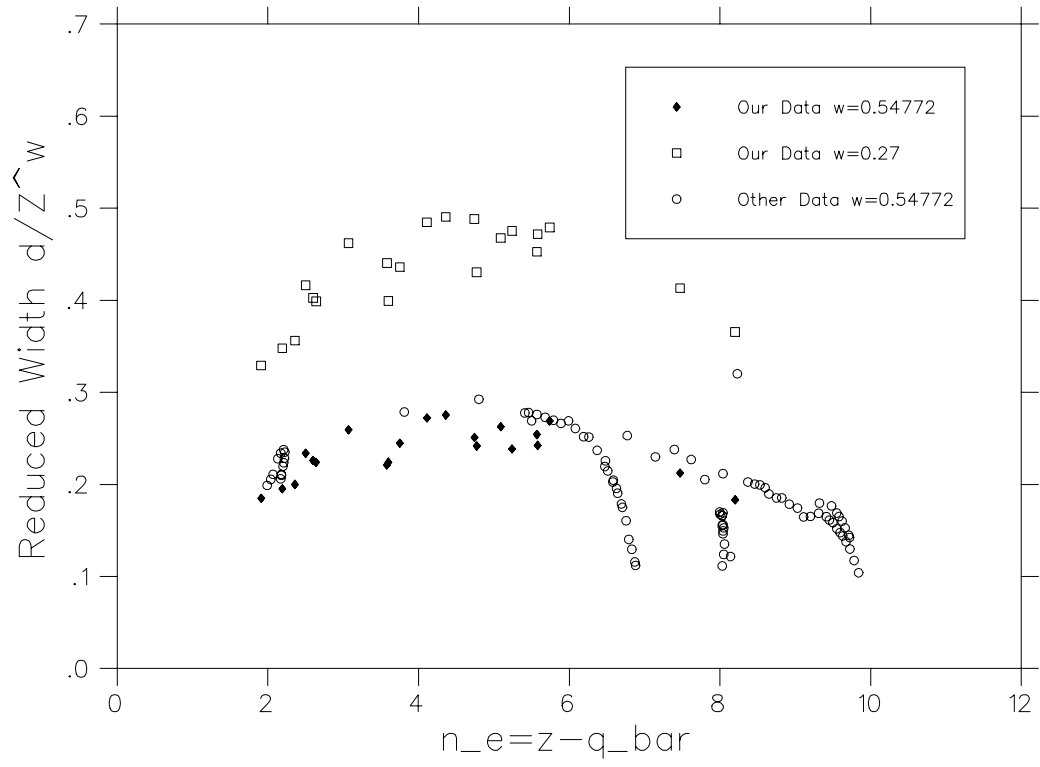


Figure 4.9: Reduced width $d/(Z_p^w)$ plotted as a function of mean number of electrons $n_e (= Z_p - \bar{q})$.

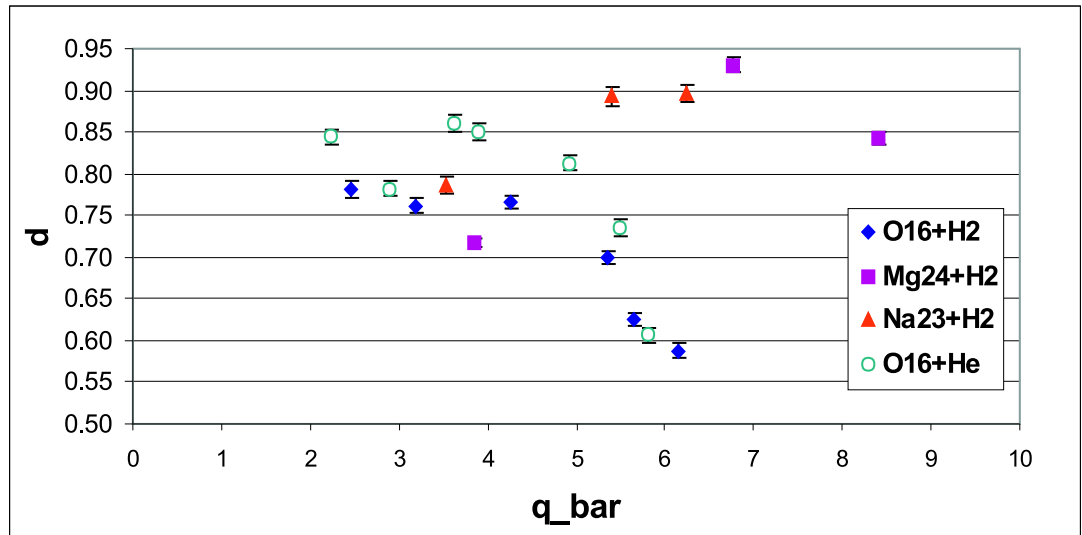


Figure 4.10: Distribution width d plotted as a function of relative average equilibrium charge state.

capture or loss process is considered. The change of the charge state fraction exiting each layer of thickness δx is estimated from equation (2.5) to be

$$\delta F_q = \delta x (F_{q+1} \sigma_{q+1,q} + F_{q-1} \sigma_{q-1,q} - F_q (\sigma_{q,q+1} + \sigma_{q,q-1})) \quad (4.9)$$

The χ^2 is calculated for all the charge state fractions measured and calculated, for the certain combination of projectile energy and target species. All the possible single electron capture and loss cross sections are set up as free parameters in the minimization of the χ^2 . Also, the fact that projectiles of different incident charge state should end up in the same equilibrium charge state distribution is used as a constraint in the fitting. The hydrogen molecule is simply treated as two atoms, and the cross sections we got are in unit of $cm^2/atom$.

With the cross sections fitted from excel as initial parameters, FORTRAN code is written to integrate the series of differential equations (2.5) numerically using the adaptive stepsize Runge-Kutta method. Again the χ^2 is calculated with all the possible single electron capture or loss cross sections as its free parameters. The minimization of the χ^2 was done by MINUIT program from CERN library. Since the parameters are highly correlated, a scan has been done for each cross section fitted to make sure it sits at the minimum of the χ^2 function.

The fitted charge changing cross sections related to charge states with low fraction F_q (say less than 1%) have large uncertainties because of the large uncertainties associated with the measured F_q . The improvement of this situation requires the availability of incident beam in these charge states.

All fitted cross sections with uncertainties are tabulated in Table 4.4. In cases when χ^2 per degree of freedom is larger than 1, the uncertainties have been multiplied by the square root of χ^2 per degree of freedom. And since the non-equilibrium charge state distribution depends on the target thickness, additional normalization was introduced by the uncertainty in the target effective length. Because of the inverse proportional relationship between the target thickness and the cross sections, it will basically affect all the fitted cross sections by $\pm 10\%$ (the uncertainty in the target effective length). The agreement of the growth curve calculated from these cross sections with the experimental data, as shown in Appendix A, indicates that the single electron capture and loss is a reasonable assumption.

As stated before, the charge distribution of lower energy beam passing through gas target reaches equilibrium at lower pressure, which indicates larger charge changing cross sections. Meanwhile, this also results in the fact that not enough data of non-equilibrium

charge distribution could be measured because of the limit in the precise measure of very low target pressure, namely, of the order of mTorr. So generally, the cross sections fitted for low energy beam have larger percentage uncertainties. In case of DRAGON's experiments, the distribution with only one incident charge state has been measured, so the corresponding cross sections were not well determined.

Limited by little published data available for directly comparison, we extrapolated data from Montenegro etc. [43] on $\sigma_{5,6}$ and $\sigma_{5,4}$ of oxygen beam passing through hydrogen, as shown in Table 4.6. Their data of cross sections have been fitted to single power law, e.g.

$$\sigma_{5,6} = aE^\beta \quad (4.10)$$

where a and β are free parameters. Then, corresponding cross sections of 0.138 MeV/u and 0.200 MeV/u ^{16}O beam passing through hydrogen and helium gas have been calculated and listed in Table 4.6 with our experimental data. Their cross sections with hydrogen target in unit of $\text{cm}^2/\text{molecule}$ have converted to unit of cm^2/atom by timing 2, simply from the point that a hydrogen molecule contains two atoms. Comparison with our data indicates good agreement. Other than this, we are not aware of any published data with which to compare the present measurements.

4.3.2 Scaling Rules for Cross Section

As discussed in Chapter 2, charge-changing cross sections are functions of projectile atomic number Z_p , target atomic number Z_t , ion charge state q and energy E . Following the result of simplified theoretical model, which gives simple power functions for the dependence of cross sections on these parameters, we checked the dependence of the cross sections on q and E , respectively, as shown in Figure 4.11, 4.12, 4.13, 4.14.

Single Electron Capture

As expected, single electron capture cross section $\sigma_{q,q-1}$ generally increases with q and decreases with E , which could be expressed in simple power law as

$$\sigma_{q,q-1} \propto q^\alpha E^\beta \quad (4.11)$$

In Bohr and Lindhard's theoretical predication [34], α is independent of projectile velocity and amounts to 3 in hydrogen and helium gas target. However, the value of α determined from our experimental data varies. In case of ^{16}O ions passing through hydrogen

Table 4.4: Single Electron Capture and Loss Cross sections for Heavy Ions, with * and † refer to data from Naples and DRAGON measurements, respectively. Uncertainties of the cross sections have been normalized to make χ^2 per freedom be 1.0. Additional normalization of all the cross sections with respect to the uncertainty in the target effective length are not included here.

	$E(\text{MeV/u})$	<i>Single Electron Capture</i>			<i>Single Electron Loss</i>		
		q	q'	$\sigma_{q,q'}(10^{-18}\text{cm}^2)$	q	q'	$\sigma_{q,q'}(10^{-18}\text{cm}^2)$
$^{16}\text{O} + H_2^*$	0.138	2	1	19.6 ± 5.2	1	2	81.0 ± 20.8
		3	2	29.4 ± 4.1	2	3	26.5 ± 3.6
		4	3	68.1 ± 3.3	3	4	12.2 ± 1.9
		5	4	126.6 ± 46.3	4	5	5.9 ± 0.7
$^{16}\text{O} + H_2^*$	0.200	3	2	10.0 ± 1.0	2	3	27.8 ± 3.5
		4	3	17.1 ± 2.3	3	4	10.6 ± 1.5
		5	4	69.5 ± 11.2	4	5	7.9 ± 0.8
		6	5	150.1 ± 105.5	5	6	2.1 ± 0.7
$^{16}\text{O} + H_2^*$	0.325	3	2	2.1 ± 1.1	2	3	25.1 ± 8.0
		4	3	3.1 ± 0.3	3	4	11.2 ± 0.6
		5	4	7.5 ± 0.6	4	5	5.4 ± 0.5
		6	5	14.8 ± 5.8	5	6	2.0 ± 0.6
$^{16}\text{O} + H_2^\dagger$	0.500	5	4	1.6 ± 0.2	4	5	6.9 ± 0.4
		6	5	2.4 ± 0.4	5	6	2.7 ± 0.2
		7	6	4.2 ± 2.5	6	7	0.04 ± 0.02
$^{16}\text{O} + H_2^\dagger$	0.800	5	4	0.18 ± 0.03	4	5	4.5 ± 0.1
		6	5	0.25 ± 0.02	5	6	1.8 ± 0.1
		7	6	0.33 ± 0.05	6	7	0.15 ± 0.01
		8	7	0.36 ± 0.15	7	8	0.02 ± 0.01
$^{23}\text{Na} + H_2^*$	0.200	3	2	4.8 ± 0.4	2	3	27.7 ± 2.5
		4	3	15.7 ± 0.8	3	4	15.1 ± 0.8
		5	4	37.7 ± 1.7	4	5	8.1 ± 0.5
		6	5	66.8 ± 4.3	5	6	4.6 ± 0.5
$^{23}\text{Na} + H_2^*$	0.374	4	3	1.4 ± 0.4	3	4	17.9 ± 5.7
		5	4	2.1 ± 0.2	4	5	6.7 ± 0.4
		6	5	5.3 ± 0.5	5	6	4.8 ± 0.4
		7	6	10 ± 2.4	6	7	2.7 ± 0.5
		8	7	15.1 ± 10.2	7	8	0.84 ± 0.14

Table 4.5: Single Electron Capture and Loss Cross sections for Heavy Ions, with * and † refer to data from Naples and DRAGON measurements, respectively (continued). Uncertainties of the cross sections have been normalized to make χ^2 per freedom be 1.0. Additional normalization of all the cross sections with respect to the uncertainty in the target effective length are not included here.

	$E(\text{MeV/u})$	<i>Single Electron Capture</i>			<i>Single Electron Loss</i>		
		q	q'	$\sigma_{q,q'}(10^{-18}\text{cm}^2)$	q	q'	$\sigma_{q,q'}(10^{-18}\text{cm}^2)$
$^{23}\text{Na} + \text{H}_2^*$	0.478	4	3	0.67 ± 0.26	3	4	14.8 ± 8.1
		5	4	0.72 ± 0.17	4	5	6.7 ± 0.6
		6	5	1.8 ± 0.2	5	6	4.4 ± 0.6
		7	6	3.6 ± 0.6	6	7	2.7 ± 0.2
		8	7	4.3 ± 1.9	7	8	1.1 ± 0.2
		9	8	11.9 ± 10.8	8	9	6.4 ± 0.2
$^{24}\text{Mg} + \text{H}_2^\dagger$	0.200	4	3	11.8 ± 0.1	3	4	16.0 ± 0.2
		5	4	36.7 ± 0.4	4	5	10.7 ± 0.4
		6	5	64.6 ± 0.4	5	6	4.7 ± 0.1
$^{24}\text{Mg} + \text{H}_2^\dagger$	0.500	5	4	2.0 ± 0.4	4	5	25.0 ± 4.4
		6	5	3.2 ± 0.6	5	6	12.2 ± 4.0
		7	6	3.2 ± 1.1	6	7	4.6 ± 0.6
		8	7	6.7 ± 0.4	7	8	2.9 ± 0.2
		9	8	8.3 ± 0.4	8	9	1.1 ± 0.9
$^{24}\text{Mg} + \text{H}_2^\dagger$	0.800	7	6	0.72 ± 0.20	6	7	5.4 ± 0.3
		8	7	0.82 ± 0.27	7	8	3.2 ± 0.3
		9	8	1.7 ± 0.3	8	9	1.6 ± 0.3
		10	9	2.0 ± 1.3	9	10	0.50 ± 0.20
$^{16}\text{O} + \text{He}^*$	0.138	2	1	15.5 ± 4.5	1	2	33.5 ± 10.8
		3	2	127.2 ± 8.0	2	3	78.3 ± 5.8
		4	3	218.0 ± 75.1	3	4	49.7 ± 17.6
		5	4	357.1 ± 191.5	4	5	14.7 ± 10.1
$^{16}\text{O} + \text{He}^*$	0.200	3	2	48.8 ± 6.0	2	3	68.4 ± 10.8
		4	3	69.8 ± 12.3	3	4	28.1 ± 4.8
		5	4	154.3 ± 28.6	4	5	15.9 ± 3.1
		6	5	292.1 ± 173.9	5	6	10.0 ± 8.9
$^{16}\text{O} + \text{He}^*$	0.325	3	2	16.0 ± 1.5	2	3	69.7 ± 7.0
		4	3	31.0 ± 2.2	3	4	38.0 ± 2.2
		5	4	41.0 ± 6.3	4	5	14.2 ± 1.9
		6	5	136.1 ± 10.4	5	6	6.8 ± 0.5

Table 4.6: Comparison of charge-changing cross sections for O^{5+} in H_2 and He with literature[43].

<i>Cross Section Data from Montenegro et al.</i>				
	<i>H₂ Target</i>		<i>He Target</i>	
<i>E(MeV)</i>	$\sigma_{5,6}(10^{-18}cm^2)$	$\sigma_{5,4}(10^{-18}cm^2)$	$\sigma_{5,6}(10^{-18}cm^2)$	$\sigma_{5,4}(10^{-18}cm^2)$
2.0	1.6±0.2	597±66	1.2±0.1	448±54
2.5	2.4±0.2	283±31	2.4±0.3	289±35
3.0	3.7±0.4	241±29	3.3±0.4	229±27
3.5	4.1±0.4	107±1.2	4.2±0.5	183±22
4.0	5.2±0.5	50.4±5.5	5.3±0.6	91.2±11
<i>Extrapolated Data verse Our Experimental Data</i>				
	<i>H₂ Target</i>			
<i>E (MeV/u)</i>	$\sigma_{5,6}(10^{-18}cm^2)$		$\sigma_{5,4}(10^{-18}cm^2)$	
	<i>Extrapolated Data</i>	<i>Our Data</i>	<i>Extrapolated Data</i>	<i>Our Data</i>
0.138			242.0± 10%	126.6±46.3
0.200	1.83±10%	2.1±0.7	67.6± 10%	69.5±11.2
	<i>He Target</i>			
<i>E (MeV/u)</i>	$\sigma_{5,6}(10^{-18}cm^2)$		$\sigma_{5,4}(10^{-18}cm^2)$	
	<i>Extrapolated Data</i>	<i>Our Data</i>	<i>Extrapolated Data</i>	<i>Our Data</i>
0.137			395.2±10%	357.1±191.5
0.200			177.3±10%	154.3±28.3

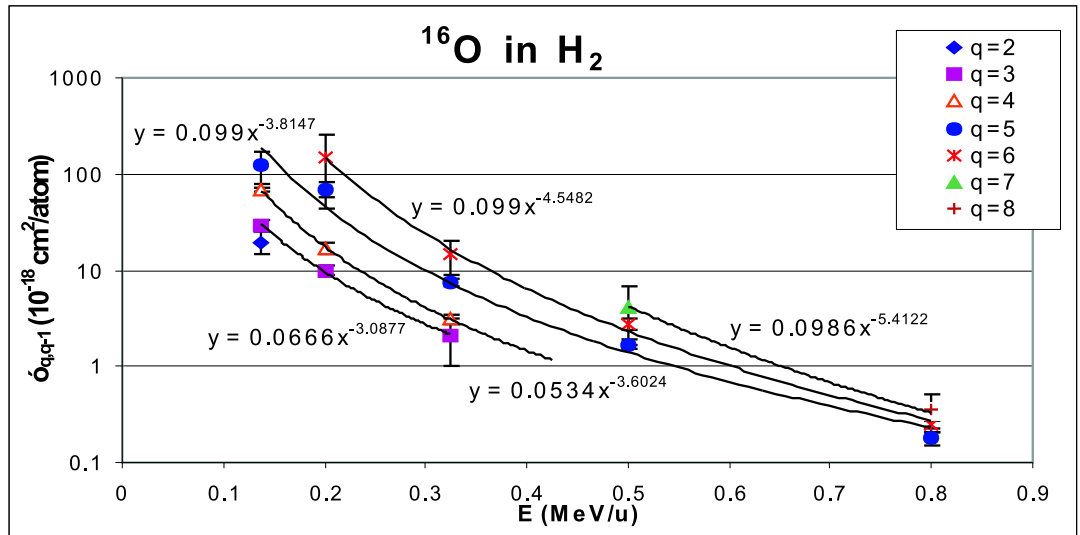
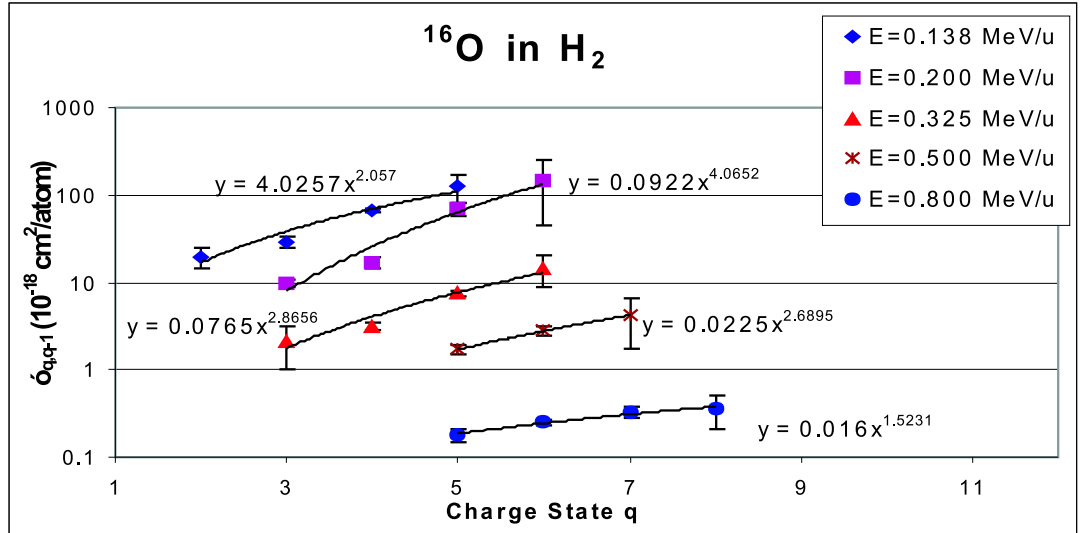


Figure 4.11: Single electron capture cross section of ^{16}O beam passing through hydrogen gas target plotted as a function of charge state q and projectile energy E , respectively.

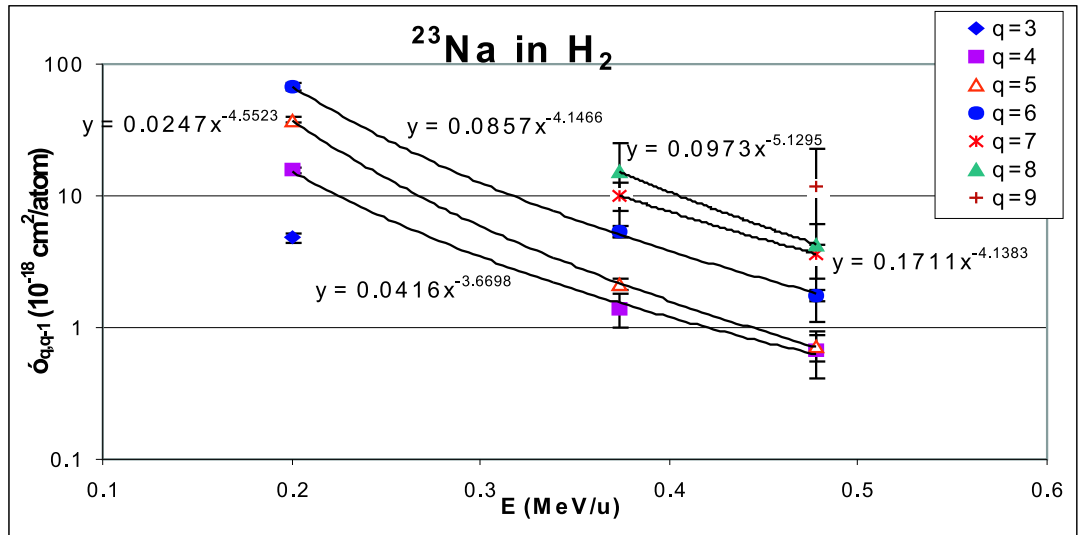
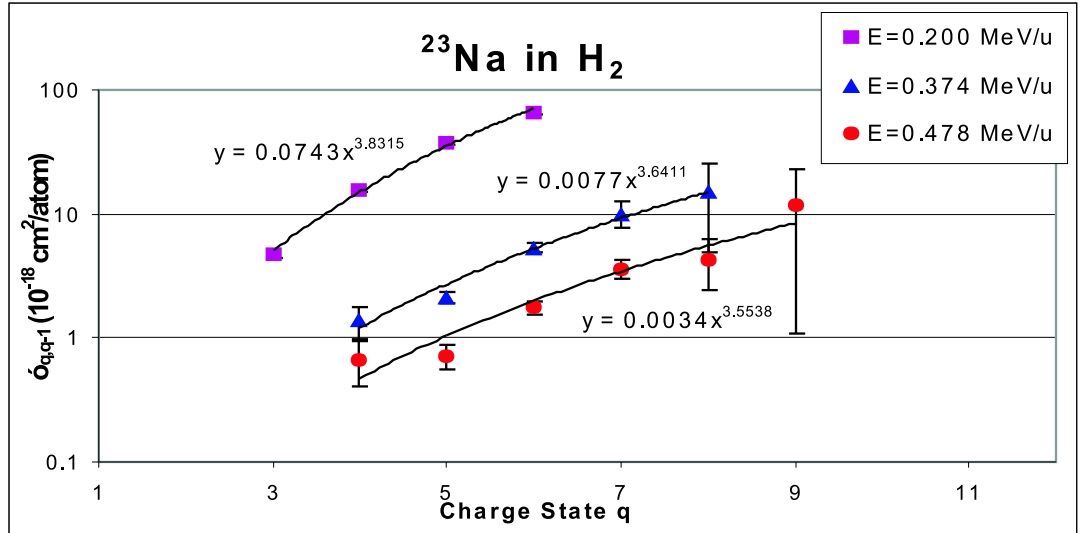


Figure 4.12: Single electron capture cross section of ^{23}Na beam passing through hydrogen gas target plotted as a function of charge state q and projectile energy E , respectively.

target, α seem to have a maximum at low energy and then decreases while the ion velocity increases. As shown in Figure 4.11, $\alpha \simeq 2.06, 4.07, 2.87, 2.69, 1.52$ for beam of 0.138, 0.200, 0.325, 0.500 and 0.800 MeV/u, respectively. In other cases, a monotonical decrease of α has been observed within the energy range of our measurement. For example, $\alpha \simeq 3.83, 3.64, 3.55$ at 0.200, 0.374 and 0.478 MeV/u, respectively, for ^{23}Na ions passing through hydrogen target. This basically contradicts with the published observation that the power of q is a increasing function of velocity for projectile with velocity larger than Bohr electron orbital velocity (2.18×10^6 m/s) [44, 45]. Our observation indicates that the power of q increases to a maximum and then monotonically decreases for projectile of higher velocity.

As the single capture cross sections of a certain charge state are plotted as function of projectile energy, we noticed that it decreases while E increases. β values are determined to be -3.09, -3.60, -3.81, -4.55, and -5.41 for ^{16}O projectile at 0.138, 0.200, 0.325, 0.500 and 0.800 MeV/u, respectively. Generally, β values fitted are in the range $-6 \sim -3$ from our measurement. Bohr and Lindhard's predication gives a velocity dependence v^{-7} , which is equivalent to an energy dependence $E^{-3.5}$. This falls in the range of β determined from our measurement.

Comparing the single electron capture cross section $\sigma_{4,3}, \sigma_{5,4}$ of 0.200 MeV/u $^{16}\text{O}, ^{23}\text{Na}$ and ^{24}Mg , we notice the general trend of a slow decrease in single electron capture section with the increase of the projectile atomic number. However, it increases with target atomic number as can be seen from the data for ^{16}O passing through hydrogen and helium, respectively.

Single Electron Loss

Different from capture cross sections, for roughly $0.25 < q/Z_p < 0.75$, loss cross sections of different projectile energy fall on a unique curve when plotted as a function of charge state as shown in Figure 4.13, 4.14 for ^{16}O and ^{23}Na passing through hydrogen. This indicates that there is no systematic dependence of single electron loss cross section on projectile energy. However, for really low and high charge state, the cross sections deviate from the general curve.

The power law dependence of the general curve can be expressed as

$$\sigma_{q,q+1} \propto q^\gamma \quad (4.12)$$

and γ is determined to be -2.67 and -3.13 for ^{16}O and ^{23}Na respectively.

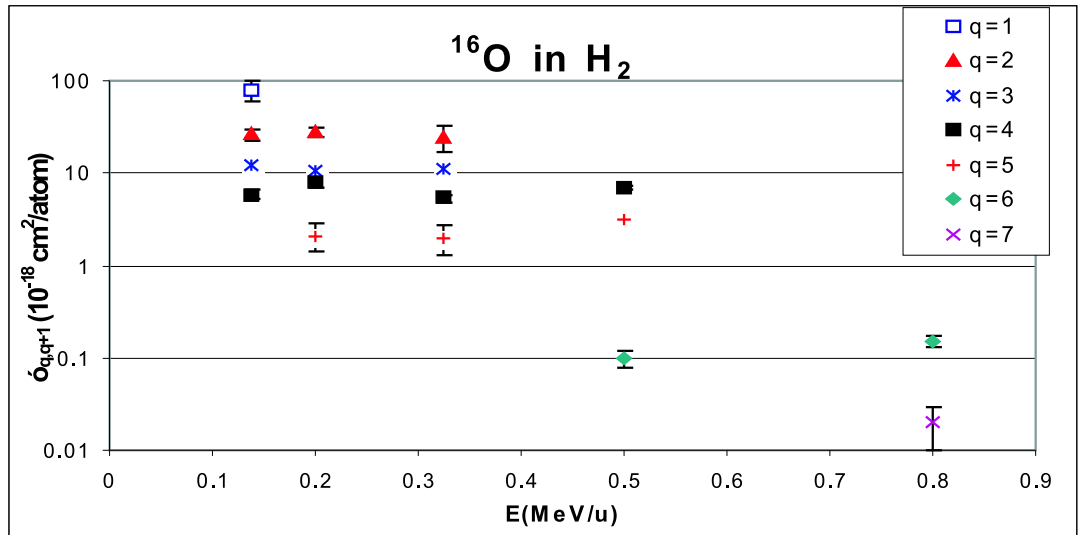
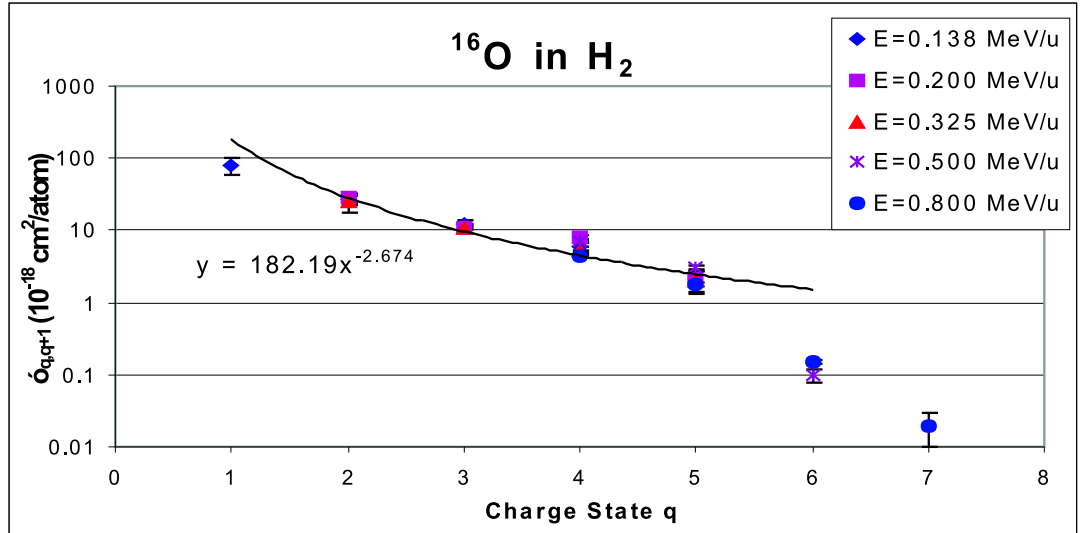


Figure 4.13: Single electron loss cross section of ^{16}O beam passing through hydrogen gas target plotted as a function of charge state q and projectile energy E , respectively.

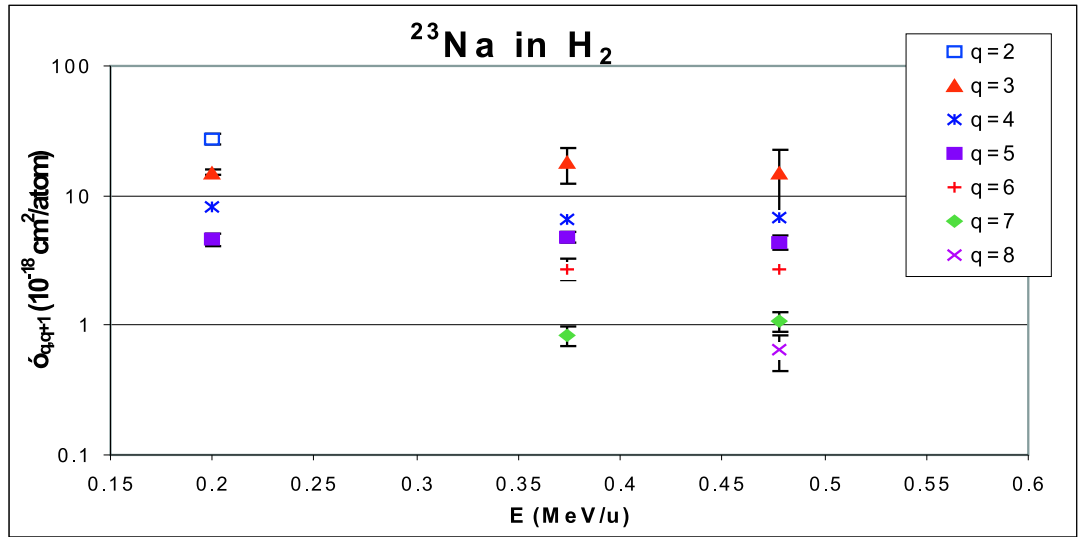
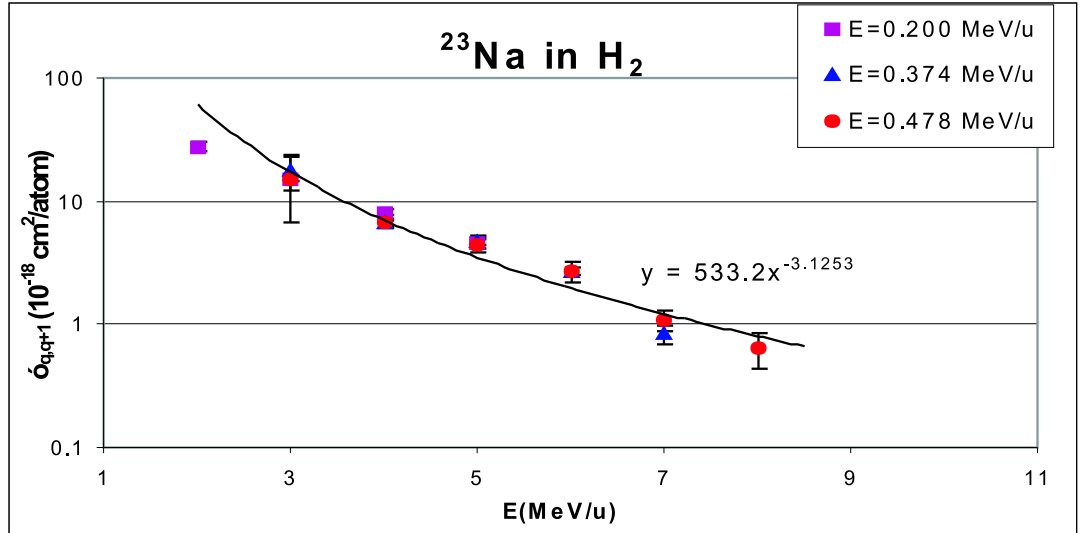


Figure 4.14: Single electron loss cross section of ^{23}Na beam passing through hydrogen gas target plotted as a function of charge state q and projectile energy E , respectively.

Again comparing the single electron loss cross section $\sigma_{3,4}, \sigma_{4,5}$ and $\sigma_{5,6}$ of 0.200 MeV/u ^{16}O , ^{23}Na and ^{24}Mg , we notice that single electron loss section increases slowly with the increase of the projectile atomic number Z_p . In case of the dependence on target atomic number, in general, it increase with target atomic number, except for $\sigma_{1,2}$ of ^{16}O passing through hydrogen and helium.

In conclusion, because of the diversity in the dependence of these charge changing cross sections on all the parameters, no universal fit as equation (2.30, 2.33) can be achieved from our data.

At a certain energy, equating the single electron capture cross section with the loss cross section gives the equilibrium average charge state.

Chapter 5

Conclusion

The use of the windowless gas target along with the operation of the DRAGON recoil mass separator placed a demand on understanding the charge state distribution of ions passing through gas target. Our study has contributed to this knowledge.

Since charge-changing is a complicated many-body collision process, no theory is available to predict the distribution accurately, and the use of semi-empirical formula is limited to a certain range. It is interesting to point out that we found none of the empirical or semi-empirical formulas published previously can be applied to our case directly.

We have not only measured the charge state distributions that is not available in the literature, but also unambiguously developed semi-empirical formulas for estimating average equilibrium charge states and distribution widths for low energy heavy ion passing through hydrogen and helium gas target. These formulas are useful to predict the equilibrium charge state distribution with the energy range from 0.138 MeV/u to 0.875 MeV/u. Extrapolation is dangerous and not recommended. As has been discussed, at least for very low energy range (i.e. < 0.1 MeV/u for O passing through hydrogen), formula (4.7) can not represent the expected relation.

Single electron capture and loss cross sections have been estimated using least squares methods. This qualitatively agrees with the theoretical prediction based on the assumption that those target electrons whose orbital velocities are close to the ion velocity are preferentially captured. The energy and velocity dependence predicted by Bohr and Lindhard as q^3 , v^{-7} (or equivalently, $E^{-3.5}$) for single electron capture cross sections, and q^{-3} for single electron loss cross section is within the range determined from our experimental data. However, we found that the dependence on q and E for capture cross section and on q for loss cross section varies, thus a universal scaling rule is not available.

Further studies are required to understand completely charge-changing processes of low energy heavy ions passing through hydrogen and helium gas. Systematic studies like the effects of the shell structure on the distribution are needed to be expanded.

Appendix A

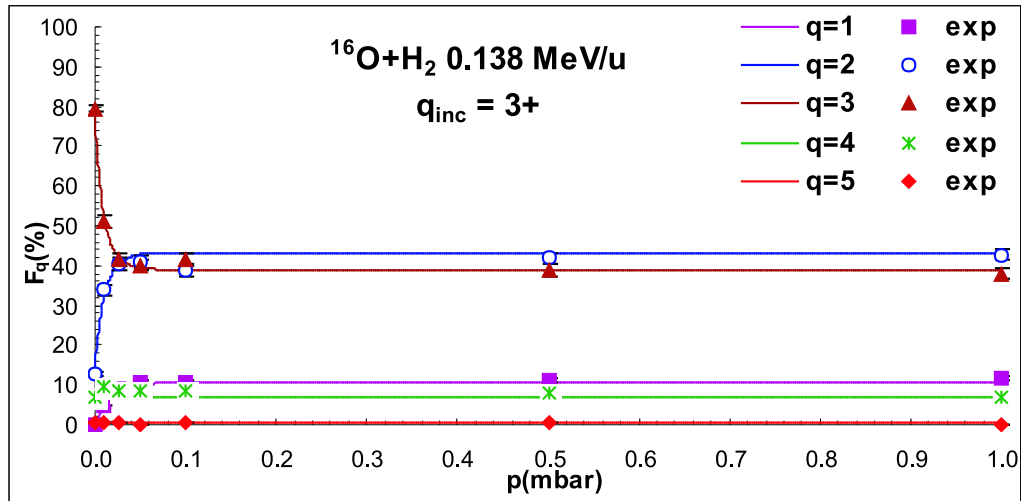
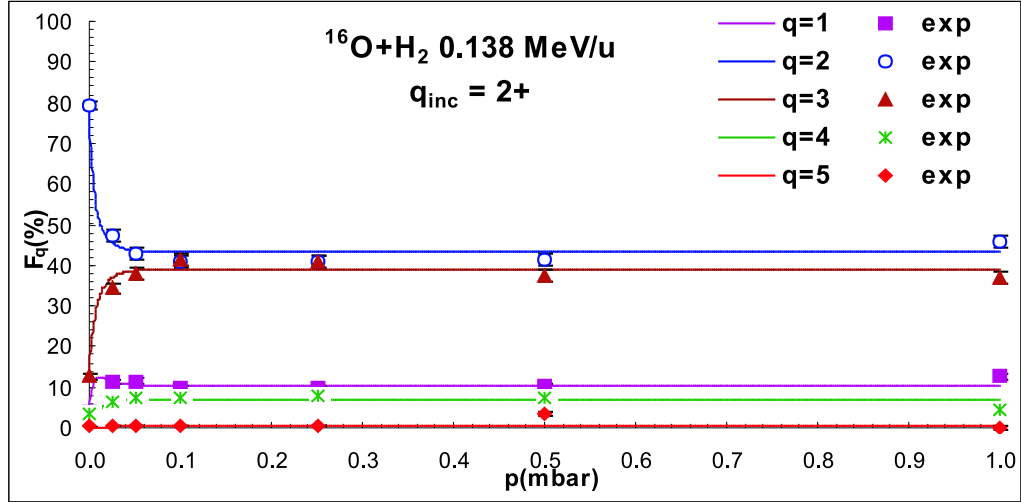
Compilation of Measured Growth Curves

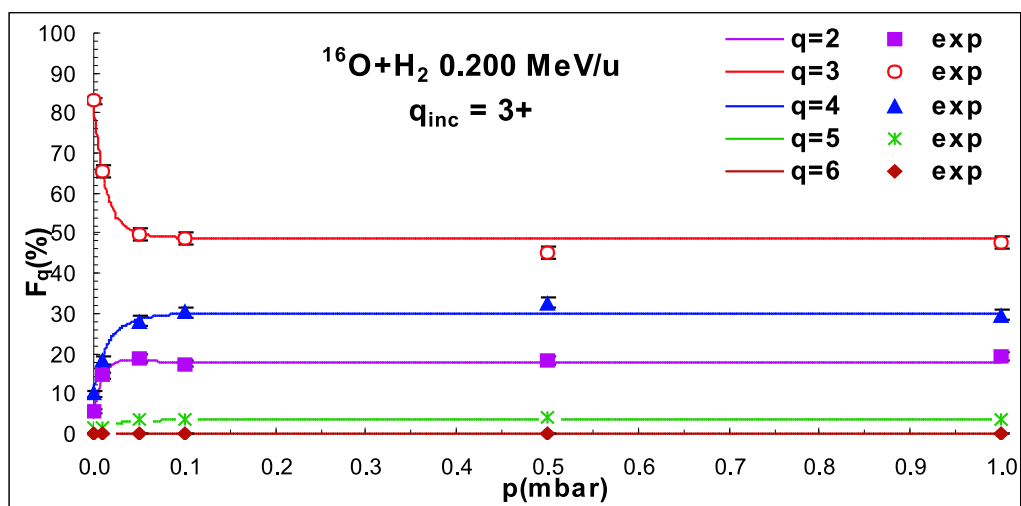
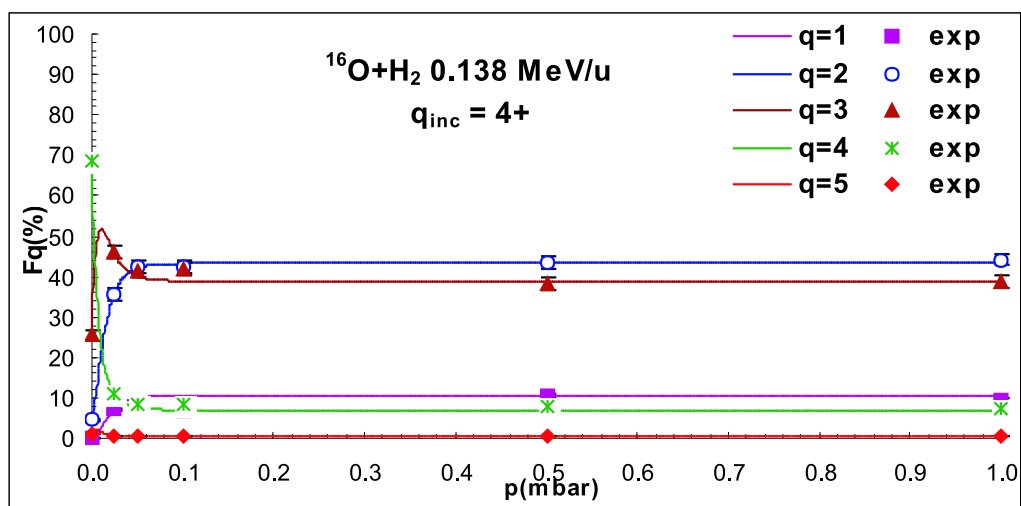
Presented here are the experimental determined, fractional charge state distributions as a function of target gas pressure. The solid symbols represent the experimental data, while the lines come from numerical integration of the differential equations (2.5) with the single electron capture and loss cross sections fitted by the least squares method.

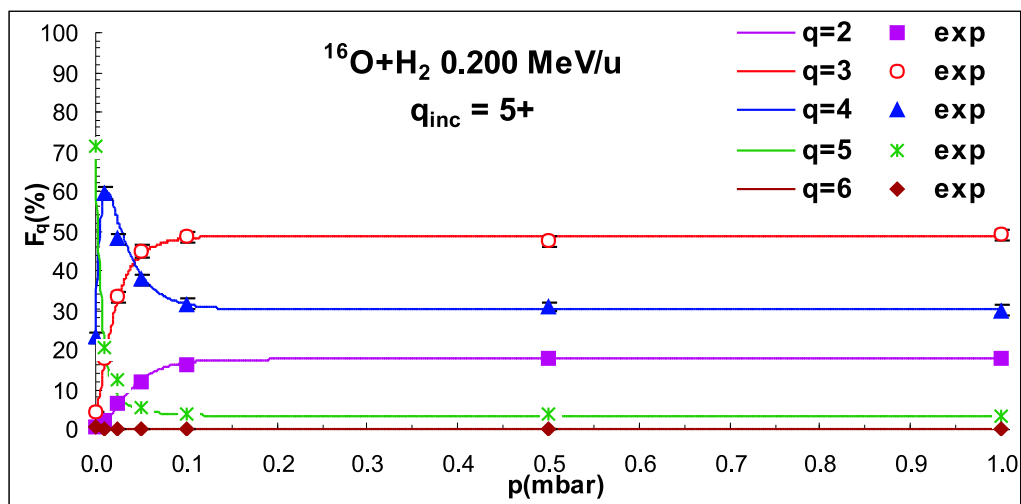
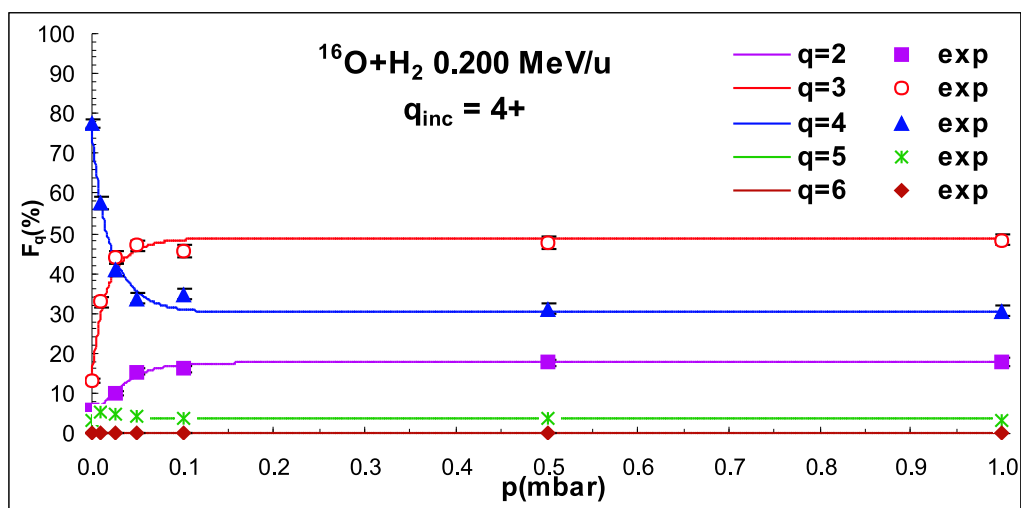
The energy labeled here are that of the incident beam since energy loss is different at different target thickness.

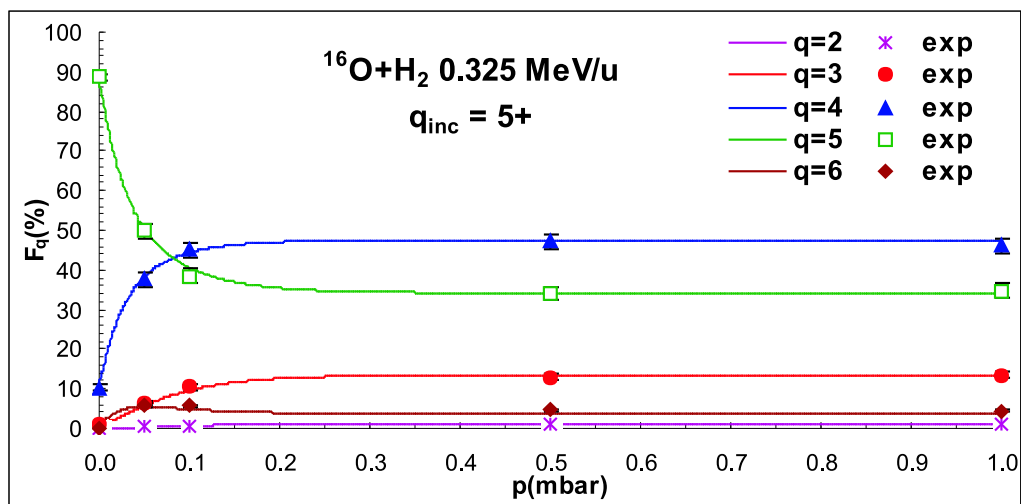
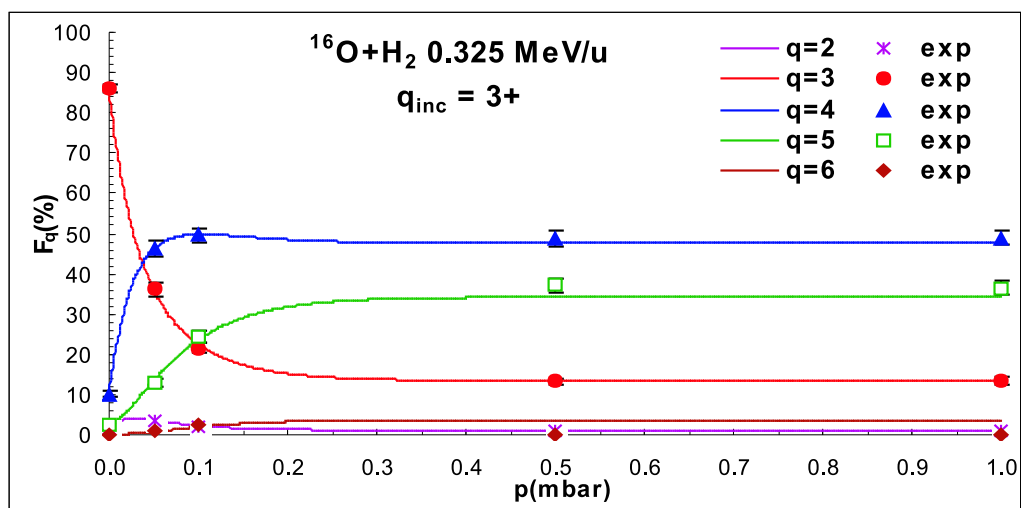
The first part shows the results from experiments done at Naples, while the second part from DRAGON/ISAC.

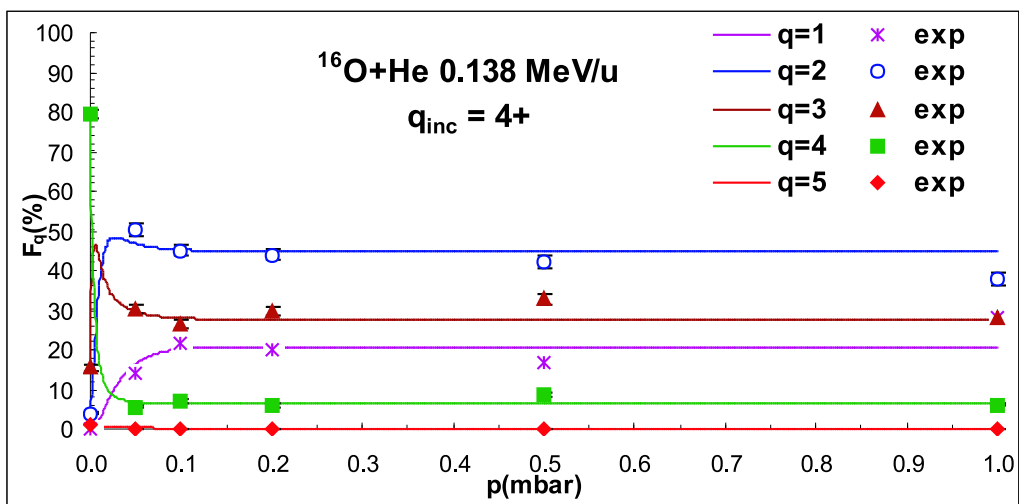
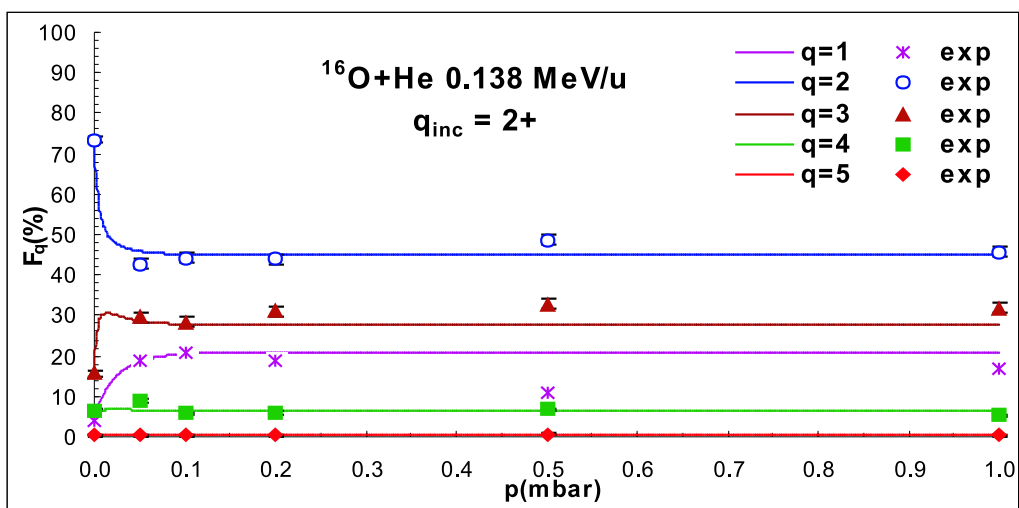
A.1 Naples Experiment Results

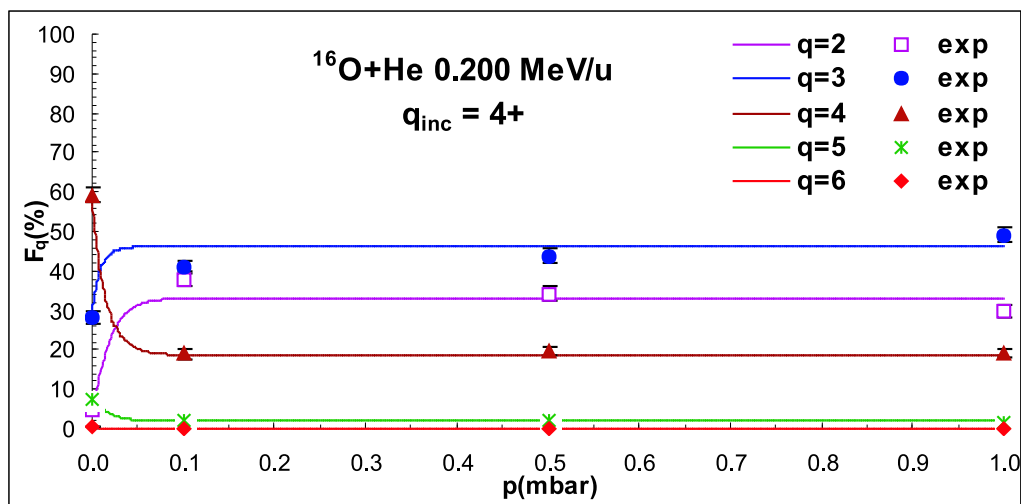
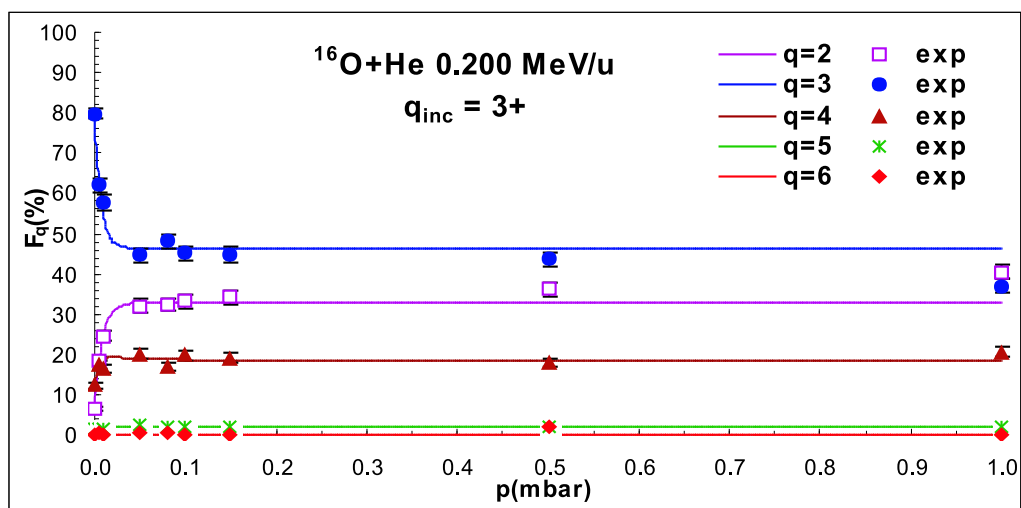


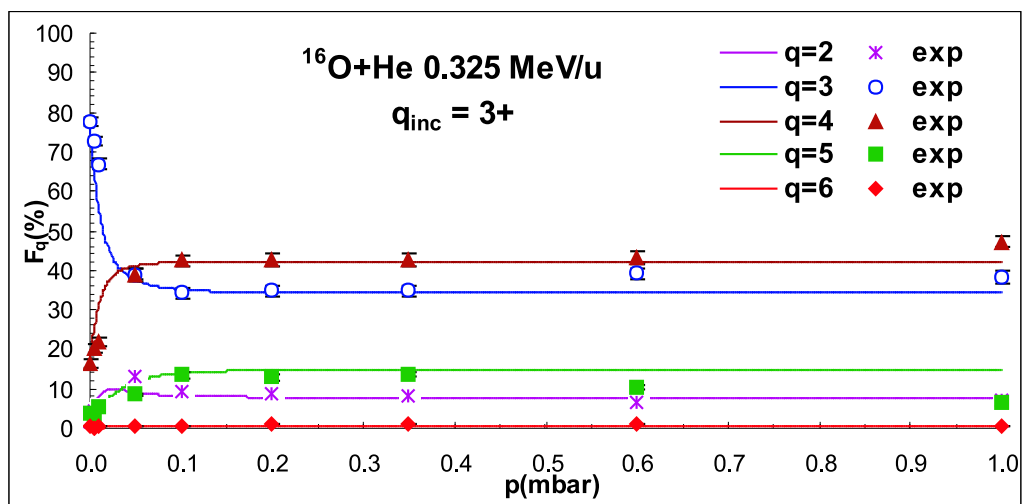
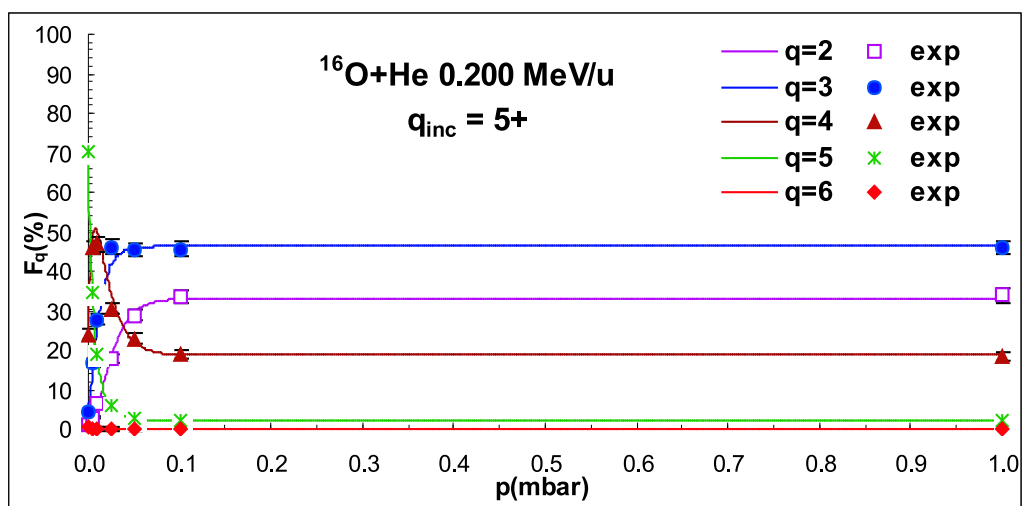


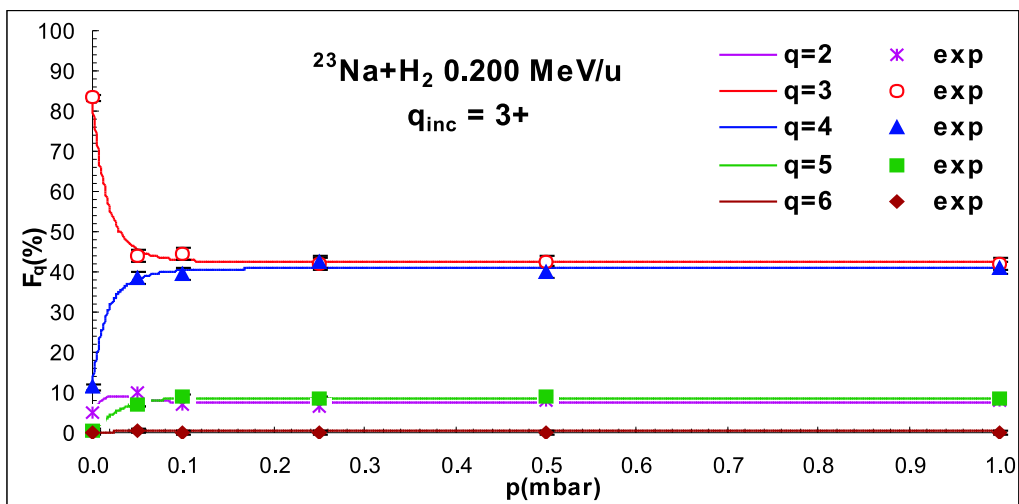
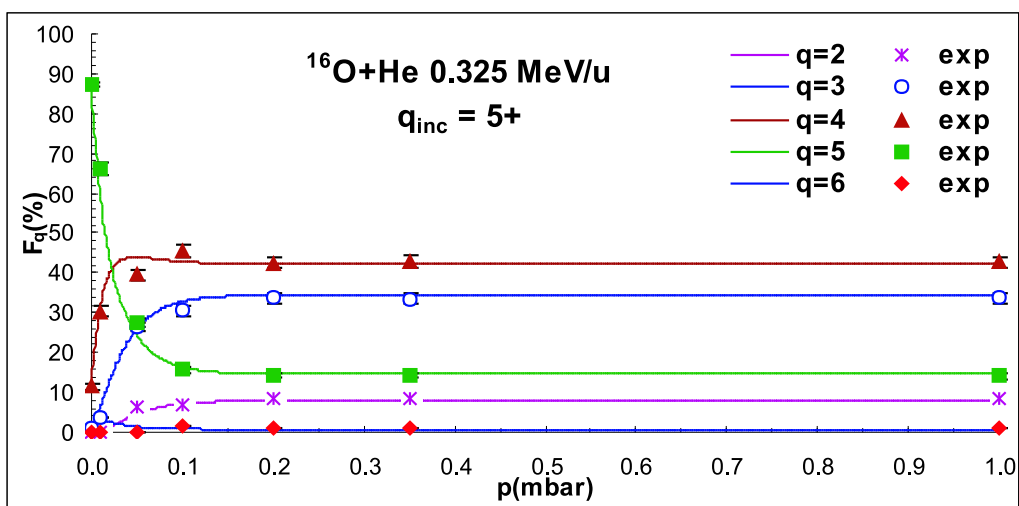


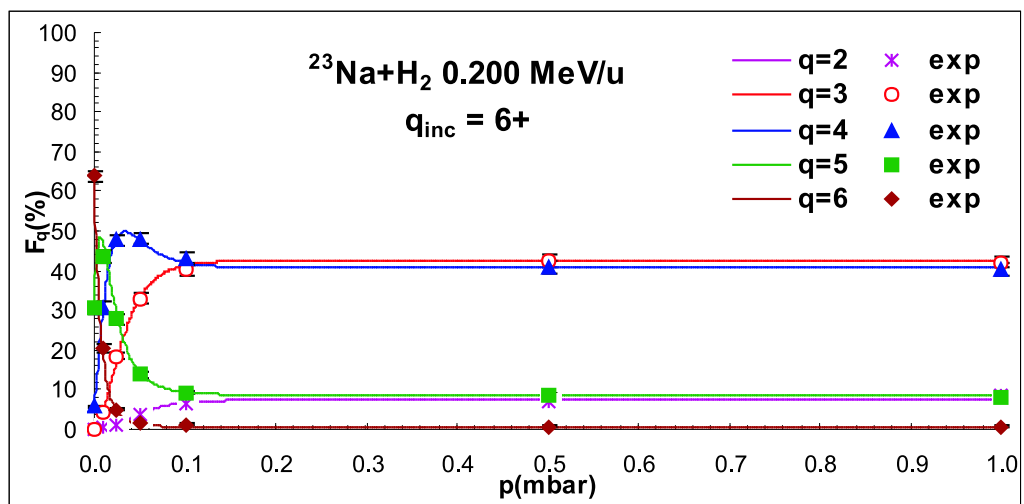
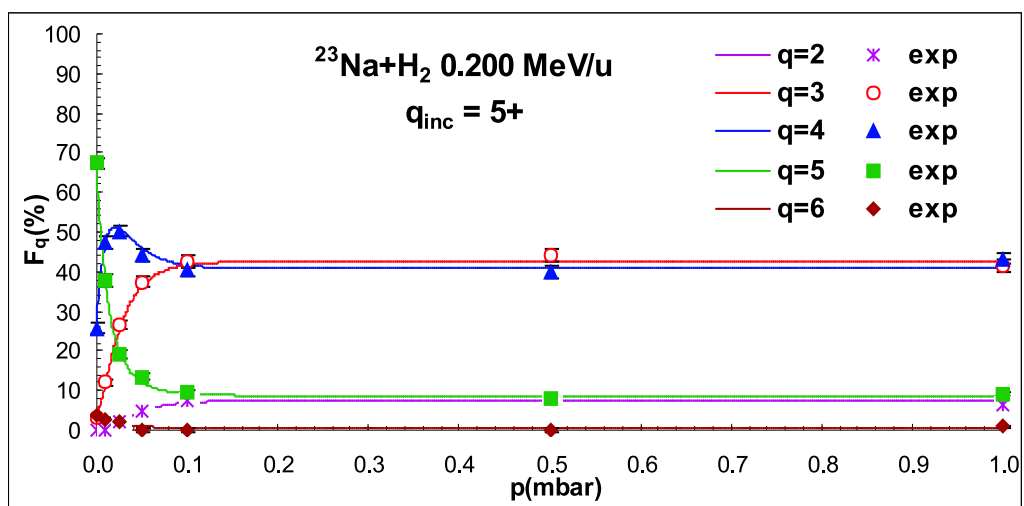


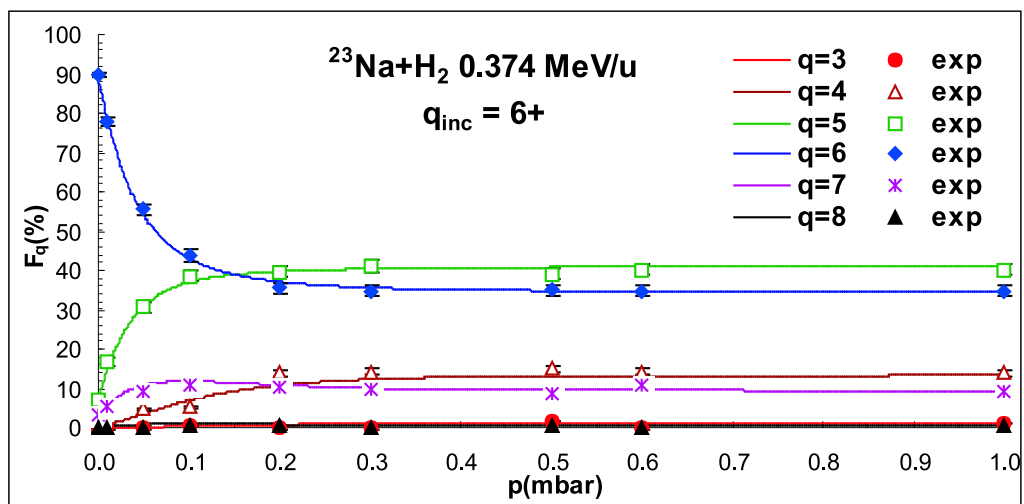
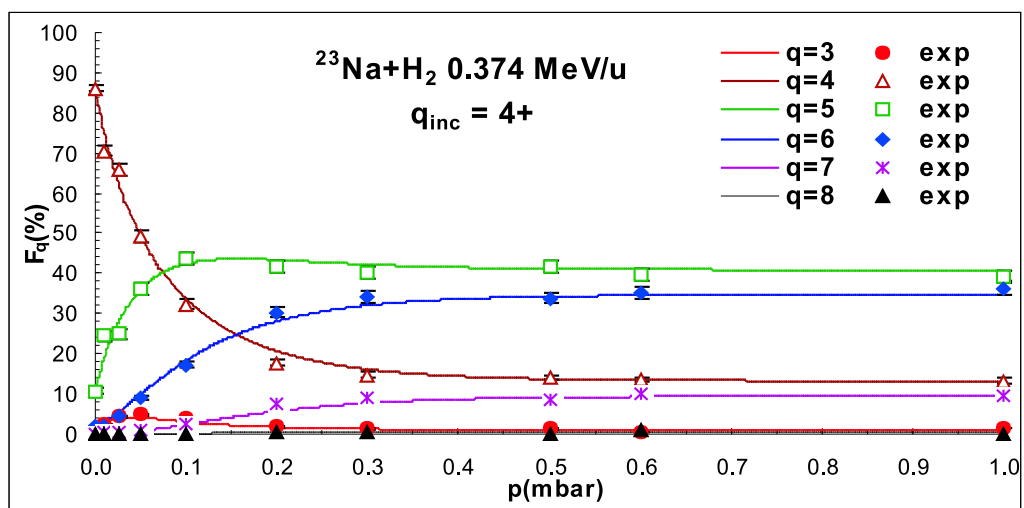


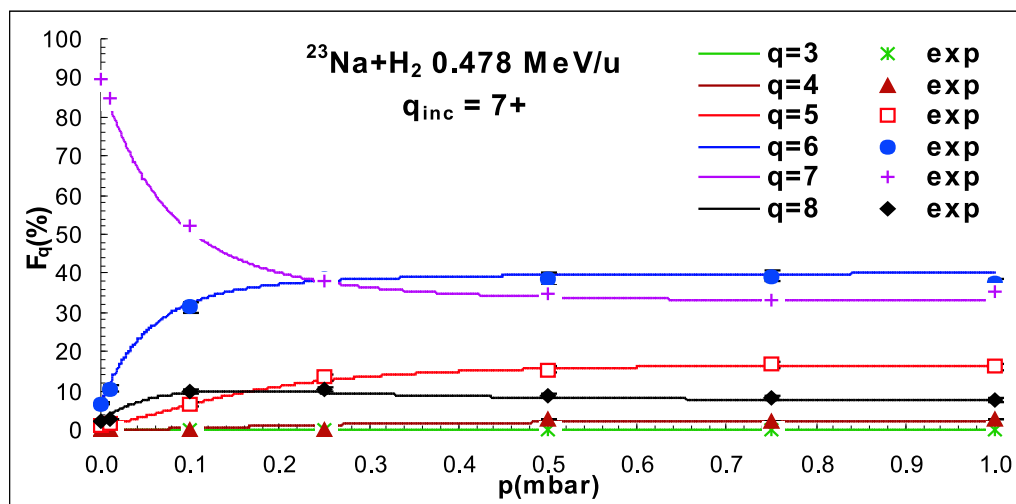
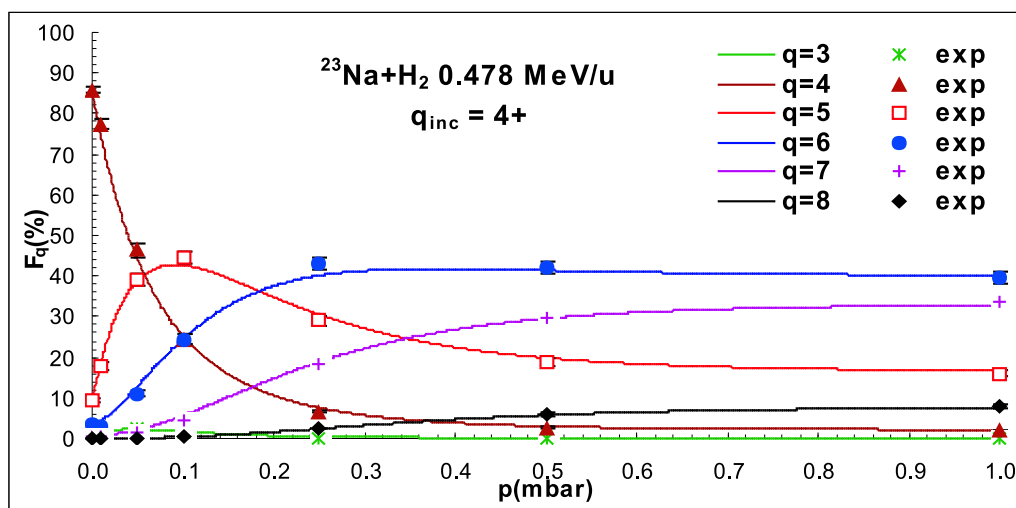




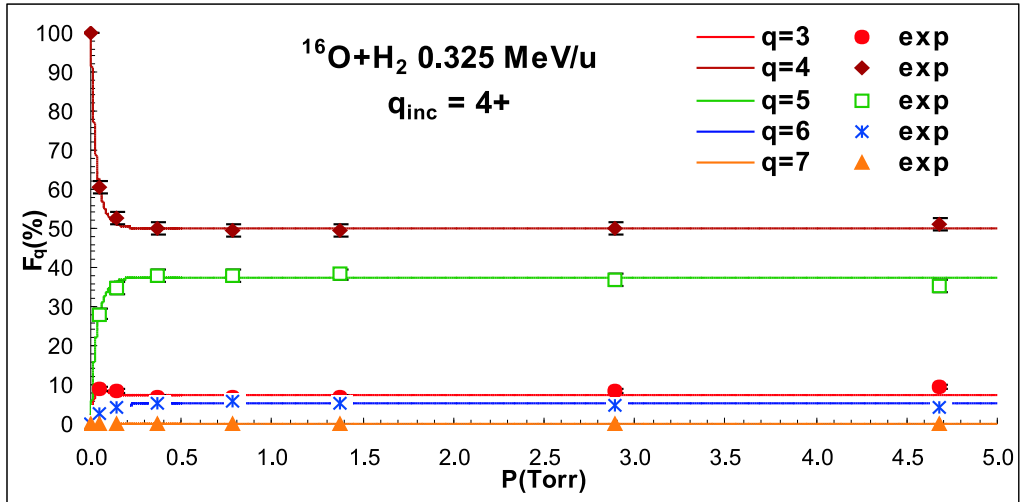
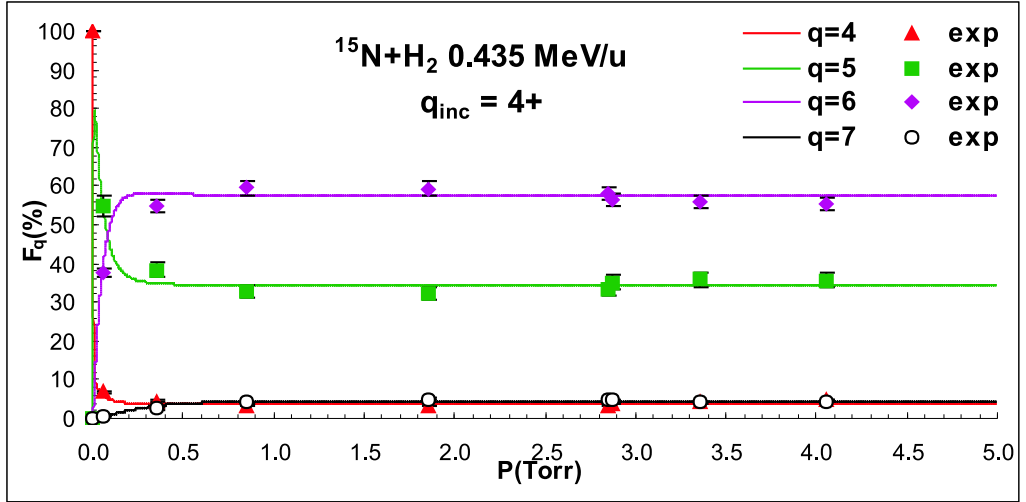


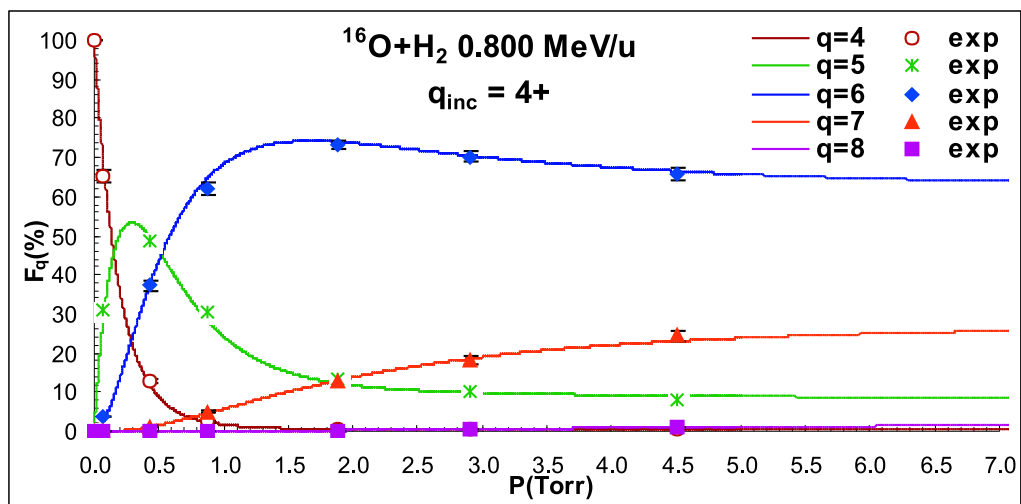
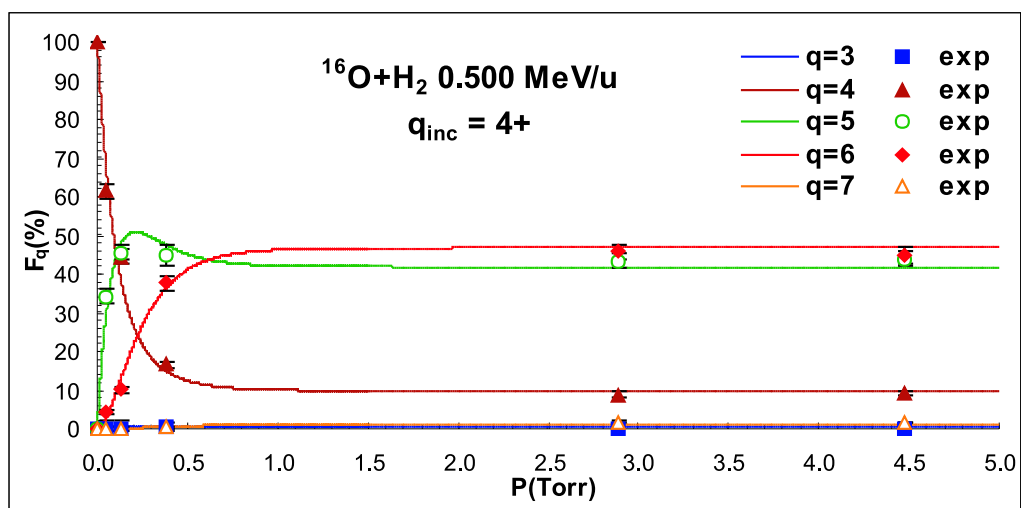


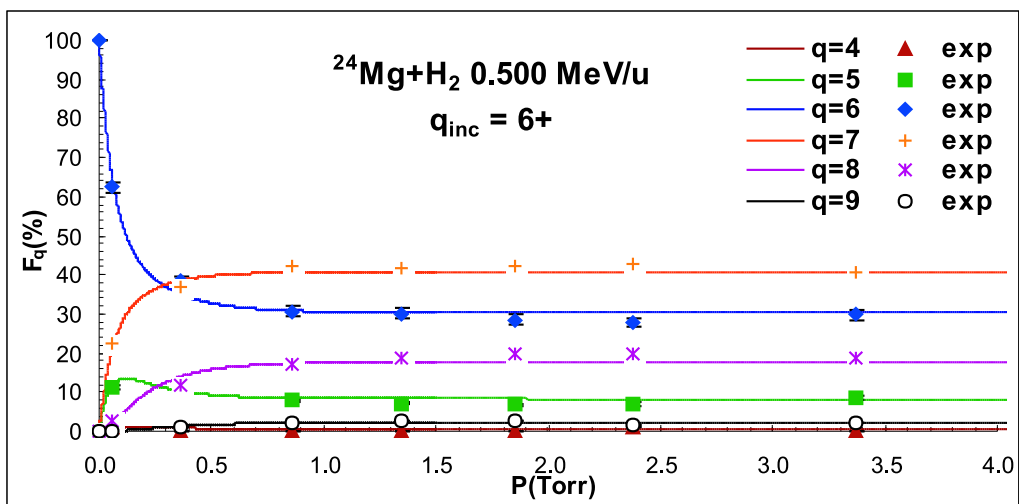
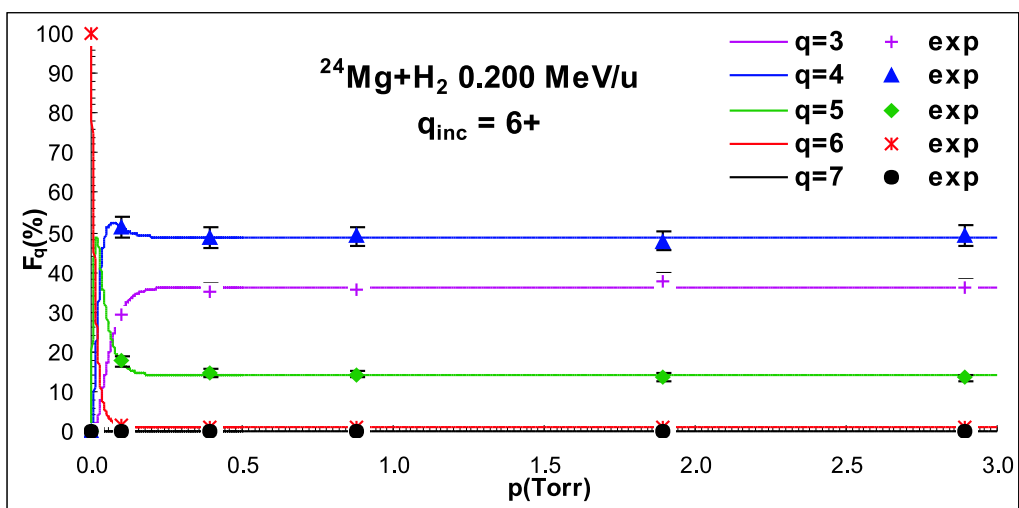


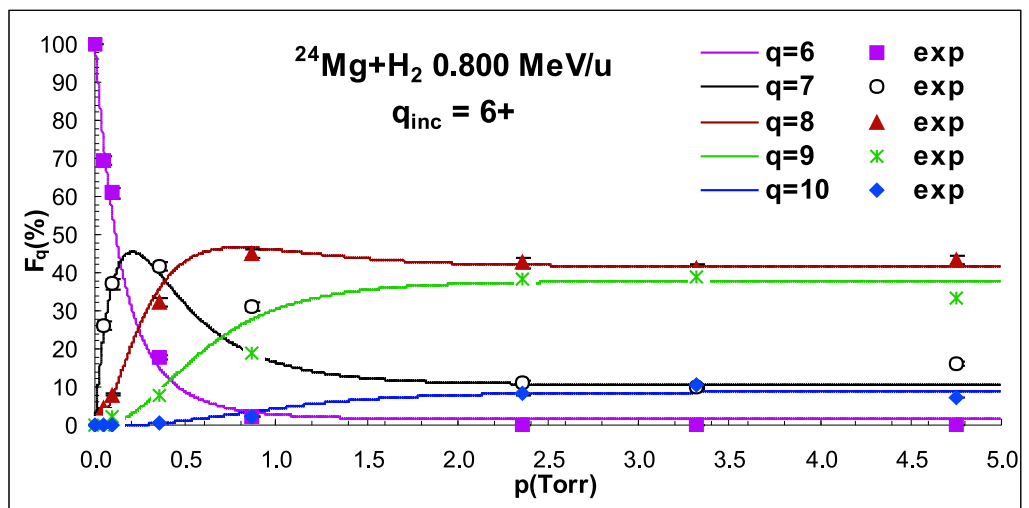


A.2 DRAGON Experiment Results









Appendix B

Illustration of Experimental Data and Charge State distribution Calculation

As an illustration of how the charge state distribution is calculated from experimental data, all the original data and calculation are shown here for two cases. One is for ^{16}O beam of 0.138 MeV/u with incident charge state 2+ passing through hydrogen gas target, measured at Naples; and the other is for ^{16}O beam of 0.800 MeV/u with incident charge state 4+ passing through hydrogen gas target, measured at DRAGON.

In Table B.1 and B.2, P is the target chamber pressure read by the baratron manometer, q the charge state and B_{sw} the magnetic field of the switching magnet for the corresponding charge state. I_3, I_4, I_5 represent the reading of Faraday cups located upstream the target, at the exit of the target and downstream the switching magnet, respectively (Figure 3.1). n_q is the beam particle intensity normalized to I_4, I_3 , respectively, calculated using equation (3.4), and $\Delta n_q/n_q$ the corresponding percentage uncertainty from equation (3.7). The charge state fraction F_q and its uncertainty are calculated as shown by equation (3.5) and (3.9).

In Table B.3 and B.4, I_4 represents the reading of HEBT Faraday cup FC4 located upstream the target, while I_1 and I_{FCCH} are readouts of current integrator connected to DRAGON FC1 and FCCH located at the exit of the target and downstream MD1, respectively (Figure 3.3). At each pressure, we first integrated the beam on FC1 and then on FCCH for different charge states. E_0 and E_1 are readouts of two particle detectors installed inside the target cell as have been discussed in section 3.3.2. Trigger gives a measure of the duration of the measurement. $n_q, \Delta n_q/n_q$ and F_q are calculated as above except that n_q is normalized to E_0 and E_1 , respectively, which give a more accurate measure of the beam intensity. At zero pressure, n_q is normalized to trigger reading presuming a constant

beam because of the absence of the particle detector measurement. The error on current integrator and elastic monitor readouts are considered as statistical error. The offset of the pressure reading is checked by normalizing E_0 readout to incident beam intensity (I_4) and time (Trigger), as shown in Figure B.1, and determined to be 0.124 Torr. This should be deducted from the pressure reading.

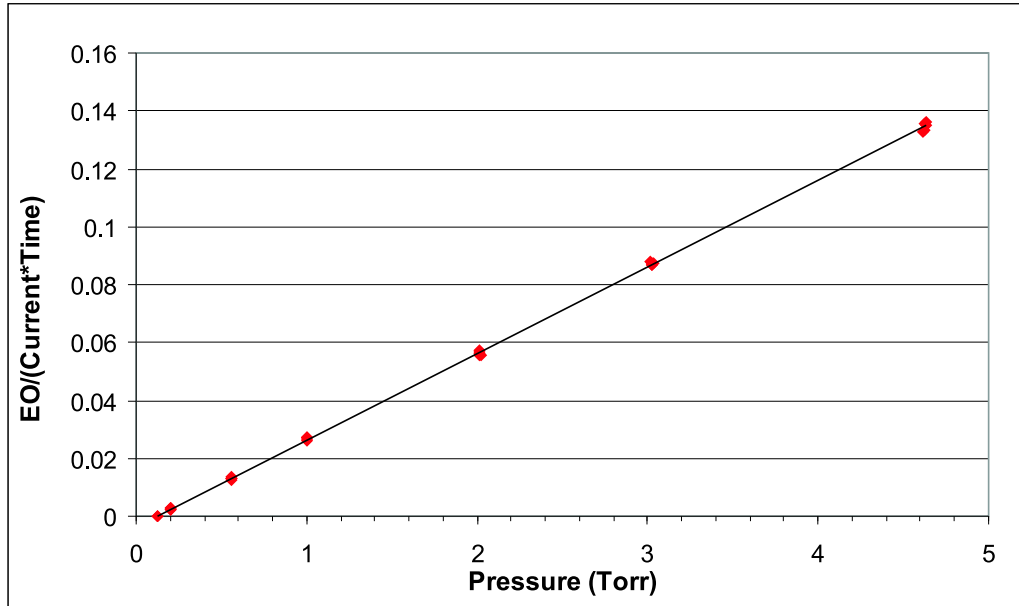


Figure B.1: E_0 reading normalized to incident beam intensity and time plotted as a function of pressure reading.

Table B.1: $^{16}O^{2+}0.138MeV/u + H_2$

Measurement						Calculation					
$P(mbar)$	q	B_{sw}	$I_5(nA)$	$I_4(nA)$	$I_3(nA)$	Normalize to I_4			Normalize to I_3		
						n_q	$\Delta n_q/n_q(\%)$	$F_q(\%)$	n_q	$\Delta n_q/n_q(\%)$	$F_q(\%)$
0	1	10942	0.034 ± 0.001	1.70 ± 0.05	4.2 ± 0.1	0.020	4.2	4.2 ± 0.2	0.008	3.8	4.1 ± 0.2
0	2	5419	1.30 ± 0.05	1.70 ± 0.05	4.1 ± 0.1	0.371	4.8	78.4 ± 1.0	0.159	4.6	79.4 ± 0.9
0	3	3623	0.32 ± 0.01	1.70 ± 0.05	4.2 ± 0.1	0.063	4.3	13.2 ± 0.7	0.025	6.7	12.7 ± 1.0
0	4	2725	0.12 ± 0.01	1.65 ± 0.05	4.2 ± 0.1	0.018	8.9	3.8 ± 0.4	0.007	8.7	3.6 ± 0.4
0	5	2171	0.012 ± 0.001	1.65 ± 0.05	4.2 ± 0.1	0.001	8.9	0.30 ± 0.03	0.0006	8.7	0.29 ± 0.03
0.025	1	10928	0.040 ± 0.001	0.77 ± 0.03	2.75 ± 0.05	0.052	4.6	11.8 ± 0.6	0.015	3.1	11.4 ± 0.4
0.025	2	5472	0.32 ± 0.01	0.79 ± 0.03	2.65 ± 0.05	0.202	4.9	45.8 ± 1.4	0.060	3.7	47.4 ± 1.2
0.025	3	3640	0.38 ± 0.01	0.80 ± 0.02	2.90 ± 0.05	0.158	3.6	35.8 ± 1.0	0.044	3.1	34.3 ± 0.9
0.025	4	2710	0.10 ± 0.01	0.90 ± 0.01	2.95 ± 0.05	0.028	10.0	6.3 ± 0.7	0.008	10.1	6.6 ± 0.7
0.025	5	2171	0.006 ± 0.001	0.93 ± 0.01	3.0 ± 0.05	0.001	16.7	0.29 ± 0.06	0.0004	16.7	0.31 ± 0.06
0.050	1	10922	0.056 ± 0.001	1.24 ± 0.05	3.5 ± 0.1	0.045	4.4	11.2 ± 0.5	0.016	3.4	11.5 ± 0.4
0.050	2	5426	0.41 ± 0.01	1.20 ± 0.05	3.45 ± 0.10	0.171	4.8	42.4 ± 1.4	0.059	2.9	42.8 ± 0.9
0.050	3	3628	0.53 ± 0.02	1.15 ± 0.05	3.35 ± 0.10	0.154	5.8	38.1 ± 1.7	0.053	4.8	38.0 ± 1.4
0.050	4	2724	0.135 ± 0.005	1.05 ± 0.05	3.3 ± 0.1	0.032	6.0	8.0 ± 0.5	0.010	4.8	7.4 ± 0.4
0.050	5	2170	0.007 ± 0.001	1.00 ± 0.05	3.2 ± 0.1	0.001	15.1	0.33 ± 0.06	0.0004	14.6	0.32 ± 0.05

Table B.2: $^{16}O^{2+}0.138MeV/u + H_2$ (continued)

Measurement						Calculation					
$P(mbar)$	q	B_{sw}	$I_5(nA)$	$I_4(nA)$	$I_3(nA)$	Normalize to I_4			Normalize to I_3		
						n_q	$\Delta n_q/n_q(\%)$	$F_d(\%)$	n_q	$\Delta n_q/n_q(\%)$	$F_d(\%)$
0.100	1	10891	0.052 ± 0.001	1.25 ± 0.05	3.5 ± 0.1	0.042	4.4	10.0 ± 0.5	0.015	3.4	9.8 ± 0.4
0.100	2	5449	0.45 ± 0.02	1.3 ± 0.1	3.6 ± 0.1	0.173	8.9	41.6 ± 2.6	0.063	5.2	41.2 ± 1.6
0.100	3	3607	0.66 ± 0.02	1.3 ± 0.05	3.5 ± 0.1	0.169	4.9	40.6 ± 1.4	0.063	4.2	41.3 ± 1.2
0.100	4	2706	0.175 ± 0.001	1.4 ± 0.05	3.8 ± 0.1	0.031	4.6	7.5 ± 0.4	0.011	3.9	7.6 ± 0.3
0.100	5	2166	0.01 ± 0.001	1.45 ± 0.05	3.6 ± 0.1	0.001	10.6	0.33 ± 0.04	0.0006	10.4	0.36 ± 0.04
0.250	1	10872	0.062 ± 0.001	1.47 ± 0.05	3.9 ± 0.1	0.042	3.8	10.3 ± 0.4	0.016	3.0	10.0 ± 0.3
0.250	2	5432	0.50 ± 0.01	1.50 ± 0.05	3.85 ± 0.10	0.167	3.9	40.8 ± 1.1	0.065	3.3	40.9 ± 1.0
0.250	3	3616	0.72 ± 0.01	1.45 ± 0.05	3.7 ± 0.1	0.166	3.7	40.5 ± 1.1	0.065	5.9	40.9 ± 0.9
0.250	4	2725	0.19 ± 0.01	1.45 ± 0.05	3.8 ± 0.1	0.033	6.3	8.0 ± 0.5	0.013	5.9	7.9 ± 0.5
0.250	5	2182	0.010 ± 0.001	1.40 ± 0.05	3.8 ± 0.1	0.001	10.6	0.35 ± 0.04	0.0005	10.3	0.33 ± 0.04
0.500	1	10892	0.064 ± 0.001	1.45 ± 0.05	3.9 ± 0.1	0.044	3.8	10.3 ± 0.4	0.016	3.0	10.1 ± 0.3
0.500	2	3393	0.54 ± 0.02	1.5 ± 0.05	4.0 ± 0.1	0.180	5.0	42.0 ± 1.5	0.068	4.5	41.5 ± 1.3
0.500	3	3603	0.74 ± 0.02	1.55 ± 0.05	4.05 ± 0.1	0.159	4.2	37.2 ± 1.2	0.061	3.7	37.5 ± 1.0
0.500	4	2699	0.2 ± 0.02	1.6 ± 0.05	4.05 ± 0.1	0.031	10.5	7.3 ± 0.8	0.012	10.3	7.6 ± 0.8
0.500	5	2159	0.11 ± 0.02	1.6 ± 0.05	4.1 ± 0.1	0.014	18.4	3.2 ± 0.7	0.005	18.3	3.3 ± 0.7
1.000	1	10732	0.029 ± 0.001	0.6 ± 0.03	2.6 ± 0.05	0.048	6.1	11.9 ± 0.8	0.011	3.9	12.7 ± 0.5
1.000	2	5296	0.21 ± 0.01	0.58 ± 0.03	2.6 ± 0.05	0.181	7.0	44.6 ± 2.2	0.040	5.1	45.8 ± 1.6
1.000	3	3560	0.26 ± 0.01	0.55 ± 0.03	2.65 ± 0.05	0.158	6.7	38.9 ± 2.0	0.033	4.3	37.1 ± 1.3
1.000	4	2632	0.041 ± 0.001	0.55 ± 0.03	2.65 ± 0.05	0.019	6.0	4.6 ± 0.3	0.004	3.1	4.4 ± 0.2

Table B.3: $^{16}O^{4+}0.800MeV/u + H_2$

Measurement								Calculation					
$P(Torr)$	q	$I_4(nA)$	I_1	I_{rCCH}	E_0	E_1	Trigger	n_q	$\Delta n_q/n_q(\%)$	$F_d(\%)$	n_q	$\Delta n_q/n_q(\%)$	$F_d(\%)$
0.125	4	9.8	7825				4885						
0.125	4	9.8		6888			4186	0.4114	2.0	99.47 \pm 0.01			
0.125	5	9.8		95			8671	0.0022	10.3	0.53 \pm 0.08			
0.200	4	8.6	10497		168	58	7465						
0.200	4	8.6		5655	156	58	6427	9.063	8.1	65.2 \pm 2.5	24.38	13.2	65.7 \pm 4.0
0.198	5	8.5		3566	165	63	7950	4.322	8.0	31.1 \pm 2.3	11.32	12.7	30.5 \pm 3.7
0.198	6	8.6		1293	416	153	18788	0.5180	5.6	3.7 \pm 0.3	1.409	8.5	3.8 \pm 0.4
0.198	7	8.5		3	416	167	19339	0.0010	57.9	0.007 \pm 0.005	0.0026	58.3	0.007 \pm 0.005
0.557	4	10.3	6536		454	372	3026						
0.557	4	10.3		1834	1209	2121	8996	0.3792	3.7	12.8 \pm 0.5	0.2162	3.2	18.6 \pm 0.6
0.557	5	10.4		6816	944	2461	6759	1.444	3.5	48.7 \pm 1.1	0.5539	2.4	47.8 \pm 0.7
0.557	6	10.3		5776	874	3307	6763	1.101	3.6	37.2 \pm 1.1	0.2911	2.2	25.1 \pm 0.5
0.559	7	8.7		386	1419	562	12729	0.0389	5.7	1.3 \pm 0.1	0.0981	6.6	8.5 \pm 0.6
0.559	8	8.7		0	725	289	6450						
1.003	4	9.8	14105		1633	756	6247						
1.003	4	9.8		236	1602	701	6225	0.0368	7.0	2.4 \pm 0.2	0.0842	7.5	2.4 \pm 0.2
1.006	5	9.8		3986	1724	751	6429	0.4624	2.9	30.6 \pm 0.8	1.062	4.0	30.8 \pm 1.1
1.006	6	9.8		10169	1805	795	6703	0.9390	2.6	62.1 \pm 0.8	2.132	3.7	61.8 \pm 1.1
1.006	7	9.8		911	1754	754	6674	0.0742	4.1	4.9 \pm 0.2	0.1726	4.9	5.0 \pm 0.3
1.006	8	9.8		0	1529	718	6005						

Table B.4: $^{16}O^{4+}0.800MeV/u + H_2$ (continued)

Measurement										Calculation				
$P(Torr)$	q	$I_4(nA)$	I_1	I_{FCC}	E_0	E_1	Trigger	Normalize to E_0		Normalize to E_1				
								n_q	$\Delta n_q/n_q(\%)$	$F_q(\%)$	n_q	$\Delta n_q/n_q(\%)$	$F_q(\%)$	
2.007	4	9.8	14918		3485	1514	6222							
2.010	4	9.8		59	4127	1816	7362	0.0036	13.1	0.49 ± 0.08	0.0081	13.2	0.51 ± 0.08	
2.015	5	9.8		1659	3484	1603	6337	0.0952	3.0	13.2 ± 0.4	0.2070	3.5	13.0 ± 0.5	
2.015	6	9.8		15449	4851	2194	8733	0.5308	1.6	73.3 ± 0.4	1.1736	2.3	73.6 ± 0.5	
2.017	7	9.8		2472	3799	1728	7003	0.0930	2.6	12.8 ± 0.4	0.2044	3.1	12.8 ± 0.5	
2.019	8	9.8		29	3604	1644	6606	0.0010	18.6	0.14 ± 0.03	0.0022	18.7	0.14 ± 0.03	
3.013	4	9.8	15401		5342	2370	6278							
3.020	4	9.8		40	5664	2471	6588	0.0018	15.9	0.38 ± 0.07	0.0040	15.9	0.38 ± 0.08	
3.021	5	9.8		1301	5599	2391	6550	0.0465	3.1	9.9 ± 0.4	0.1088	3.4	10.3 ± 0.4	
3.023	6	9.8		11946	6012	2672	7046	0.3312	1.6	70.8 ± 0.4	0.7451	2.1	70.8 ± 0.5	
3.029	7	9.8		3743	6224	2819	7303	0.0859	2.1	18.4 ± 0.4	0.1897	2.5	18.0 ± 0.5	
3.031	8	9.8		108	5708	2495	6650	0.0024	9.7	0.51 ± 0.06	0.0054	9.8	0.51 ± 0.06	
4.610	4	9.8	10878		5928	2616	4465							
4.610	4	9.8		36	8051	3617	6199	0.0011	16.7	0.37 ± 0.07	0.0025	16.7	0.36 ± 0.07	
4.620	5	9.8		1051	8342	3647	6290	0.0252	3.3	8.3 ± 0.3	0.0576	3.5	8.4 ± 0.3	
4.626	6	9.8		10800	8970	3978	6862	0.2007	1.4	65.8 ± 0.4	0.4525	1.9	65.9 ± 0.5	
4.633	7	9.8		3230	6184	2768	4640	0.0746	2.2	24.5 ± 0.5	0.1667	2.6	24.3 ± 0.6	
4.636	8	9.8		220	8468	3712	6409	0.0032	6.8	1.1 ± 0.1	0.0074	6.9	1.1 ± 0.1	

Bibliography

- [1] L. Buchmann. *Elemental Synthesis in the Universe*. Lecture Note for Phys881 at SFU, 2001.
- [2] G. H. Henderson. Proc. R. Soc. London A102, 496, 1922.
- [3] S. K. Allison. Rev. Mod. Phys. 30, 1137, 1958.
- [4] V. S. Nikolaev. Sov. Phys. Usp. 8, 269, 1965.
- [5] H. D. Betz. Rev. Mod. Phys. 44, 465, 1972.
- [6] H. B. Gillbody. Adv. At. Mol. Phys. 22, 143, 1986.
- [7] B. H. Bransden and M.R. C. McDowell. *Charge Exchange and the Theory of Ion-Atom Collisions*. Oxford University Press, New York, 1992.
- [8] E. W. McDaniel, J. B. A. Mitchell, and M. E. Rudd. *Atomic Collisions – Heavy Particle Projectile, chap. 5*. John Wiley & Sons, Inc., 1993.
- [9] S. Datz, C. D. Moak, H.O. Lutz, L. C. Northcliffe, and L. B. Bridwell. At. Data. 2, 273, 1971.
- [10] A. B. Wittkower and H. D. Betz. At. Data 5, 2, 116, 1973.
- [11] H. Tawara, T. Kato, and Y. Nakai. At. Data Nucl. Data Tables 32, 235, 1985.
- [12] W. K. Wu, B. A. Huber, and K. Wiesemann. At. Data Nucl. Data Tables 40, 57, 1988.
- [13] W. K. Wu, B. A. Huber, and K. Wiesemann. At. Data Nucl. Data Tables 42, 157, 1989.
- [14] *CRC Handbook of Chemistry and Physics, 70th*. CRC Press, Boca Raton, 1989.

- [15] W. N. Lennard, D. Phillips, and D. A. S. Walker. Nucl. Instr. and Meth. 179, 413, 1981.
- [16] N. Bohr. Phys. Rev. 58, 654, 1940.
- [17] N. Bohr. Phys. Rev. 59, 270, 1941.
- [18] W. E. Lamb. Phys. Rev. 58, 696, 1940.
- [19] H. H. Heckmann, E. L. Hubbard, and W. G. Simon. Phys. Rev. 129, 1240, 1963.
- [20] P. O. Lowdin. J. Molec. Spectry. 3, 46, 1959.
- [21] J. K. Knipp and E. Teller. Phys. Rev. 59, 659, 1941.
- [22] G. I. Bell. Phys. Rev. 90, 548, 1953.
- [23] H.D. Betz, G. Hortig, E. Leischner, Ch. Schmelzer, B. Stadler, and J. Weihrauch. Phys. Lett 22, 643, 1966.
- [24] V. S. Nikolaev and I. S. Dmitriev. Phys. Lett. A 28, 277, 1968.
- [25] K. Shima, N. Kuno, and I. S. Dmitriev. Phys. Rev. A 40, 3557, 1989.
- [26] X. Tordoir, T. Bastin, P. D. Dumont, and H. P. Garnir. Nucl. Instr. and Meth. B 173, 275, 2001.
- [27] G. Schiwietz and P. L. Grande. Nucl. Instr. and Meth. B 175, 125, 2001.
- [28] G. Ryding, A. B. Wittkower, and P. H. Rose. Phys. Rev. 185, 129, 1969.
- [29] A. B. Wittkower and G. Ryding. Phys. Rev. A 4, 226, 1971.
- [30] H. D. Betz. in *Applied Atomic Collision Physics*. Academic, New York, Vol. 4, p.1, 1984.
- [31] O. Sayer. Rev. Phys. Appl. 12, 1543, 1977.
- [32] Y. Baudinet-Robinet. Nucl. Instr. and Meth. 190, 197, 1981.
- [33] N. Bohr. Kgl. Danske Videnskab. Selskab, Mat.-Fys. Medd. 18, No.8, 1948.
- [34] N. Bohr and J. Lindhard. Kgl. Danske Videnskab. Selskab, Mat.-Fys. Medd. 28, No.7, 1954.

- [35] K. H. Berkner, W. G. Graham, R.V. Pyle, A. S. Schlachter, and J. W. Stearns. Phys. Rev. A 23, 2891, 1981.
- [36] A. S. Schlachter, J. W. Stearns, and W. G. Graham. Phys. Rev. A 27, 3372, 1983.
- [37] L. Campajola et al. Nucl. Instr. and Meth. B 29, 129, 1987.
- [38] F. Terrasi et al. Nucl. Instr. and Meth. B 52, 259, 1990.
- [39] J. F. Ziegler, J. P. Biersack, and U. Littmark. *The Stopping And Range Of Ions in Matter*. www.SRIM.org, 2000.
- [40] L. Gialanella et al. Nucl. Instr. and Meth. A 376, 174, 1996.
- [41] C. Rolfs and W. S. Rodney. Nucl. Phys. A 235, 450, 1974.
- [42] S. Dushman. *Scientific Foundations of Vacuum Technique, 2nd edition*. Wiley, New York, 1962.
- [43] E. C. Montenegro and G. M. Sigaud. Phys. Rev. A 45, 1575, 1992.
- [44] R. A. Phaneuf and F. W. Meyer. Phys. Rev. A 17, 534, 1978.
- [45] F. W. Meyer, R. A. Phaneuf, H. J. Kim, P. Hvelplund, and P. H. Stelson. Phys. Rev. A 19, 515, 1979.